

Journal of Engineering and Technology for Industrial Applications



ISSN 2447-0228

February 2023

Volume 09 / No 39

Editor-in-Chief: J. C. Leite

www.itegam-jetia.org



O **ITEGAM-JETIA: Journal of Engineering and Technology for Industrial Applications** is a publication of the Galileo Institute of Technology and Education of the Amazon (ITEGAM), located in the city of Manaus since 2008. JETIA publishes original scientific articles covering all aspects of engineering. Our goal is the dissemination of research original, useful and relevant presenting new knowledge on theoretical or practical aspects of methodologies and methods used in engineering or leading to improvements in professional practice. All the conclusions presented in the articles It should be state-of-the-art and supported by current rigorous analysis and balanced assessment. Public magazine scientific and technological research articles, review articles and case studies.

JETIA will address topics from the following areas of knowledge: Mechanical Engineering, Civil Engineering, Materials and Mineralogy, Geosciences, Environment, Information and Decision Systems, Processes and Energy, Electrical and Automation, Mechatronics, Biotechnology and other Engineering related areas.

Publication Information:

ITEGAM-JETIA (ISSN 2447-0228), (online) is published by Galileo Institute of Technology and Education of the Amazon on a every two months (February, April, June, August, October and December).

Contact information:

Web page: www.itegam-jetia.org

Email: editor@itegam-jetia.org

Galileo Institute of Technology and Education of the Amazon (ITEGAM).

Joaquim Nabuco Avenue, No. 1950. Center. Manaus, Amazonas. Brazil.

Zip Code: 69020-031. Phone: (92) 3584-6145.

Copyright 2014. Galileo Institute of Technology and Education of the Amazon (ITEGAM)

The total or partial reproduction of texts related to articles is allowed, only if the source is properly cited. The concepts and opinions expressed in the articles are the sole responsibility of the authors.

Previous Notice

All statements, methods, instructions and ideas are the sole responsibility of the authors and do not necessarily represent the view of ITEGAM -JETIA. The publisher is not responsible for any damage and / or damage to the use of the contents of this journal. The concepts and opinions expressed in the articles are the sole responsibility of the authors.

Directory

Members of the ITEGAM Editorial Center - Journal of Engineering and Technology for Industrial Applications (ITEGAM-JETIA) of the Galileo Institute of Technology and Education of the Amazon (ITEGAM). Manaus-Amazonas, Brazil.

Jandecy Cabral Leite, CEO and Editorial Editor-in-Chief

Ivan Leandro Rodriguez Rico, Editorial Assistant

Ricardo Silva Parente, Information Technology Assistant



ITEGAM-JETIA. v.9, n.39. February of 2023. Manaus - Amazonas, Brazil. ISSN 2447-0228 (ONLINE)
<https://www.itegam-jetia.org>

SUMMARY

- DESIGN OF THE POSITION CONTROL SYSTEM OF PARABOLIC SOLAR CONCENTRATORS THROUGH COLLECTOR BY ELECTRICAL DRIVE** 4
José Abreu García, Ariel Barreiros Albo and Lianet Consuegra Morales
- ESCHERICHIA COLI BACTERIAL COLONIES IN PATIENTS WITH URINARY TRACT INFECTIONS USING FRESH AND STORED URINE SPECIMENS** 15
Vincentia Ade Rizky, Sa'adah Siregar, Asvia Rahayu, Visensius Krisdianilo and Novita Trisna Murti
- MODIFIED BAT ALGORITHM FOR TRANSMISSION NETWORK EXPANSION PLANNING CONSIDERING ACTIVE POWER LOSSES** 19
João Ricardo Paes de Barros and Dimitri Albuquerque de Barros
- NATURE OF DISPERSION: ITS RELATIONSHIP WITH SOME FRACTAL AND THERMODYNAMIC PHENOMENA** 33
Alfredo José Constain, Gina Peña Olarte and Carlos Peña Guzman
- BEST LABORATORY PRACTICES FOR REDUCING UNCERTAINTY IN THE PRESSURE DIFFERENTIAL (ΔP) MEASUREMENTS IN CORE-FLOODING TESTS FOR THE PETROPHYSICAL CHARACTERIZATION OF RESERVOIRS** 42
Jorge Alberto Rojas P., Jenny Paola Rueda M., Jorge Alejandro Sarmiento G., Pedro Juan Rojas M., Jose Luis Mendoza, Cesar Augusto Romero R. and Carlos Humberto Amaya A.



ISSN ONLINE: 2447-0228

ITEGAM-JETIA

Manaus, v.9 n.39, p. 4-14. Jan/Feb, 2023.
DOI: <https://doi.org/10.5935/jetia.v9i39.848>



RESEARCH ARTICLE

OPEN ACCESS

DESIGN OF THE POSITION CONTROL SYSTEM OF PARABOLIC SOLAR CONCENTRATORS THROUGH COLLECTOR BY ELECTRICAL DRIVE

José Abreu García*¹, Ariel Barreiros Albo² and Lianet Consuegra Morales³

¹ Faculty of Electrical Engineering, Marta Abreu de Las Villas Central University - UCLV, Cuba.

^{2,3} Faculty of Electrical Engineering, Marta Abreu de Las Villas Central University - UCLV, 3 CEDAI Ciego de Ávila, Cuba.

¹ <http://orcid.org/0000-0002-8344-8796> , ² <http://orcid.org/0000-0002-6238-069X> , ³ <http://orcid.org/0000-0002-6493-5409> 

Email: *abreu@uclv.edu.cu, abarreiros@uclv.cu, lianetcm98@gmail.com

ARTICLE INFO

Article History

Received: January 23th, 2023

Accepted: February 21th, 2023

Published: February 28th, 2023

Keywords:

Parabolic solar concentrator,
Tracking systems,
Electric drive,
Solar energy,
Raspberry Pi.

ABSTRACT

Solar energy is one of the most important renewable energies due to its abundance and sustainability. This has led to a great development in the technologies used to obtain them, which are increasingly effective and varied, such as solar thermal collection technology. Solar thermal collection technology to obtain a greater capture of solar energy requires a monitoring mechanism for its use, either manual or automatic. This work provides a proposal for automatic solar tracking in Parabolic Trough Solar Concentrators, with the aim that they absorb as much solar energy as possible during the day from the position control of their reflectors to faithfully follow the solar path. The positioning of these collectors is done by an electric drive and using a Raspberry Pi single-board computer as a control and command unit. The geared motor and the other elements that conform to the system were selected in compliance with the requirements of the application. The programming of the position control system implemented in the Raspberry Pi is carried out and the collectors are provided with wind safety. Finally, the results of the simulation tests made with the help of the MATLAB tool are carried out and shown. In addition to an economic and environmental analysis that demonstrates the reliability of the project. The system design generated a satisfactory result for sun tracking using the developed algorithm.



Copyright ©2023 by authors and Galileo Institute of Technology and Education of the Amazon (ITEGAM). This work is licensed under the Creative Commons Attribution International License (CC BY 4.0).

I. INTRODUCTION

Solar energy is one of the cleanest energy resources, it does not modify the environment and above all it is free. This energy is obtained from the Sun and, depending on the solar radiation incident on the Earth, it can be harnessed by its heating capacity (solar thermal energy) or directly by the photoelectric effect (solar photovoltaic energy). Moreover, it is considered the backbone of any sustainable development program [1],[2] and from this point of view, it offers several advantages. The use of this energy resource allows the recovery of degraded lands, the increase of regional and national energy independence, as well as the diversification and security of energy supply, and the improvement of the quality of water resources.

N nowadays, energy consumption has become a basic factor for many aspects of human activity and progress [3]. Therefore, energy is indispensable for the advancement of a country, so much

so that the rate of energy consumption is closely related to the degree of economic development. On the other hand, the various global developments such as global warming, pollution, scarcity of non-renewable resources, and high energy demand also constitute a reason why renewable energies are in great demand [4]. The use of the solar resource produces no polluting emissions to the environment and is obtained from a virtually inexhaustible natural source [5].

Solar energy currently holds incredible promise as renewable energy to meet the world's energy demand [6]. The solar energy absorbed by the Earth in one year is approximately 20 times the energy stored in all the fossil fuel reserves in the world [3]. According to the 21st World Energy Council Study [7], by the year 2100, 70% of the energy consumed will be of solar origin. Likewise, the use of technologies for obtaining solar energy presents great potential in tropical countries where the intensity of

solar radiation has a high value, between $900 \text{ [W/m}^2\text{]}$ and $1000 \text{ [W/m}^2\text{]}$ when it is incident perpendicularly on a surface. This represents an average of approximately $400 \text{ [W/m}^2\text{]}$ on the earth's surface [8], and more than 5 kWh per day per square meter as an annual average value.

II. THEORETICAL REFERENCE

II.1 PARABOLIC SOLAR CONCENTRATOR THROUGH COLLECTOR

Solar thermal energy has now achieved a degree of maturity, both economically and technically, and is thus a good option for the production of electrical energy. Parabolic solar concentrators through collectors (PTC) are part of this solar energy strategy [2]. These have several application alternatives among which are to satisfy the heat requirements of processes in the chemical and food industry, in processes such as drying, sterilization, and cleaning, as well as the conditioning of industrial buildings [9]. This energy alternative avoids the use of conventional energy sources and therefore reduces the environmental impact produced by the use of the latter.

There are several types of solar thermal collectors that, although they have the same principle, have different characteristics:

- Stationary" collectors: These types of collectors are stationary all day long and operate with global solar energy [10]. They are located at an angle capable of covering the declination of the Sun from the summer solstice to the winter solstice [11]. Evacuated tube and flat plate collectors are within this classification.

- Tracker" collectors: These are collectors that need a solar tracking system to move according to the path of the Sun throughout the day [10]. Within this group can be found the collectors with concentration [11]. As the absorption area of these collectors is small, these systems must be perpendicular to the sun to reach higher temperatures.

- Low temperature ($30^\circ\text{C} - 100^\circ\text{C}$): This range is achieved with flat plate collectors.

- Medium temperature ($100^\circ\text{C} - 400^\circ\text{C}$): These are achieved with linear or spherical concentrators, and include parabolic solar concentrators through collectors.

- High temperature ($400^\circ\text{C}-3000^\circ\text{C}$): These are achieved with point concentrators [10] such as Dish Stirling and central tower fields.

Solar concentrators through collectors are included in solar thermal technologies. This technology takes advantage of the sun's radiation and uses mirrors to reflect it onto a focal line, through which the thermal energy of the solar radiation is transferred, to obtain a high temperature and generate steam [12],[13] move a turbine, and produce electricity.

The operation of the PTC is based on solar tracking and the concentration of solar rays on high thermal efficiency receiver tubes located in the focal line of the cylinders. A working fluid circulates through these tubes, either water or some kind of thermal oil [11], which can reach a temperature of 400°C . Therefore, they are included in the medium temperature solar collectors [10],[14]. This system takes advantage of the property of parabolas [15]: any ray hitting the parabola will be reflected in the direction of a point called the focus.

The PTC concentrates sunlight 30 to 60 times the normal intensity on the absorber, heating the heat transfer fluid to high temperatures [16]. These collectors centralize about 99.95% of the direct solar radiation (DNI) [17], typically generating 100 kW/m^2 .

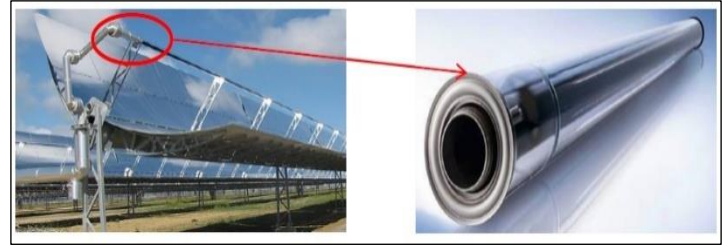


Figure 1: Parabolic solar concentrator trough collector and absorber tube.

Source: Authors, (2023).

The parabolic-cylinder solar concentrator through collector system takes full advantage of direct solar radiation if there is an automated solar tracking mechanism that follows the sun's path throughout the day [18]. The solar tracking system consists of a device that rotates the parabolic-cylinder reflectors of the collector around a tracking axis.

To increase the amount of solar energy reaching the receiver [19], it is necessary to include a solar tracking system that can follow the trajectory of the sun during the day and as a consequence, vary the position of the PTC. The tracking system must have the ability to return the collector to its starting position to wait for the Sun at sunrise, after having tracked the trajectory of the Sun throughout the day. In addition, it must follow the sun regardless of the weather, as long as there are no strong gusts of wind that could damage the collectors and their parts, so the tracking system must also include a safety system to protect against these cases and bring the collectors to a safe position.

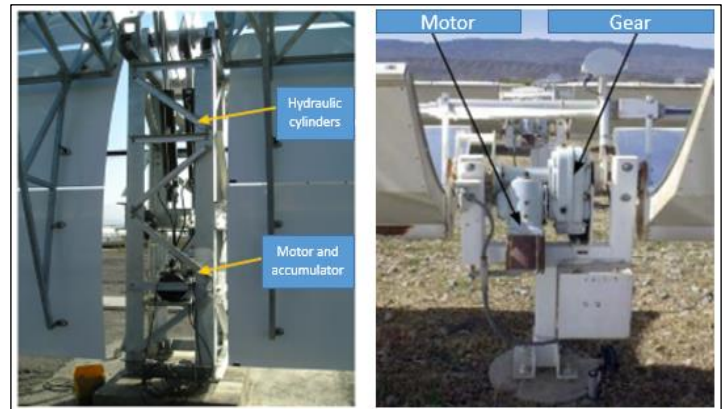


Figure 2: Basic elements of a PTC.

Source: Taken from [20].

II.2 SOLAR TRACKING ALGORITHMS

Solar tracking can be performed using different types of algorithms:

- Sensor tracking: They use photoresistive sensors, which vary the resistive value depending on the amount of light they capture [21]. With this difference, the position of the motor is controlled. It presents difficulties in the presence of cloudy weather.

- Tracking by sundial: The structure moves at a constant speed, it is independent of the weather but does not take into account the nonlinearity of the solar trajectory.

- Tracking by calculated coordinates: It tracks the trajectory of the Sun between each position by calculating its astronomical coordinates. They are immune to cloudy days or any other circumstance that may produce errors in tracking.

Different control strategies can be found:

- Closed loop: tracking systems using this variant are based on feedback transferred from sensors [22] capable of providing information about the solar position concerning the earth plane.

- Open loop: this type of control bases its operation on the estimation of its inputs using only the current state and a computer algorithm to determine whether its inputs have achieved the desired objective [23]. This control lacks feedback in the system because there is no sensor to provide information for correcting the solar tracking.

Trackers according to the type of motion:

- Dual-axis trackers: these trackers have two degrees of freedom acting as axes of rotation, which are typically normal to each other. The primary axis is the one that is fixed concerning the ground and the secondary axis is referenced to the primary axis [24]. This tracking system can change the altitude and azimuthal degrees of the solar collection system, thus tracking the Sun in East to West and North to South directions to maximize energy production [25], making full tracking of the Sun. Although the performance of the installation may be superior compared to single-axis trackers [26], they have a higher cost.

Figure 3: Two-axis solar tracker.



Source: Taken from [11].

- Single-axis trackers: these are the simplest trackers, generally use less energy and are less complex than dual-axis trackers [6]. They have only one degree of freedom so the rotation of the pickup surface is done on a single axis. The limitation of this type of tracker is that it cannot perform a full tracking of the Sun since it can only complete tracking of the Sun since it can only follow [26], for example, the azimuth or the solar inclination, but it can only solar inclination.

PTC is mainly used with a single-axis tracking scheme, as this is mechanically simpler and involves lower costs and lower thermal losses as there is no passive piping [10]. Generally, the collectors can be oriented in two ways: East-West, such that it follows the Sun from North to South, or, in North-South orientation [27] where the collector follows the Sun from East to West.

Tracking on an East-West oriented axis requires less adjustment. However, despite having the aperture always facing the Sun at noon this solar tracking system presents a much lower performance during the morning and afternoon, due to the increase in the angle of incidence. PTCs with an East-West orientation [28] collect more solar energy during winter periods.

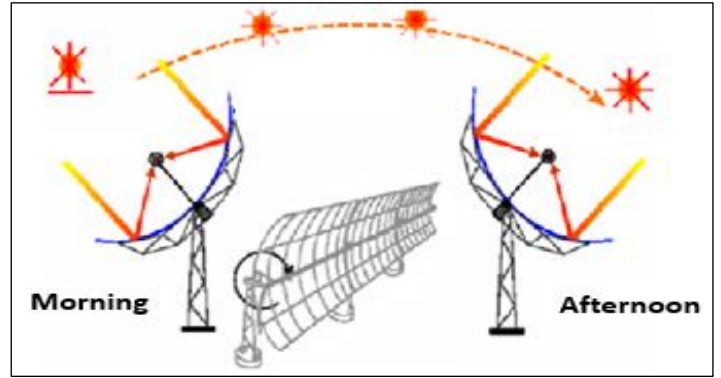


Figure 4: Solar tracking system with one axis of motion. Source: taken from [22].

III. MATERIALS AND METHODS

III.1 STRUCTURE OF THE TRACKING SYSTEM

Based on the above analysis, the tracking system for this application was designed and developed. This system will be constituted by a single axis of movement, following the trajectory of the Sun in the sky from North to South. In other words, following its height, and therefore the collectors will be oriented East-West. Astronomical scheduling is chosen as the tracking method, so it will be necessary to have accurate time and day data.

The collectors are positioned by electric drive and controlled by a Raspberry Pi microcomputer. An anemometer and a wind vane will also be needed to ensure the safe operation of the collectors when functioning during strong gusts of wind.

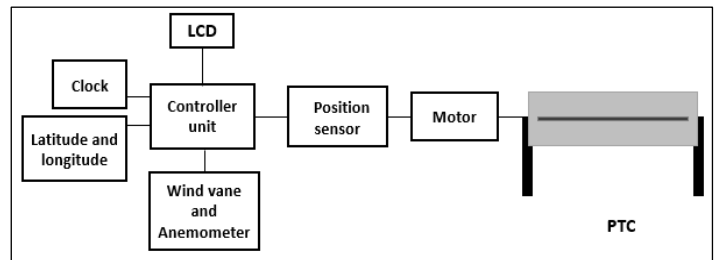


Figure 5: Architecture of the proposed monitoring system. Source: Authors, (2023).

The basic elements that make up the system are: the motor, controller unit, Raspberry Pi, clock, anemometer position sensor, weather vane and a Liquid Cristal Display (LCD).

III.1.1 Requirements of the Collector Position Control System

The proposed tracking system is controlled by a programming algorithm that, based on astronomical calculations, determines the position of the Sun throughout the day, from which the tracking is performed. This system is composed of a positioning system, and a control unit with its respective accessories and elements for the measurement of the variables necessary for such control.

It is desired to control the position of two parabolic solar concentrators through collector of 12 m long and 2.5 m in diameter. To move these collectors it is necessary that the positioning system can develop a moment of 800 Nm.

III.1.2 The Positioning System, Electric Drive

The positioning system consists of a geared motor coupled to the axis of the PTC to carry out its movement to follow the solar

trajectory. This movement will be executed according to the orders received from the controller board of the system.

For the selection of the elements that compose the system, the following factors must be taken into account:

The movement of the Sun across the sky is very slow so the tracking systems are characterized by developing small velocities. Considering normal motor speeds if directly coupled, such a slow speed of motion would not be achieved with adequate torque to drive solar tracking [29]. Therefore, a gear drive system is necessary to reduce the motor speed.

Generally, solar tracking uses a transmission system with a gear ratio between 10,000: 1 and 30,000: 1; thus, the rotational motion of the solar tracker is usually faster than the rotational motion speed of the Sun. This is why on/off type solar tracking control systems are used to synchronize the angular rotational motion of the solar tracker on the ground with the apparent motion of the sun in the sky.

III.2 CONTROL ELEMENTS

III.2.1 Control Unit: Raspberry Pi

The Raspberry Pi is characterized by the possibility of running several Linux distributions and other operating systems such as RISC OS and can be used in electronic projects. In addition, it is capable of doing many of the features offered by a desktop PC, such as running spreadsheet programs [30]. It is possible to connect USB peripherals such as a keyboard, mouse, webcams, Wi-Fi adapters, Bluetooth and many others.

For the implementation of the control algorithm for the solar tracking of this project, the Raspberry Pi 1 Model B+ board is chosen. This Raspberry Pi model has forty pins distributed in two columns of twenty pins each that constitute the general purpose input and output (GPIO) ports of the board, which can be seen in Figure 6.

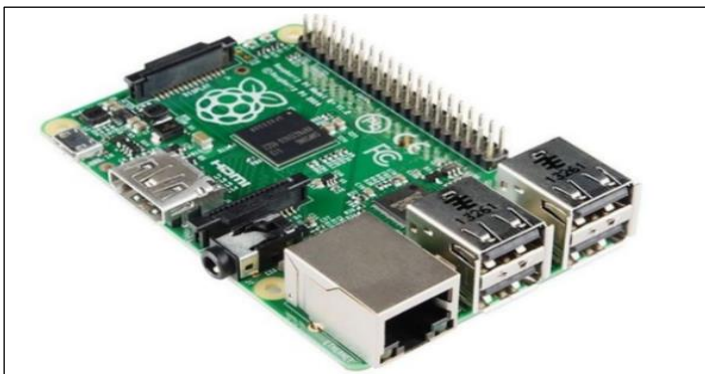


Figure 6: Raspberry Pi 1 Model B+ rev 1.2. Source: Taken from [31].

The system software is located in the micro SD memory inserted in the Raspberry Pi and the programming language used for the implementation of the control algorithm is Python. Using the Anaconda tool, Spyder is used as an integrated development environment (IDE), dedicated to scientific programming in the Python language, a free and simple developmental environment.

III.2.2 Real-Time Clock

A real-time clock (RTC) is responsible for keeping the time and date updated. It consists of an oscillator crystal that generates a frequency of 32768 Hz and a chip capable of keeping the internal registers [31] in which it stores the date and time data updated.

As the Raspberry Pi is designed to be a very low-cost computer there are many of the features provided by traditional computers have been omitted as is the case of the RTCs [32].

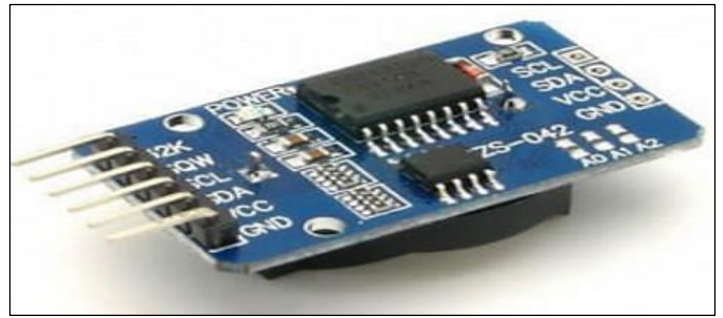


Figure 7: RTC to Raspberry Pi. Source: Taken from [33].

III.2.3 Absolute Encoder

The actual position of the PTC needs to be known and compared with the tracking angle that it should have according to the programming calculations. For that, a device able to measure this variable and provide this data to the controller unit is needed to control the position of these collectors. An absolute encoder is the most suitable device to meet the objective of measuring the position.

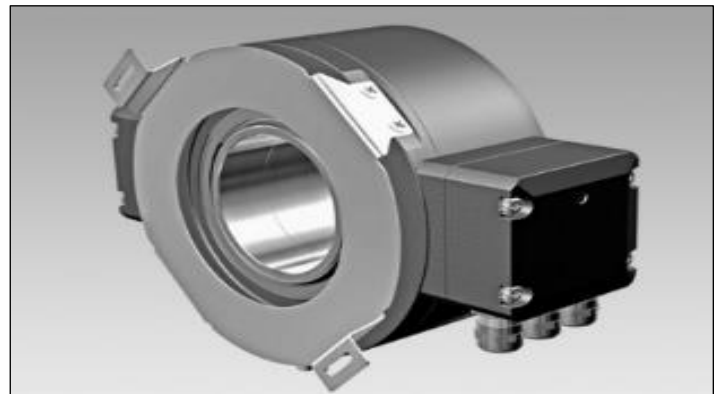


Figure 8: Absolute encoder. Source: Taken from [34].

III.2.4 LCD

For displaying tracking angle data and the actual position of the collector, a 16-column, 2-row LCD can be selected. This allows 16 characters to be displayed in each row [35], with blue backlight feedback and white characters.

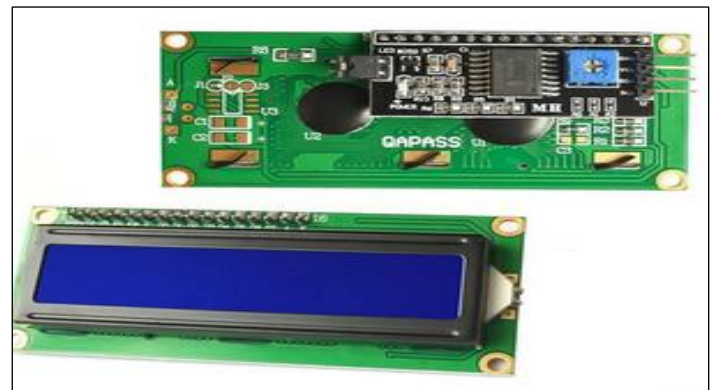


Figure 9: LCD. Source: Taken from [35].

III.2.5 Voltage Level Converter

The GPIOs work with 3.3 V to be able to use the devices that work with 5 V. It is necessary to use a voltage converter to be able to use these devices with the Raspberry Pi. The voltage level converter selected for this project consists of a printed circuit board with 4 bidirectional converter lines, composed of 4 FETs, with 10 K Ω resistors. It works up to 1.8 V on the low side and up to 10 V on the high side.



Figure 10: Bidirectional voltage converter.
Source: Taken from [36].

III.2.6 Optocoupler

An Optocoupler is used to work with 3.3 V input and 24 V output compatible with the proposed Raspberry.

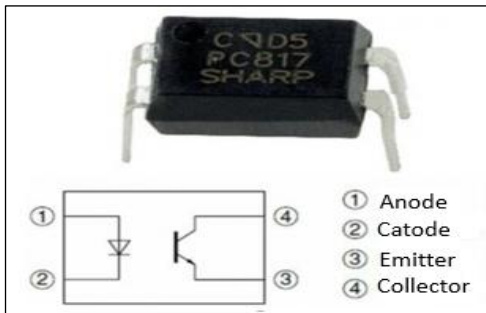


Figure 11: Optocoupler.
Source: Taken from [37].

III.2.7 Battery

The battery should be used as a backup in case of failure of the system power supply. It is advisable to use a lithium polymer battery because they provide longer battery life and allow higher loads [38]. Lithium polymer batteries are composed of solid polymers, which replace the flammable liquid electrolytes used in other types of batteries [28], thus increasing safety when used for any type of application.

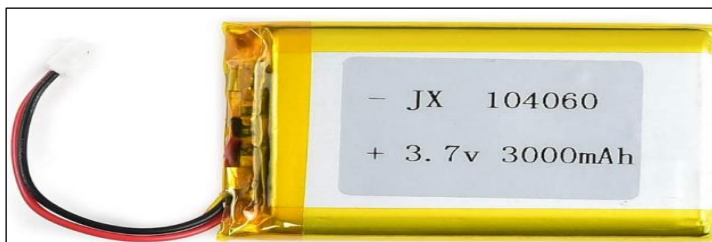


Figure 12: Lithium polymer battery.
Source: Taken from [38].

III.2.8 Safe Position of the Collectors in the Wind

The presence of strong winds causes damage to the components of the collector and its structure.

The PTC can operate as long as the wind speed does not exceed 14 m/s (50.4 km/h) [39], however, when it exceeds 5 m/s (18 km/h) the collector performance will start to be affected. In the case of winds between 14 and 40 m/s (144 km/h), the collector must be brought to a safe position, which varies according to its structural design.

The safe position generally coincides with the rest position to which the collector will be taken at the end of the day to spend the night in this position and be ready for the sunrise, shortening the start-up times. This position will also be used during days when the tracking system is down for maintenance or other factors. The safe position of the collectors is set below the horizontal, thus facilitating maintenance tasks and preventing the first rays of the day from concentrating on the absorber tube when it is not in operation.

III.2.9 Measurement of Wind Speed and Direction

The wind is a natural, generally horizontal movement of air masses [40]. Thermal imbalances between unlike places produce differences in atmospheric pressure, which cause winds. The wind speed can be measured using an anemometer, and the wind direction is measured by a wind vane, which gives the direction from which the wind is coming.

III.2.10 Anemometer

The analog anemometer sends a voltage that varies linearly with the speed of rotation of the blades. As the Raspberry Pi does not have analog input/output pins, it is necessary to use the digital signal generated by the anemometer. The selected sensor must be designed to work outdoors [41] and requires a voltage of 7-24 V to work properly.



Figure 13: Anemometer.
Source: Taken from [41].

III.2.11 Wind Vane

To determine the wind direction, it is necessary use a wind vane. By using a rotary encoder the sensor can indicate which cardinal point coincides with the direction from which the wind is coming.



Figure: 14 Wind vane.
Source: Taken from [42].

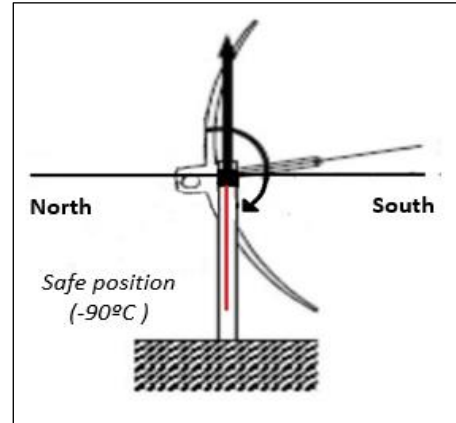


Figure 15: Safety and rest position.
Source: Authors, (2023).

III.2.12 Collector Safety System

If the PTC is tracking the Sun normally and the wind speed exceeds the set limits, it must be moved to a safe position. One option is to take the maximum speed at 40 km/h and the position 90° below the horizontal, the same position that is set for the rest and maintenance state of these collectors.

III.2.13 Control System

The tracking control is performed from the positioning algorithm programmed in the Raspberry Pi, based on astronomical calculations to determine the position of the Sun. The time and date for the calculations are provided by the real-time clock. These calculations determine the reference point of the control system and based on the measurement of the actual position of the PTC provided by the position sensor, the tracking error is determined and if it exists the Raspberry Pi, sends a command signal to the geared motor to adjust the position of the collectors with the desired position in the programming. The system also receives information about the wind speed, acting as a safety system.

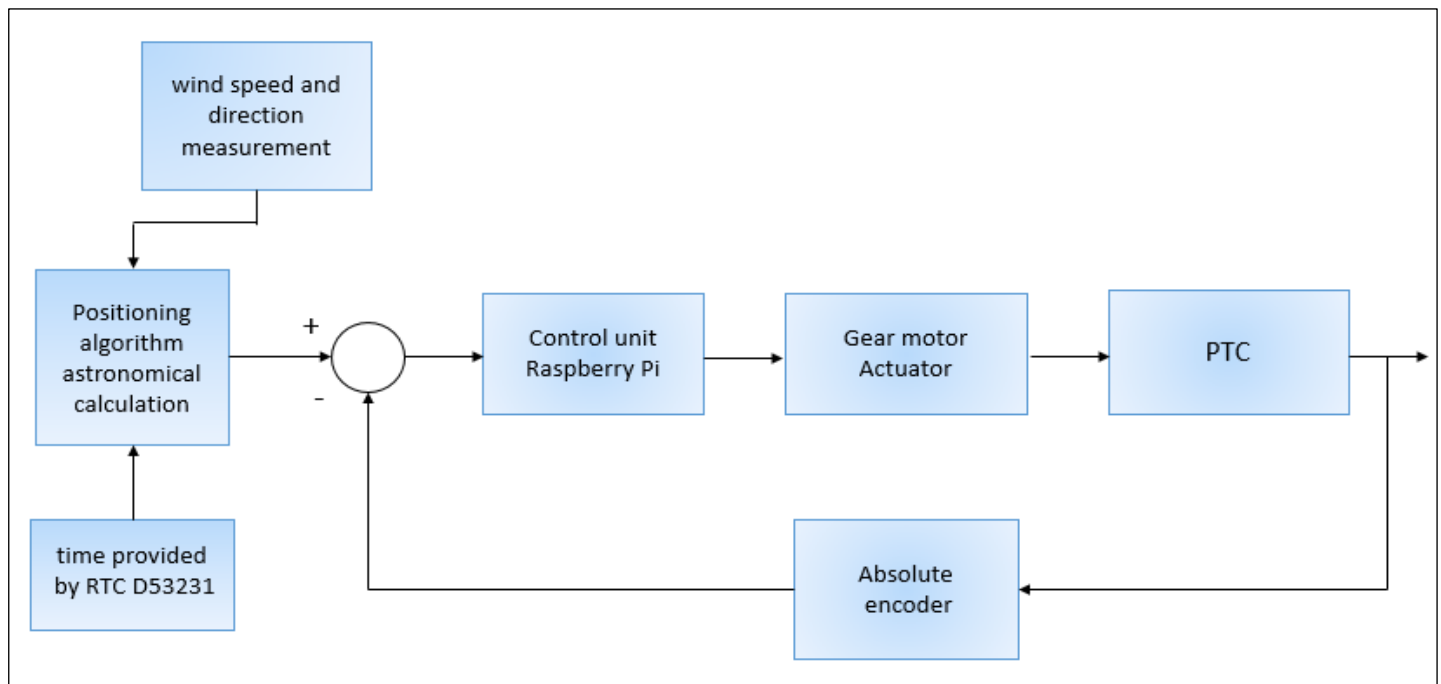


Figure 16: Position control system.
Source: Authors, (2023).

III.2.14 Command Signal and Control Algorithm

The solar tracking control driven by the slewing actuator only requires incremental corrections in the angle of the tracking system to achieve effective solar tracking [28].

The motor will only move when a position error is detected. The resolution of the tracking system is adjusted, for PTC, 0.5° is adequate according to the diameter of the absorber tube.

As a control philosophy, it is also used the obligation that at the end of the day, the PTC must be at rest position and ten minutes before the next day's sunrise it will go to the zero position, being available to start tracking. In the case of detecting wind speeds higher than the allowed limit, the monitoring is stopped by bringing the collector to the safety position, leaving it only when the wind speed returns to the limits established for the protection of the PTC during a determined period.

IV. RESULTS AND DISCUSSIONS

The validation of the control algorithm is performed using the MATLAB tool, a high-performance technical computing environment [43] that integrates numerical analysis, matrix computation, signal processing, and graphics. Figure 17 shows the flowchart describing the process of the implemented solar tracking algorithm, from which the tests are performed.

In this environment, the performance of the system based on astronomical calculations, implemented in the Raspberry Pi, was evaluated for the determination of solar angles and other variables such as solar time, solar azimuth, solar height, sunrise, and sunset for different days of the year. Figure 17 shows the flowchart describing the process of the implemented solar tracking algorithm, from which the tests are performed.

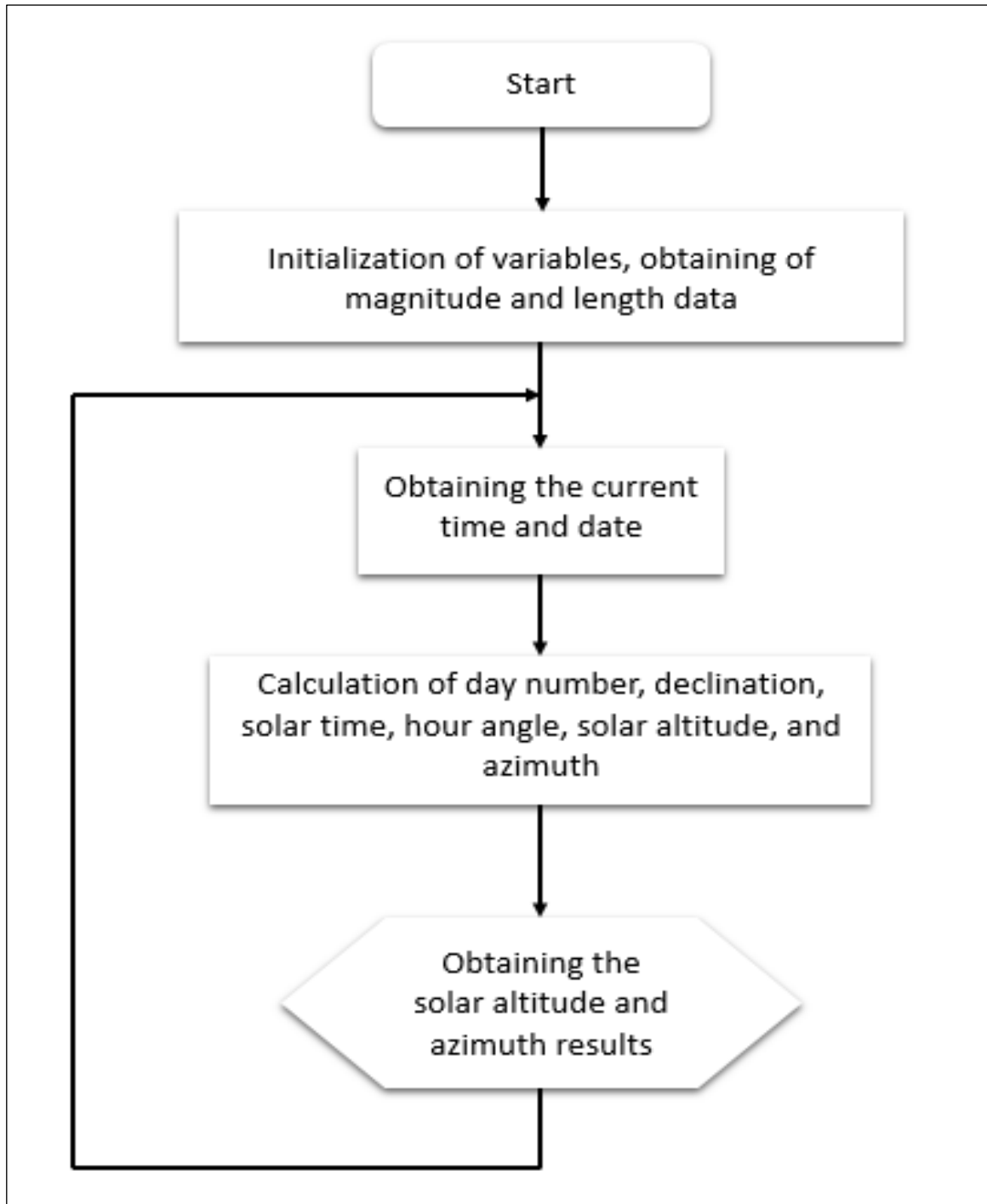


Figure 17: Block diagram of the designed algorithm.
Source: Authors, (2023).

As a result of the execution of this algorithm, Figures 18 and 19 show the behavior of the azimuthal angle and the solar elevation angle obtained by the system according to the latitude and longitude data of the city of Santa Clara, belonging to the province

of Villa Clara, Cuba on September 22, 2021, day in which the autumnal equinox takes place, between the time of Sunrise (7:12:55 AM) and Sunset (7:10:56 PM).

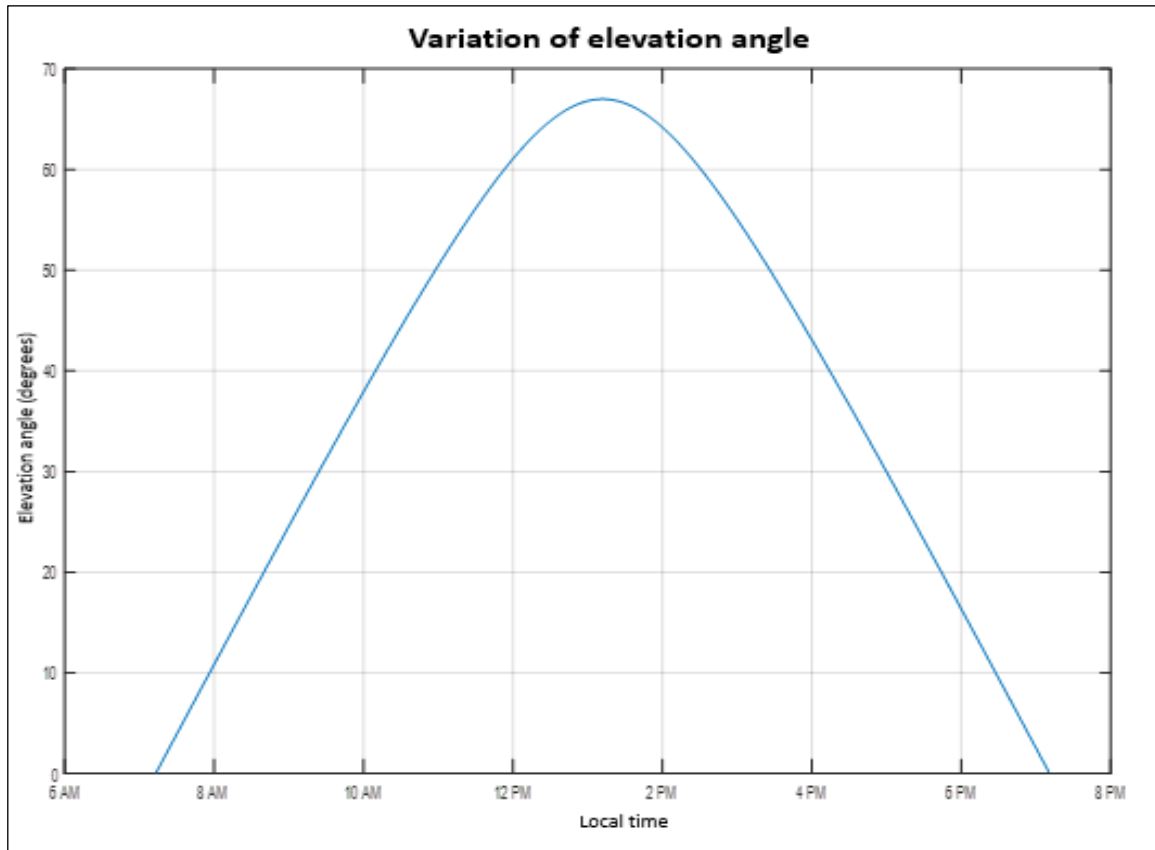


Figure 18: Behavior of the solar elevation angle.
Source: Authors, (2023).

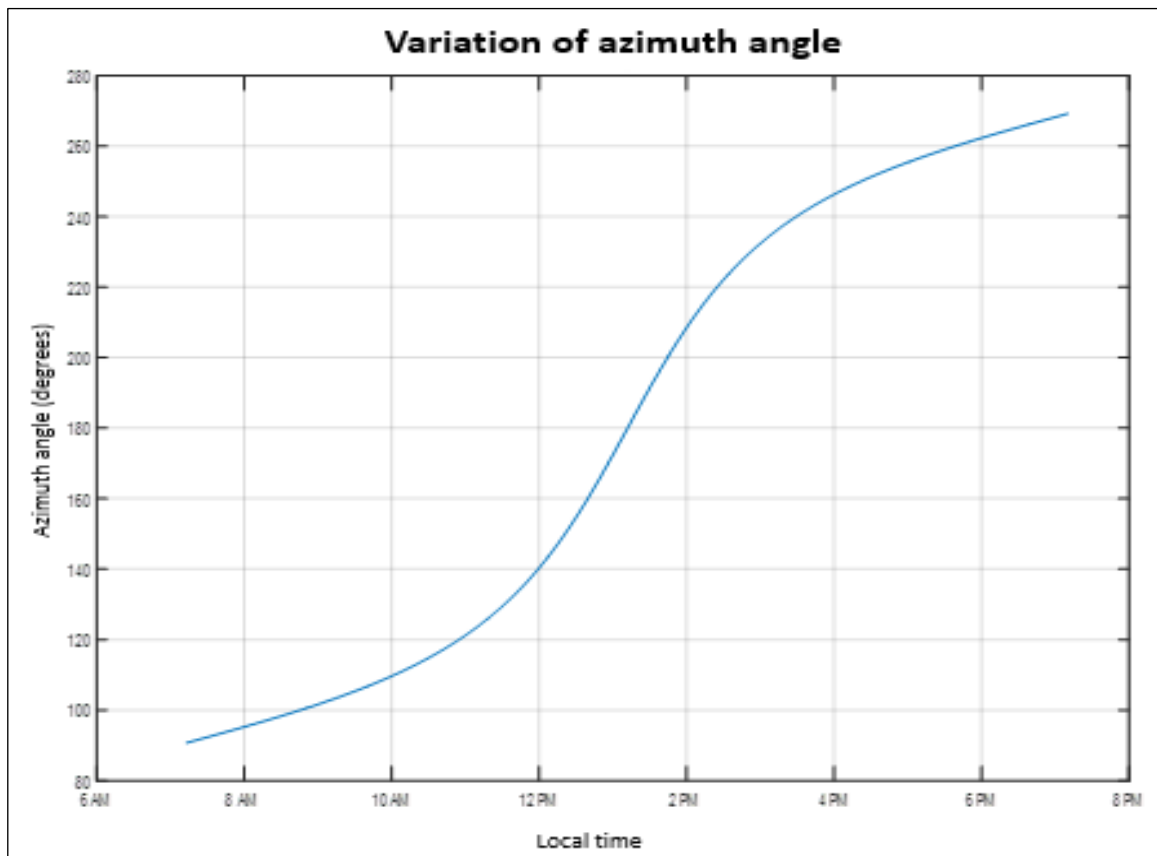


Figure 19: Behavior of the solar azimuth angle.
Source: Authors, (2023).

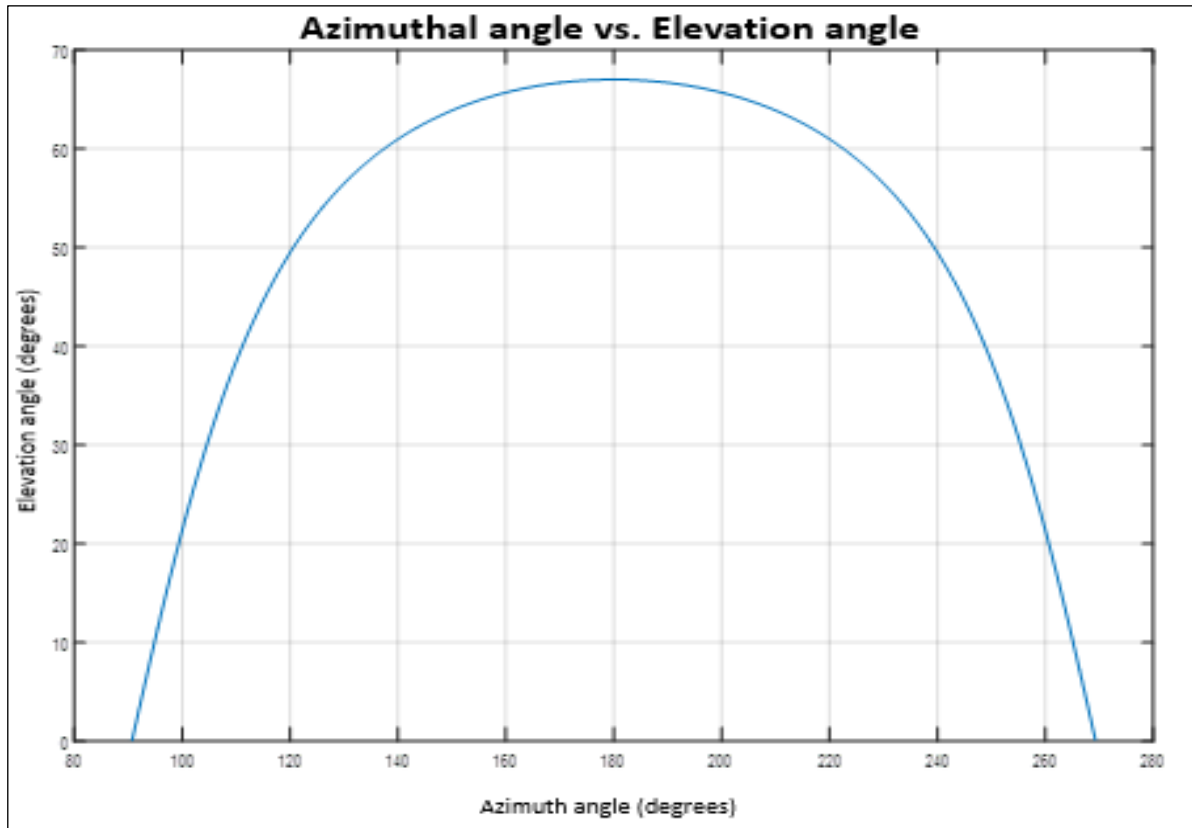


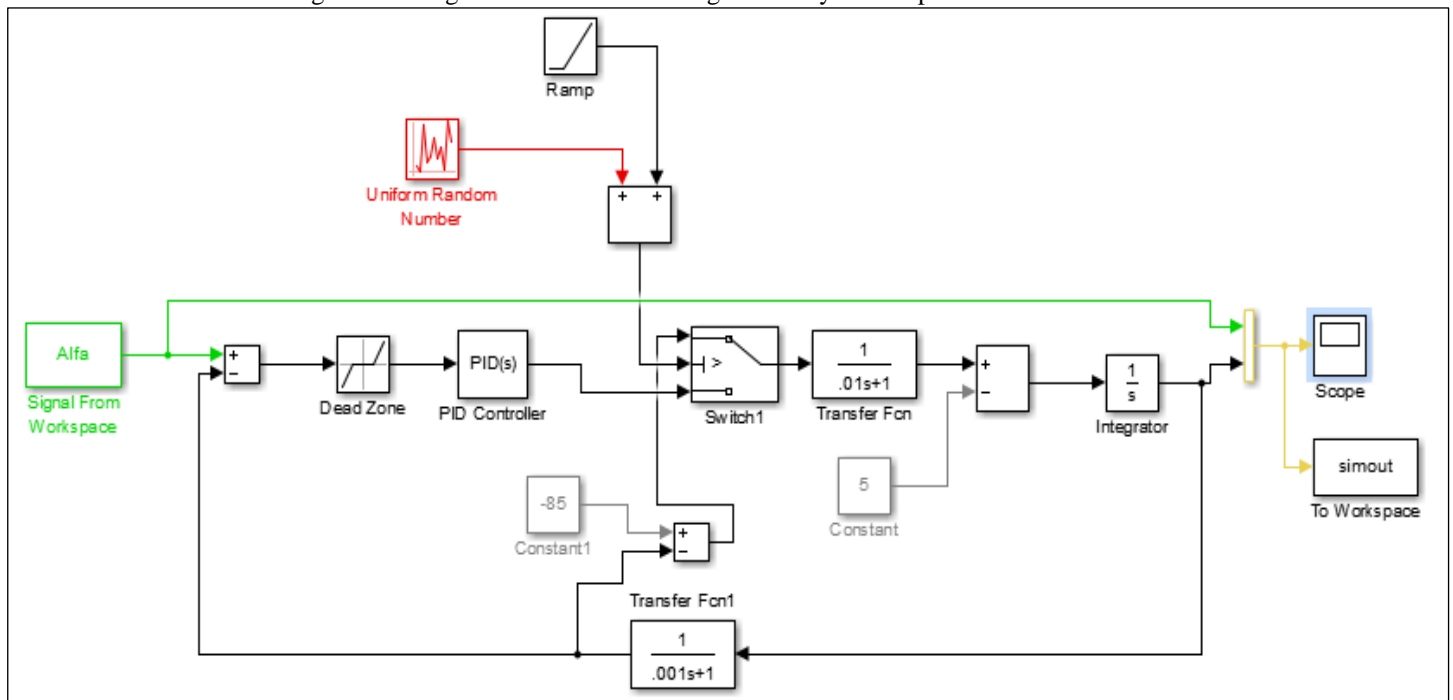
Figure 20: Behavior of the solar azimuth angle together with the solar elevation angle.
Source: Authors, (2023).

For these tests, an equinox day was chosen since it is the time of the year when day and night have the same duration.

Knowing the effectiveness of the tracking algorithm through astronomical programming using MATLAB Simulink, the behavior of the control system to follow the calculated ideal

position and its response in the presence of strong gusts of wind is evaluated. Figure 21 shows the diagram used to evaluate the behavior of the system with the designed controller when it is perceived that the velocity of the wind exceeds the limit established for the application.

Figure 21: Diagram of the solar tracking control system implemented in Simulink.



Source: Authors, (2023).

As shown in the previous figure, the control system also has a Proportional Integral Derivative (PID) controller to ensure the correct behavior of the tracking system in a steady state. Figure 22 shows the behavior of the system with the controller to a change in the reference input unitary step type.

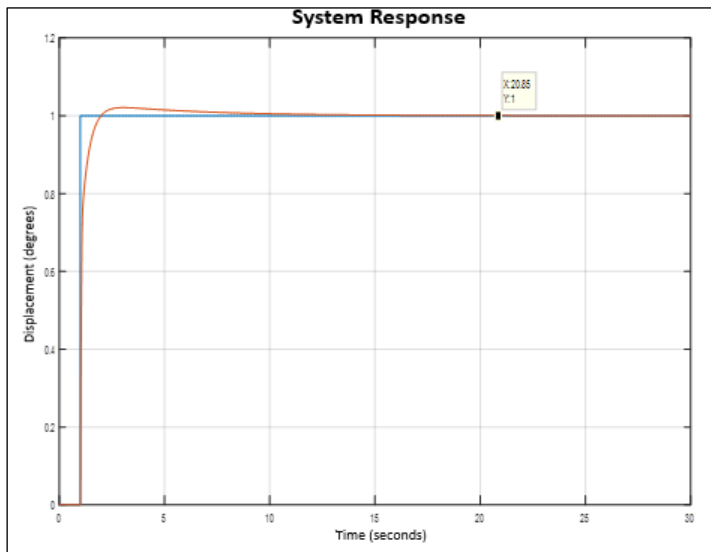


Figure 22: Response of the system with the designed PID.
Source: Authors, (2023).

As can be seen, the controller stabilizes at approximately 20.85 seconds and with a maximum overshoot practically null.

When the wind speed exceeds the limit value determined by the programming, the collectors are directed to a safe position below the horizontal. Figure 23 shows the behavior of the system under wind disturbance.

V. CONCLUSIONS

The designed position control algorithm for the Parabolic Solar Concentrators Through Collectors guarantees the correct tracking of the sun and the safety of the collectors under strong wind gusts. In addition, the correct selection of the hardware and software elements that compose the system allows the proper connection, integration, and operation of the system, designed according to the system requirements. The designed PID controller guarantees a fast response and ensures a correct steady-state operation. The position control using the astronomical programming method for calculating the solar position yielded excellent results.

VI. AUTHOR'S CONTRIBUTIONS

Conceptualization: José Abreu García, Ariel Barreiros Albo and Lianet Consuegra Morales.

Methodology: José Abreu García, Ariel Barreiros Albo and Lianet Consuegra Morales.

Investigation: José Abreu García, Ariel Barreiros Albo and Lianet Consuegra Morales.

Discussion of results: José Abreu García, Ariel Barreiros Albo and Lianet Consuegra Morales.

Writing – Original Draft: José Abreu García, Ariel Barreiros Albo and Lianet Consuegra Morales.

Writing – Review and Editing: José Abreu García, Ariel Barreiros Albo and Lianet Consuegra Morales.

Resources: José Abreu García, Ariel Barreiros Albo and Lianet Consuegra Morales.

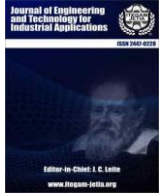
Supervision: José Abreu García, Ariel Barreiros Albo and Lianet Consuegra Morales.

Approval of the final text: José Abreu García, Ariel Barreiros Albo and Lianet Consuegra Morales.

VII. REFERENCES

- [1] K. Solangi, M. Islam, R. Saidur, N. Rahim, and H. Fayaz, "A review on global solar energy policy," *Renewable and sustainable energy reviews*, vol. 15, no. 4, pp. 2149-2163, 2011.
- [2] B. J. I. Nuñez, "Diseño y construcción de un concentrador solar lineal tipo Fresnel didáctico.," Universidad Del Zulia, 2016.
- [3] J. C. López Valdés, "Análisis de variantes de sistemas fotovoltaicos con seguimiento solar en las condiciones de Cuba," Universidad Central "Marta Abreu" de Las Villas, Facultad de Ingeniería Eléctrica, 2017.
- [4] D. J. Arrieta Morelo and S. Y. Puello Bravo, "Diseño y construcción de un seguidor solar para aumentar el rendimiento energético en paneles fotovoltaicos de un sistema de bombeo," 2018.
- [5] A. J. Abdulhamed, N. M. Adam, M. Z. A. Ab-Kadir, and A. A. Hairuddin, "Review of solar parabolic-trough collector geometrical and thermal analyses, performance, and applications," *Renewable and Sustainable Energy Reviews*, vol. 91, pp. 822-831, 2018.
- [6] A. Amelia, Y. Irwan, I. Safwati, W. Leow, M. Mat, and M. S. A. Rahim, "Technologies of solar tracking systems: A review," in *IOP Conference Series: Materials Science and Engineering*, 2020, vol. 767, no. 1, p. 012052: IOP Publishing.
- [7] D. I. K. Cardozo and E. A. M. Jara, "Automatización de Panel Solar," *FPUNE Scientific*, no. 5, 2014.
- [8] A. R. M. Cancio, "Análisis del estado del arte del calentamiento de agua con energía solar: Minirevisión," *Márgenes*, vol. 4, no. 2, pp. 58-85, 2016.
- [9] W. AJBAR, "Sistema de concentradores solares de canal parabólico para la generación de calor de proceso: diseño, construcción y modelado matemático," 2019.
- [10] C. Paredes Velasco, "Diseño de captador solar cilíndrico parabólico para aplicaciones rurales en Paraguay," 2012.
- [11] V. P. Arellano Mancheno and A. L. Chamorro Páez, "Diseño y construcción de un calentador solar cilíndrico parabólico con fines investigativos para la Escuela de Ingeniería Mecánica," Escuela Superior Politécnica de Chimborazo, 2017.
- [12] G.-F. Power-Porto, "Estudio de prefactibilidad para la instalación de una planta generadora de electricidad de 120 MW por medio de concentradores solares cilíndricos parabólicos," 2019.
- [13] D. Mentado-Islas, S. Elizalde-Carrizo, D. Jiménez-Islas, and J. Azuara-Jiménez, "Simulación de un concentrador solar de canal parabólico mediante el software SolTrace," *Revista de Prototipos Tecnológicos*, p. 68, 2016.
- [14] C.-Y. Lee, P.-C. Chou, C.-M. Chiang, and C.-F. Lin, "Sun tracking systems: a review," *Sensors*, vol. 9, no. 5, pp. 3875-3890, 2009.
- [15] A. M. Pérez Sánchez, "Diseño y evaluación de un campo de concentradores solares integrados en el esquema de fluido térmico de la Empresa textil "Desembarco del Granma", Universidad Central" Marta Abreu" de Las Villas. Facultad de Ingeniería ..., 2017.
- [16] C. F. Iglesias Forns, "Diseño y fabricación de un motor Stirling de bajo diferencial de temperatura para la generación de energía eléctrica, mediante energía solar térmica," Universidad Autónoma de Nuevo León, 2019.
- [17] H. M. Castro Chamorro, "Análisis técnico y financiero de plantas de concentración solar con tecnología de cilindro parabólico en las Islas Galápagos," Quito, 2021., 2021.
- [18] C. Echevarría López, "Diseño de un colector cilindro parabólico compuesto con aplicación para el calentamiento de agua," 2012.
- [19] G. R. Barrera, "Prototipo de un colector solar parabólico para la generación de energía eléctrica," *UGCiencia*, vol. 22, no. 1, pp. 149-158, 2016.

- [20] J. Quinteros Grijalva, "Estudio teórico y experimental de colector solar parabólico para generación de energía eléctrica," 2008.
- [21] A. T. Morales, "Adaptación de algoritmo de posicionamiento solar embebido con aplicación en energía solar," 2019.
- [22] J. F. Moreno, "Estudio comparativo de eficiencias térmicas en colectores solares cilindro parabólicos utilizando diferentes sustancias de trabajo.," Instituto tecnológico de Pachuca, 2015.
- [23] J. A. Carballo, J. Bonilla, L. Roca, and M. Berenguel, "New low-cost solar tracking system based on open source hardware for educational purposes," *Solar Energy*, vol. 174, pp. 826-836, 2018.
- [24] S. Naveen, M. A. A. Baig, and A. Saxena, "A novel scheme for dynamically tracking solar panel," *IOSR J Mech Civil Eng*, vol. 16, pp. 29-35, 2017.
- [25] B. K. S. Vastav, S. Nema, P. Swarnkar, and D. Rajesh, "Automatic solar tracking system using DELTA PLC," in *2016 International Conference on Electrical Power and Energy Systems (ICEPES)*, 2016, pp. 16-21: IEEE.
- [26] A. Marrero Valdivia, "Control de paneles solares fotovoltaicos," Universidad Central "Marta Abreu" de Las Villas. Facultad de Ingeniería ..., 2017.
- [27] K. M. Velázquez Lucho, "Construcción y evaluación de un concentrador solar de canal parabólico para calor de proceso de baja entalpía," 2014.
- [28] O. A. Calzadilla Napoles, "Control de posición de Concentradores Solares de Canal Parabólico mediante accionamiento hidráulico," 2020.
- [29] G. Prinsloo and R. Dobson, "Solar Tracking: High Precision Solar Position Algorithms, Programs, Software, and Source-Code for Computing the Solar Vector, Solar Coordinates," *Sun Angles in Microprocessor, PLC, Arduino, PIC and PC-Based Sun Tracking Devices or Dynamic Sun Following Hardware. E-Book*, 2014.
- [30] R. P. Foundation. (2021, 20 agosto). *Raspberry Pi 1 modelo B+*. Available: <https://www.electronicoscaldas.com/es/boards-raspberry-pi/800-raspberry-pi-1-modelo-b-plus.html>
- [31] A. Martín Montero, "Programación y control de un reloj de tiempo real con Raspberry Pi," 2018.
- [32] Adafruit. (2012, 16 de julio). *Adicionando un reloj en tiempo real para Raspberry Pi (1 ed.)*. Available: <https://learn.adafruit.com/adding-a-real-time-clock-to-raspberry-pi?view=all>
- [33] Tiendatec. (2021, 2 de septiembre). *Módulo ZS-042ZS-042 , reloj en tiempo real RTC basado en DS3231 AT24C32* Available: <https://www.tiendatec.es/arduino/modulos/400-modulo-zs-042-reloj-en-tiempo-real-rtc-basado-en-ds3231-at24c32-arduino-y-raspberry-pi-8404001180013.html>
- [34] Baumer, "Encoder Absoluto HMG 161," in *HMG 161 datasheet*, ed, 2021.
- [35] Dusco.E. (2021, 18 de septiembre). *Módulo LCD 1602, pantalla azul 1602 i2c, módulo de pantalla LCD HD44780, caracteres 16x2 5V, Serial IIC Jumpr Wire para Arduino ,Raspberry Pi.* Available: <https://es.aliexpress.com/item/32370241702.html>
- [36] Adafruit. (2021, 15 de septiembre). *4-channel I2C-safe Bi-directional Logic Level Converter - BSS138*. Available: <https://www.adafruit.com/product/757>
- [37] R. Estrada Marmolejo. (2016, 19 de septiembre). *Optoacoplador, qué es y como funciona.* Available: <http://www.google.com/amp/s/hetpro-store.com/TUTORIALES/optoacoplador/amp/>
- [38] Waveshare. (2021, 15 de julio). *Batería de polímero de litio para Raspberry Pi SW6106 Power Bank Solution con circuitos de protección integrados* Available: <https://www.amazon.com/-/es/Waveshare-Raspberry-circuitos-protecci%C3%B3n-integrados/dp/B07YZK24RT>
- [39] E. Balado Leal, "Prototipo de campo de colectores solares cilindro-parabólicos para generación de calor a alta temperatura," 2011.
- [40] L. A. Aros Salazar, "Proyectar estación meteorológica con Raspberry Pi 4 Modelo B," Universidad Técnica Federico Santa María, Chile, 2020.
- [41] Adafruit. (2021, 10 de septiembre). *Anemómetro Analógico*. Available: <https://www.pcfactory.cl/producto/29017-adafruit-anemometro-analogico>
- [42] CALT. (2021, 18 de octubre). *Sensor de dirección del viento 5 V CC fuente 0 – 2,5 V voltaje de salida CALT YGC-FX* Available: <https://www.amazon.com/-/es/Sensor-direcci%C3%B3n-del-viento-fuente/dp/B07GNY8XYB>
- [43] L. Bravo Ballén and F. Quevedo Sánhez, "MATLAB 6.1," Ciencias Económicas, Universidad Nacional de Colombia, Colombia, 2014.








RESEARCH ARTICLE OPEN ACCESS

ESCHERICHIA COLI BACTERIAL COLONIES IN PATIENTS WITH URINARY TRACT INFECTIONS USING FRESH AND STORED URINE SPECIMENS

Vincentia Ade Rizky*¹, Sa'adah Siregar², Asvia Rahayu³, Visensius Krisdianilo⁴ and Novita Trisna Murti⁵

^{1, 2, 3, 4, 5} Medical Laboratory Technology, Faculty of Pharmacy, Institut Kesehatan Medistra Lubuk pakam. Indonesia.

¹ <http://orcid.org/0000-0002-2866-1236> , ² <http://orcid.org/0000-0002-0664-4873> , ³ <http://orcid.org/0000-0002-2638-4917> , ⁴ <http://orcid.org/0000-0001-9888-9933> , ⁵ <http://orcid.org/0000-0002-8244-0602> 

Email: *vincentiarizky@gmail.com, ghozalirusman@gmail.com, asviarahayu@gmail.com, chrizdianilo@gmail.com, novitatrismamurti@gmail.com

ARTICLE INFO

Article History

Received: February 16th, 2023
Accepted: February 25th, 2023
Published: Month 28th, 2023

Keywords:

UTI,
Fresh Urine,
Urine Stored,
Calculation of the Number of Bacterial Colonies.

ABSTRACT

Urinary Tract Infection (UTI) is one of the most common bacterial infections that affects around 40% of women in their lives. Diagnosis of UTI is very necessary to determine the steps in treatment. Counting the number of bacteria is the gold standard for determining the severity of a UTI. In some hospitals, urine samples are often sent to the laboratory in conditions that are not fresh, even though the examination of bacteria in the urine must be carried out immediately, because storage of bacterial examination causes the development of bacteria, so that the growing colonies do not show the actual number of bacteria in the urine at the time of collection. to determine the results of examination of Escherichia coli bacteria on the urine of patients with Urinary Tract Infection (UTI) with urine that is examined immediately and stored. Urine culture on EMBA (Eosin Methylene Blue Agar) media , with a sample of 15. In this examination, an examination of the sample was planted on EMBA (Eosin Methylene Blue Agar) media and then viewed macroscopically. Then observed under a microscope with gram staining, after that it was planted on PCA (Plate Count Agar) media and then counted the number of colonies. The results of research that has been carried out on 15 urine samples of patients with a diagnosis of Urinary Tract Infection (UTI) which were examined immediately and stored for 15 and 30 minutes showed that the number of bacteria in the samples with variations in storage showed an increase at 30 minutes, whereas at 0 and 30 minutes 15 minutes there is no significant difference. Based on the research that has been done, it can be concluded that the number of bacterial colonies has increased, especially at the 30th minute, so it is hoped that the bacterial culture examination of UTI sufferers will be carried out before 30 minutes.



Copyright ©2023 by authors and Galileo Institute of Technology and Education of the Amazon (ITEGAM). This work is licensed under the Creative Commons Attribution International License (CC BY 4.0).

I. INTRODUCTION

Urinary Tract Infection (UTI) is one of the most common bacterial infections that affects around 40% of women in their lives [1]. Although most UTIs are mild, these infections can also cause life-threatening sepsis. The most serious cause of UTIs is bacteria, but fungal, viral and parasitic infections can also be causes. Bladder infection or cystitis is the most common form of

UTI but infection can occur in any part of the urinary tract, which can cause pyelonephritis, urethritis and prostatitis, among others.

Urinary Tract Infection (UTI) is an infectious disease that is often found in general practice. Several studies have shown that there are factors that can cause UTIs such as age, gender, long lying down, use of immunosuppressant and steroid drugs, catheterization, urinary retention habits, genital hygiene, and predisposing factors [2].

One important condition that needs to be considered in UTI symptoms is bacteriuria. Bacteriuria is a condition where bacteria can be found in the urine, but this condition does not always mean UTI. Bacteriuria is often asymptomatic. Bacteriuria is often known by another term, namely pyuria, which means a condition in which leukocytes are found in the urine. Leukocytes in the urine is a sign that there is an inflammatory response due to a bacterial infection. UTI clinical symptoms vary depending on age, the intensity of the inflammatory reaction and the location of the infection in the urinary tract. Children aged 2 months – 2 years who suffer from UTIs need special attention because of the atypical clinical symptoms, invasive methods of obtaining urine samples, and having the greatest risk of kidney damage. After the first episode, UTI can recur in 30-40% of patients, especially in patients with anatomic abnormalities, such as vesicoureteral reflux, hydronephrosis, urinary obstruction, bladder diverticulum, and others. The main management of patients is to maintain urinary tract function and improve the patient's quality of life by immediately handling urination so that there is no interference with urine elimination [3].

According to the National Kidney and Urologic Diseases Information Clearinghouse (NKUDIC), UTI ranks second after upper respiratory infection (ARI) and as many as 8.3 million cases are reported per year. UTIs can affect patients of all ages, from newborns to the elderly. Women suffer from UTIs more often than men, approximately 50% of all women have suffered from UTIs in their lifetime. Even women often experience recurrent UTIs which can interfere with their social life [4].

According to the Ministry of Health of the Republic of Indonesia, the number of UTI sufferers in Indonesia is still quite a lot, reaching 90-100 cases per 100,000 population per year or around 180,000 new cases per year [5].

Diagnosis of UTI is very necessary to determine the steps in treatment. The bacterial count is the gold standard for confirming a UTI. The results of counting the number of bacteria in the urine are used to determine the degree of severity of UTI, namely mild severity of 10^3 CFU/mL, moderate around 10^4 CFU/mL, and severe if it reaches 10^5 CFU/mL. In several hospitals, urine samples are often sent to the laboratory in

conditions that are not fresh, even though the examination of bacteria in the urine must be carried out immediately, because delays in the examination cause the development of bacteria, so that the colonies that grow do not show the actual number of bacteria in the urine at the time of collection [6].

According to the Clinical and Laboratory Standard Institute (CLSI) it is recommended that urine tests be carried out no later than 2 hours from the time urine is urinated. Urine delay for 2 hours without being stored at 2-8°C and the addition of preservatives can reduce the quality of urine examination results. Urine examination results that change due to delays in examination cannot properly describe the patient's condition, so that it can be an error in diagnosis [7]. In Sirait's study, it showed that the bacteria numbered 7.5×10^4 CFU/ml was delayed for 6 hours, when the delay was 12 hours there was an increase of 1.2×10^5 CFU/ml, but when the delay was 18 and 24 hours it decreased to 8.0×10^4 CFU/ml and 7.8×10^4 CFU/ml. Examinations at the hospital are often delayed due to the delivery of urine specimens from the room for inpatients and the large number of patients is a concern for further research to determine the amount of Escherichia coli using urine that is checked immediately and stored tests [8].

II. MATERIALS AND METHODS

This type of research is an experimental research. The population in this study were sufferers who experienced urinary tract infections caused by Escherichia coli bacteria at Grandmed Lubuk Pakam Hospital, the number of samples that would be used as respondents in this study were 15 respondents. The research sample taken was urine found in people who had urinary tract infections.

III. RESULTS AND DISCUSSIONS

Culture specimen in Eosin Methylene Blue Agar media and incubated for 24 hours at 37 ° C in an incubator with the following results (show in table 1):

Table 1: Culture Results on EMBA Media (Eosin Methylene Blue Agar).

Specimen No	Results		
	In the 0th minute	In the 15th minute	In the 30th minute
1	Round Colonies, Metallic Green Color	Round Colonies, Metallic Green Color	Round Colonies, Metallic Green Color
2	Round Colonies, Metallic Green Color	Round Colonies, Metallic Green Color	Round Colonies, Metallic Green Color
3	Round Colonies, Metallic Green Color	Round Colonies, Metallic Green Color	Round Colonies, Metallic Green Color
4	Round Colonies, Metallic Green Color	Round Colonies, Metallic Green Color	Round Colonies, Metallic Green Color
5	Round Colonies, Metallic Green Color	Round Colonies, Metallic Green Color	Round Colonies, Metallic Green Color
6	Round Colonies, Metallic Green Color	Round Colonies, Metallic Green Color	Round Colonies, Metallic Green Color
7	Round Colonies, Metallic Green Color	Round Colonies, Metallic Green Color	Round Colonies, Metallic Green Color
8	Round Colonies, Metallic Green Color	Round Colonies, Metallic Green Color	Round Colonies, Metallic Green Color
9	Round Colonies, Metallic Green Color	Round Colonies, Metallic Green Color	Round Colonies, Metallic Green Color
10	Round Colonies, Metallic Green Color	Round Colonies, Metallic Green Color	Round Colonies, Metallic Green Color
11	Round Colonies, Metallic Green Color	Round Colonies, Metallic Green Color	Round Colonies, Metallic Green Color
12	Round Colonies, Metallic Green Color	Round Colonies, Metallic Green Color	Round Colonies, Metallic Green Color
13	Round Colonies, Metallic Green Color	Round Colonies, Metallic Green Color	Round Colonies, Metallic Green Color
14	Round Colonies, Metallic Green Color	Round Colonies, Metallic Green Color	Round Colonies, Metallic Green Color
15	Round Colonies, Metallic Green Color	Round Colonies, Metallic Green Color	Round Colonies, Metallic Green Color

Source: Authors, (2023).

Based on the results obtained, specimens 1-15 actually cultured urine specimens at 0, 15 and 30 minutes showing round, metallic green colonies. Based on the culture results in the EMBA media, it shows that it is a colony of the Enterobacteriaceae family.

After culturing on EMBA media, microscopic examination was then carried out to ensure the growing bacterial colonies. the results can be seen in table 2.

Table 2: Gram Staining Results.

Specimen No	Results		
	In the 0th minute	In the 15th minute	In the 30th minute
1	Basil, Gram Negative	Basil, Gram Negative	Basil, Gram Negative
2	Basil, Gram Negative	Basil, Gram Negative	Basil, Gram Negative
3	Basil, Gram Negative	Basil, Gram Negative	Basil, Gram Negative
4	Basil, Gram Negative	Basil, Gram Negative	Basil, Gram Negative
5	Basil, Gram Negative	Basil, Gram Negative	Basil, Gram Negative
6	Basil, Gram Negative	Basil, Gram Negative	Basil, Gram Negative
7	Basil, Gram Negative	Basil, Gram Negative	Basil, Gram Negative
8	Basil, Gram Negative	Basil, Gram Negative	Basil, Gram Negative
9	Basil, Gram Negative	Basil, Gram Negative	Basil, Gram Negative
10	Basil, Gram Negative	Basil, Gram Negative	Basil, Gram Negative
11	Basil, Gram Negative	Basil, Gram Negative	Basil, Gram Negative
12	Basil, Gram Negative	Basil, Gram Negative	Basil, Gram Negative
13	Basil, Gram Negative	Basil, Gram Negative	Basil, Gram Negative
14	Basil, Gram Negative	Basil, Gram Negative	Basil, Gram Negative
15	Basil, Gram Negative	Basil, Gram Negative	Basil, Gram Negative

Source: Authors, (2023).

Based on the results obtained, specimens 1-15 actually examined the bacterial colonies at 0, 15 and 30 minutes, showing positive gram-negative bacilli results. It can be seen in Bergey's book that the two results that have been carried out show that the bacterial colonies are *Escherichia coli* bacteria.

III.1 ON PCA MEDIA (PLATE COUNT AGAR)

Urine specimens as many as 15 specimens that have been obtained are immediately examined, then examination is carried

out on storage specimens at the 15th and 30th minutes. The results of direct examination calculations, 15 and 30 minutes showed the number of bacteria in the specimen was $\geq 10^5$ CFU/ml. After that, the calculation of the average bacteria in units (10^5 CFU/ml) was carried out to find out the differences in the three storage treatments, the results of the calculations can be seen in Table 3. Then the results of the average calculation of the number of colonies on the media can be seen in table 4.

Table 3: Colony Count Results at 0 Minutes (Immediate), 15 Minutes and 30 Minutes.

Specimen No	Results		
	In the 0th minute	In the 15th minute	In the 30th minute
1	1.05	1.17	1.38
2	1.10	1.20	1.40
3	1.10	1.16	1.36
4	1.50	1.16	1.40
5	1.02	1.21	1.45
6	1.00	1.17	1.36
7	1.40	1.30	1.39
8	1.10	1.31	1.50
9	1.05	1.17	1.51
10	1.10	1.21	1.37
11	1.00	1.30	1.37
12	1.11	1.17	1.37
13	1.70	1.16	1.47
14	1.00	1.18	1.54
15	1.50	1.33	1.37

Source: Authors, (2023).

Table 4: The average value of bacteria in each variation of examination storage time.

No	Minute Storage	Number of Specimens	Bacterial mean value (10^5 CFU/ml)
1	0	15	1.18
2	15	15	1.21
3	30	15	1.42

Source: Authors, (2023).

The table above shows that there is a difference in the average value of the results of direct examination and storage at the 15th and 30th minutes. The longer the examination, the average number of bacteria increases in units of 10^5 CFU/ml.

In this study using the urine culture method, urine examination on direct examination showed the number of bacteria in each specimen was $\geq 10^5$ CFU/ml. When compared with the Guidelines on Urological Infection, all specimens examined had a UTI with a severe degree of severity, but supporting examinations

such as leukocytes in the urine must also show $\geq 10^5$ white blood cells per high-power field (400x) for centrifuged urine specimens. Dipstick examination can be used for routine tests, such as leukocyte esterase, hemoglobin, and nitrite reactions. In complicated UTIs, there is usually an underlying disease. The bacteria that are often found are Gram negative bacteria such as *E.coli*, *Proteus*, *Klebsiella*, *Pseudomonas*, *Serratia*, and *Enterococci* [9-11].

The research that has been carried out is also supported by the research of Dewanti, which shows that there is an effect of delaying the 3-hour examination on the number of urinary leukocytes in UTI patients [12]. Likewise with research conducted by Nugraha, in his research it was shown that the duration of centrifugation of urine specimens affected the results of examination of urine leukocyte sediments in UTI sufferers, this was due to the large number of sediment deposits formed due to the centrifugation process and the high number of leukocytes [13].

The results of the delayed urine examination for each variation showed an increase in the number of bacteria, this was influenced by the composition in the urine. Urine is a liquid containing waste products from the body's metabolism, such as protein, dissolved salts such as sodium (Na⁺) and organic matter in the form of nitrates (NO₃) which are excreted through the urinary system [14,15]. These materials become nutrients or growth media, so that bacteria can grow and develop. Apart from nutrition, urine temperature which ranges from 32°C-38°C also supports bacterial growth, because bacterial metabolism is faster [16]. Nutritional content and temperature can cause bacteria to multiply if the inspection is delayed.

Another study conducted by Sirait [8], showed that at a delay of 6 hours, the number of bacteria was 75,050 CFU/ml, which increased to 128,000 CFU/ml at a delay of 12 hours, and at a delay of 18 hours, the number of bacteria began to decrease to 80,750 CFU/ml, then to 78,900 CFU./ml on a 24 hour delay.

In this study using SPSS data analysis. Based on the Normality test with an error rate of 5%, a significance value of 0.909 was obtained for all study specimens, this value was <0.05 which indicates that the data is normally distributed. Specimen Test Paired T-test as a follow-up test for Normality was carried out to find out the significant differences from each treatment, so that it can be interpreted that each storage variation showed an increase in the 30th minute, while at 0th and 15th minutes there was no significant difference.

IV. CONCLUSIONS

Based on the research results obtained, it can be concluded that urine specimens that were examined immediately and postponed showed an increase in urine specimens at 0, 15 and 30 minutes. It is hoped that urine culture examination will be carried out immediately without delay. This is because the more specimens are postponed, the more bacteria will increase.

V. AUTHOR'S CONTRIBUTION

Conceptualization: Vincentia Ade Rizky and Saadah Siregar.

Methodology: Vincentia Ade Rizky and Novita Trisna Murti.

Investigation: Asvia Rahayu and Visensius Krisdianilo.

Discussion of results: Vincentia Ade Rizky, Visensius Krisdianilo and Novita Trisna Murti.

Writing – Original Draft: Visensius Krisdianilo and Novita Trisna Murti.

Writing – Review and Editing: Saadah Siregar and Vincentia Ade Rizky.

Resources: Asvia Rahayu.

Supervision: Vincentia Ade Rizky.

Approval of the final text: Saadah Siregar and Asvia Rahayu.

VI. ACKNOWLEDGMENTS

Thank you to the Lubuk Pakam Medistra Health Institute for supporting the completion of this research.

VII. REFERENCES

- [1] C. W. Tan and M. P. Chlebicki, 'Urinary tract infections in adults', *Singapore Med. J.*, vol. 57, no. 9, pp. 485–490, Sep. 2016.
- [2] E. Irawan, 'Faktor-Faktor Penyebab Infeksi Saluran Kemih (ISK) (Literature Review)', *INA-Rxiv*, 19-Jul-2018.
- [3] S. O. Pardede, 'Infeksi pada ginjal dan saluran kemih anak: Manifestasi klinis dan tata laksana', *Sari Pediatri*, vol. 19, 2018.
- [4] Hermiyanty, 2016. Faktor Risiko Infeksi Saluran Kemih di Bagian Rawat Inap RSUD Mokopindo Tolitoli Tahun 2012, *Jurnal Kesehatan Tadulako*, 2, (2), 1-72.
- [5] R. I. Depkes, 'Survei Demografi dan Kesehatan Indonesia', *Jakarta : Depkes RI*, 2016.
- [6] Fitri, I. Triffit, and N. W. Diva, 'Pengaruh variasi lama penundaan pemeriksaan terhadap enumerasi bakteri pada urine penderita infeksi saluran kemih (ISK)', *Jurnal biologi dan pembelajarannya*, vol. 6, no. 2, 2019.
- [7] J. Delanghe and M. Speeckaert, 'Preanalytical requirements of Urineanalysis', *Biochemia Medica*, vol. 24, no. 1, pp. 89–104, 2014.
- [8] R. Sirait, *Penundaan Pemeriksaan Kulture Urine Pasien dengan Penyimpanan menggunakan Coolbox pada pertumbuhan Bakteri di RSUP Kariadi Semarang, KTI*. 2017.
- [9] R. Mittal, S. Anggarwal, S. Sharma, S. Chibber, and K. Harjai, 'Urinary Tract Infections Caused By Pseudomonas Aeruginosa: a Mnireview', *Journal Infect Public Health*, vol. 2, pp. 101–111, 2009.
- [10] K. C. Leung, A. H. C. Wong, A. A. M. Leung, and K. L. Hon, 'Urinary Tract Infection in children', *Recent Pat. Inflamm. Allergy Drug Discov.*, vol. 13, no. 1, pp. 2–18, Aug. 2019.
- [11] T. Bharara, S. Abha, G. Renu, D. D. Shalini, P. J. Pragnya, and K. Avinash, 'Predictive Role Proteinuria in Urinary Tract Infection', *Journal of Clinical and Diagnostic Research*, vol. 10, no. 11, pp. 1–3, 2017.
- [12] I. G. A. Sarihati, B. Dewanti, and B. Burhannuddin, 'PENGARUH PENUNDAAN PEMERIKSAAN URIN TERHADAP JUMLAH LEUKOSIT PADA PENDERITA INFEKSI SALURAN KEMIH', *Meditory: The Journal of Medical Laboratory*, vol. 7, pp. 7–12, Jul. 2019.
- [13] C. Nugraha, 'Pengaruh Lama Sentrifugasi Spesimen Urine Terhadap Hasil Pemeriksaan Sedimen Lekosit Urine Pada Penderita Infeksi Saluran Kemih (ISK) di Laboratorium D-III Analisis Kesehatan Universitas Indonesia Timur', *Jurnal Media Leboran*, vol. 9, no. 2, pp. 6–12, 2019.
- [14] U. Erdbrügger et al., 'Urinary extracellular vesicles: A position paper by the Urine Task Force of the International Society for Extracellular Vesicles', *J. Extracell. Vesicles*, vol. 10, no. 7, p. e12093, May 2021.
- [15] D. Purnomo and T. Untung, 'Sensitivity and Specificity of Urineanalysis to Diagnose UTI in Patient With Urolithiasis Sardjito General Hospital', *Indonesian Journal of Urology*, vol. 23, no. 2, pp. 130–134, 2016.
- [16] D. Krihariyani, 'Pengaruh Penyimpanan Urine Kultur Pada Suhu 20C-80C Selama Lebih Dari 24 Jam Terhadap Pertumbuhan Bakteri', *Jurnal Penelitian Kesehatan Forikes*, vol. 1, no. 2, 2010.



RESEARCH ARTICLE

OPEN ACCESS

MODIFIED BAT ALGORITHM FOR TRANSMISSION NETWORK EXPANSION PLANNING CONSIDERING ACTIVE POWER LOSSES

João Ricardo Paes de Barros*¹ and Dimitri Albuquerque de Barros²

¹ Electrical Power System Consultant and Research, Recife, Pernambuco, Brazil.

² Electrical Engineer, Recife, Pernambuco, Brazil.

¹ <http://orcid.org/0000-0001-9804-1983> , ² <http://orcid.org/0000-0003-4576-3514> 

Email: *jrpb64@gmail.com, dimitrialbuquerque@hotmail.com

ARTICLE INFO

Article History

Received: January 02th, 2023

Accepted: February 21th, 2023

Published: February 28th, 2023

Keywords:

Active power loss,
Bat Algorithm,
Metaheuristic,
Power system,
Transmission expansion planning.

ABSTRACT

This paper presents a metaheuristic algorithm, called BATp optimizer, to solve the combinatorial problem of static transmission networks expansion planning (STNEP) considering the effect of active power losses in the circuits. The optimizer is composed of two modules. One module generates candidate solutions, using the modified Bat Algorithm (BA), and the other that makes solutions with over costs or infeasibilities competitive. The modification made to the original BA consists in the inclusion of a local search intensification operator that acts on the elements of the current global optimal solution to improve the convergence rate and hinder stagnation in a suboptimal solution. The number of elements modified in the current global optimal solution is defined as a function of the number of buses and branches in the analyzed system. The size of the initial population is also defined as a function of the number of buses and branches. The active power losses are represented in the equality constraints of the mixed-integer nonlinear programming (MINLP) problem. The performance evaluation of the transmission network of the analyzed system is done by a linear power flow. The performance of the BATp optimizer was tested in three systems well known in the literature: the IEEE 24-bus and the South Brazilian - SB 46-bus. In each of the analyzed systems, situations were simulated with and without the possibility of generation redispatch. The BATp optimizer was able to find good results compared to those published in the literature, with relatively low computational effort.



Copyright ©2023 by authors and Galileo Institute of Technology and Education of the Amazon (ITEGAM). This work is licensed under the Creative Commons Attribution International License (CC BY 4.0).

I. INTRODUCTION

I.1 PURPOSE OF TNEP

Transmission network expansion planning - TNEP of any power electric system is a task of great importance, because it involves large investments in transmission lines, transformers, and substation and voltage control equipment. The TNEP aims to determine a transmission network capable of transporting the electric power produced in one or more generation centers (existing and future) to the load centers (existing and future) meeting technical, quality and security requirements, to minimize the costs involved in the expansion [1].

I.2 FACTORS THAT AFFECT TNEP

The TNEP depends on factors such as; i) locations of future generation and load centers; ii) topology of the existing transmission network; (iii) list of candidate circuits; (iv) electrical parameters and costs of candidate circuits; v) maximum allowed number of parallel circuits per branch; vi) mathematical model used to represent the transmission grid (via direct current - DC or via alternating current - AC); vii) number of years of the planning periods (one period or several periods); viii) reliability criteria (deterministic N-0, N-1, or probabilistic); ix) representation of power losses in the circuits; x) representation of uncertainties.

I.3 PLANNING PERIODS

Regarding the number of planning periods, TNEP has been classified as either static or dynamic [2]. When only the last year of the planning horizon is analyzed, the TNEP is called static TNEP (STNEP), and it is determined where and how many new circuits should be added to the existing transmission network. In [3] several articles are cited that address the STNEP problem.

When more than one year of the planning horizon is analyzed, the TNEP is called dynamic TNEP (DTNEP), and it is also determined when they should be added as well as where and how many. This model is more complex than the STNEP model due to the larger number of variables and constraints that must be considered in the mathematical model. In [1] and [4] several articles are cited that address the DTNEP problem.

I.4 SAFETY CONSTRAINTS

In both STNEP and DTNEP, the transmission grid can be expanded either to meet safety constraints (deterministic reliability criterion N-1, used in Brazil) [5], where all existing and future demand must be met without violations of circuit loading limits in the event of any simple contingency, or to meet the N-0 reliability criterion [6], where only part of the total system demand must be met in the event of any simple contingency. It is implicit in the deterministic N-1 criterion that transmission network sizing is done to meet the worst-case availability condition of the components.

II.5 POWER FLOW MODELS

With respect to the representation of the transmission network in the TNEP mathematical model, it can be done by a linear power flow model or a non-linear model. In [4] several papers are cited that have used these two models, pointing out the advantages and disadvantages of each.

The non-linear model, called the alternating current power flow (pfAC), despite being realistic, is complex due to the larger number of variables and restrictions that are considered. The linear model, called the direct current power flow (pfDC), on the other hand, is not complex. Therefore, it has been extensively used in TNEP studies because it calculates the active power flows in circuits in a simple, fast and accurate manner suitable for long-term planning studies.

I.6 ACTIVE POWER LOSSES

In the TNEP problem, there is a need to include parameters, variables, constraints and/or natural effects, to make the problem representation more realistic. A very important natural effect that should be considered in the mathematical modeling is related to power losses arising from the circulations of power flows in the transmission network circuits.

Despite representing a small percentage of the energy produced in the system, the consideration of power losses in the mathematical model is important due to the increase in generation output and, consequently, increase in power flows in the circuits. This fact may cause the need for additional investments if certain circuits are operating at the limit of their maximum transmission capacities. Thus, if losses are neglected, the circuits that are actually congested appear to be uncongested, resulting in no need for additional circuits and in different solution.

According to the specialized literature, three ways of including the effects of power losses have been used in the STNEP optimization model with losses (STNEPp): i) in the objective

function - OF (Table 1), ii) in the equality constraints - EC (Table 2) and iii) in the OF and EC (Table 3).

The Tables 1, 2 and 3 show the optimization algorithms that have been used in the published work Classical Optimization Algorithm (COA), Constructive Heuristic Algorithm (CHA) and Metaheuristic Algorithm - MHA), the power flow models (pfDC or pfAC) and systems generally used in the testing of the algorithms: Garver - 6 buses/15 branches (G-6/15); Modified Garver - 6 buses/15 branches (GM-6/15); IEEE - 24 buses/41 branches (IEEE-24/41); South Brazilian - 46 buses/79 branches (SB-46/79); North-West Iranian - 17 buses/21 branches (NWI-18/21); Hypothetical System - 8 buses/12 branches (HS-8/12); IEEE -9 buses/9 branches (IEEE-9/9); Spanish System - 425 buses/628 branches (SS-425/628) and North-East Iranian - 12 buses/21 branches (NEI-12/21).

Table 1: Active power loss represented in the OF.

Year, Ref.	PF Model	Algorithm	PES Tested
1988, [6]	pfDC	COA	G-6/15
2008, [6]	pfDC	MHA	G-6/15
2010, [6]	pfDC	MHA	NWI-18/21
2014, [6]	pfDC	MHA	G-6/15
2015, [6]	pfAC	MHA	G-6/15
2016, [6]	pfDC	MHA	GM-6/15
2021, [6]	pfDC	MHA	G-6/15, IEEE-24/41

Source: Authors, (2022).

Table 2: Active power loss represented in the EC.

Year, Ref.	PF Model	Algorithm	PES Tested
2003, [6]	pfDC	COA	G-6/15, IEEE-24/41 e SB-46/79
2005, [7]	pfDC	CHA	G-6/15 e SB-46/79
2006, [6]	pfAC	COA	HS-8/12
2008, [6]	pfDC	COA	G-6/15 e IEEE-24/41
2008, [6]	pfDC	COA	G-6/15, IEEE-24/41 e SB-46/79
2008, [6]	pfDC	MHA	SB-46/79
2011, [6]	pfAC	CHA	IEEE-9/9
2012, [8]	pfAC	COA	G-6/15 e NEI 12/21
2013, [6]	pfAC linearized	COA	G-6/15 e IEEE-118/177
2016, [6]	pfDC	COA	G-6/15, IEEE118/177 e SS-425/628
2018, [9]	pfDC	CHA	G-6/15, IEEE-24/41 e SB-46/79
2019, [10]	pfDC	COA	G-6/15
2020, [11]	pfDC	MHA	G-6/15 e SB-46/79
2022, [12]	pfDC	MHA	G-6/15, IEEE-24/41 e SB-46/79

Source: Authors, (2022).

Table 3: Active power loss represented in the OF and EC.

Year, Ref.	PF Model	Algorithm	PES Tested
2017, [13]	pfDC	COA	SB-46/79

Source: Authors, (2022).

I.7 SOLUTION ALGORITHMS

The STNEPp consists of a mixed-integer nonlinear programming (MINLP) problem that requires non-convex mathematical models with non-deterministic polynomial time (NP-hard) to be solved [14]. These particularities illustrate the

difficulties in designing algorithms that are robust, efficient, and fast to solve STNEPp problems, especially large systems.

The COA explore the entire search space, in general, find the global optimal solution for small to medium-sized power system with little computational effort. However, for real or large systems, they consume large computational effort and present a convergence problem [15]. For this reason, they in several situations, become inadequate [16].

The CHA does not explore the entire search space (space of candidate solutions), and use simplified procedures for exploring the search space (diversification and intensification). Therefore, they rarely find the global optimal solution for real or large systems [17], [18].

The MHA are inspired by natural processes and use a diversification procedure, where the entire search space is explored, and another intensification procedure, where only a specific part of the search space is explored, much more elaborate than the procedures used in CHA, to avoid premature convergence and escape from suboptimal solutions. According to [19] and [20], MHA, in the vast majority of cases, find the global optimal solution to complex problems with acceptable computational effort.

In view of the good trade-off between the quality of the proposed solution and the computational effort, MHA have been widely used to solve STNEP [21] and STNEPp problems, as shown in the researches indicated in the tables.

Some MHA are inspired by the nature and, as an example, can be cited those based on swarm intelligence, which implement the collectivity of groups formed by agents of nature such as birds, fireflies, bats, and others.

The Bat Algorithm (BA) [22] was inspired by the echolocation phenomenon that bats use during flight, and uses a pulse emission frequency tuning technique to balance diversification (general search in space) and intensification (local search in space). However, it sometimes fails to escape from a point of local optimum, causing it to converge to a suboptimal solution [23]. To improve the performance of the original BA, several works have been proposed, as shown in the papers by [24], [25], [26], [27], [28].

In [29] a CHA was employed to solve the STNEP problem, considering the standard BA to generate candidate solutions. The transmission network was represented by an pfCC. The algorithm proposed in [29] was tested on the G-6/15 and IEEE-24/41 systems.

1.8 PROPOSED ALGORITHM

To solve STNEPp problems, only article [30] applied the standard BA [22], as can be seen in the articles indicated in the tables. In this paper, the transmission network was represented by an pfCA and the proposed algorithm was tested on G-6/15 system. This scarcity shows that the application of BA-based MHA is open for discussion and research.

To fill this gap, this paper presents an algorithm, called the BATp optimizer, derived from the standard BA, where the search intensification mechanism has been changed aiming at improving the convergence rate and making it difficult to stagnate at a suboptimal solution. The proposed operator acts on the elements of the vector representing the position of the bat that is closest to the prey.

In the BATp optimizer, the STNEPp problem is represented by a MINLP problem, with the transmission network represented by an fpCC and the power losses included in the equality constraints.

The BATp optimizer is composed of a module that generates candidate solutions and another that uses the local improvement procedures proposed by [31] to make solutions that present load shedding and those that present over costs competitive. These procedures have also been successfully used in [5], [32] in STNEP studies considering security constraints. The joint application of these two procedures is important, especially, when analyzing large meshed systems.

The performance evaluation of the BATp optimizer was done with the IEEE-24/41 and SB-46/79 test systems.

The remainder of this paper is organized as follows: In the second section, the main concepts of the original BAT algorithm are presented. The third section presents the mathematical model used in the representation of STNEPp. The fourth section presents the structure and operation of the BATp optimizer. The fifth section presents the case studies and analysis of the results performed with the three systems mentioned above. The sixth section presents the main conclusions. And finally, the last two sections present the main conclusions and the bibliographical references.

II. BAT ALGORITHM

This section presents the main characteristics of the original BA and the proposed variant for generating candidate solutions to the STNEPp problem.

II.1 ORIGINAL BAT ALGORITHM

According to [22], BA is inspired by the sophisticated echolocation ability that bats of the microchiroptera species use during flights to detect prey and avoid obstacles. Echolocation is based on the emission of ultrasonic waves and measurements of the times taken for these waves to return to their sources after being reflected from targets (prey or obstacles) [33].

In BA, each virtual bat (i) occupies a position (x_i) in the hunting environment, flies randomly with speed (v_i) and emits sound waves with frequency (f_i) and amplitude (A_i). The frequency is related to the emitted wavelength. At each iteration of the algorithm, each virtual bat flies in the direction of the bat that is closest to the prey, i.e., it flies in the direction of the current leader bat (x_g). The Figure 1 illustrates a flock of Nm virtual bats positioned at various locations in a hunting environment of dimension (D), emitting sound waves to identify prey.

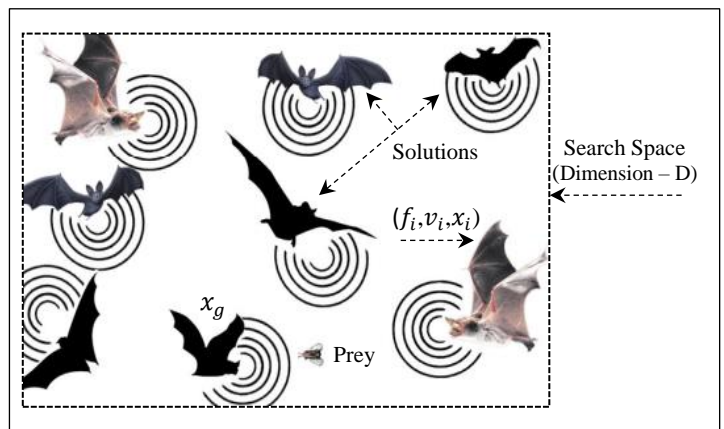


Figure 1: Flock of Bats in search of prey.

Source: Authors, (2022).

The BA, besides updating the positions of the bats (x_i), it controls the local and global searches, as in the other swarm

intelligence algorithms. The control is done, respectively, by varying the amplitude and the rate of pulse emission (r_i).

In the context of the STNEPp problem, the hunting environment represents the search space where the candidate solutions are; the dimension of the hunting environment represents the number of candidate branches; a flock of virtual bats represents the population; the number of bats in the flock represents the number of candidate solutions; a bat occupying a position represents a candidate solution, encoded as a vector; the quality of a bat represents its distance from the prey; the bat located near the prey represents a local optimal solution; and the bat located at the same position as the prey represents the global optimal solution.

To diversify the search in the dimension hunting environment, the BA updates the position, velocity, and frequency of each virtual bat i using equations (1) to (3), where: $\beta \in [0,1]$ is a vector of random numbers drawn from a uniform distribution; f_{min} and f_{max} are the minimum and maximum frequency bounds of the sound wave emitted by each virtual bat, respectively [22].

$$f_i = f_{min} + (f_{max} - f_{min}) \cdot \beta \quad (1)$$

$$v_i^{t+1} = v_i^t + (x_i^t - x_g^t) \cdot f_i \quad (2)$$

$$x_i^{t+1} = x_i^t + v_i^{t+1} \quad (3)$$

To intensify the search, the BA moves each virtual bat i in the direction occupied by the leader bat (x_g) in the hunting environment, using equation (4), where \bar{A}^t is the average loudness of all virtual bats and $\varepsilon \in [-1,1]$ is a vector of random numbers drawn from a uniform distribution.

$$x_{new}^{t+1} = x_g^t + \varepsilon \bar{A}^t \quad (4)$$

When one of the virtual bats i identifies a prey, depending on its distance to the prey, it increases its pulse emission rate (r_i) and decreases its amplitude (A_i). The amplitude (loudness) and the pulse emission rate of each virtual bat i are calculated, respectively, by the functions (5) and (6), where α and γ are constants.

$$A_i^{t+1} = \alpha A_i^t, \quad 0 < \alpha < 1 \quad (5)$$

$$r_i^{t+1} = r_i^0 [1 - \exp(-\gamma t)], \quad \gamma > 0 \quad (6)$$

These update functions indicate that when virtual bat i (candidate solution i in STNEPp) approaches a prey, i.e., when the objective of the problem (minimization of investment cost in STNEPp) is achieved, after a few iterations ($t \rightarrow \infty$), the amplitude of the pulse emitted by virtual bat i tends to zero ($A_i^t \rightarrow 0$) and the pulse emission rate tends to its initial value r_i^0 , i.e., ($r_i^t \rightarrow r_i^0 \in [0,1]$).

II.2 PSEUDOCODE OF THE ORIGINAL BA

The Algorithm 1 shows the pseudocode of the original BA [22]. The iterative cycle of the algorithm simulates the temporal evolution of the flock of bats. Before entering the iterative cycle (lines 5 to 21) the initial conditions of the algorithm are established.

Typical values suggested by [22] are: $f_{min} = 0$, $f_{max} = 2$, $\alpha = 0.97$, $\gamma = 0.10$, $A_i^0 = 1$, $r_i^0 = 1$ (line 1). The size of the flock of bat (Nm) and the maximum number of iterations (Nit) are also defined depending on the problem type.

Next (row 2) the first bat population ($X_{i,dim}^0$) is generated randomly (7), using random numbers ($\xi_{i,dim} \in [0,1]$) drawn from a uniform distribution. The dim parameter depends on the number of

variables in the problem. Lb and Ub are lower and upper bounds of the initial positions (x_i^0).

$$X_{i,dim}^0 = Lb + \xi_{i,dim} \cdot (Ub - Lb) \quad (7)$$

Then (row 3) the quality (fitness) of all initial bats (x_i^0) are evaluated according to the objective function of the optimization problem ($f(x_i^0)$) to enable their classification and the identification of the first leader bat (x_g^0) of the flock (row 4).

Next, the algorithm enters the iterative cycle (lines 5 to 21) that simulates the flights of the virtual bats, updating their current positions in the hunting environment to reach prey. The new positions (x_i^{t+1}) that the bats will occupy in the hunting environment are determined as a function of their current velocities (v_i^{t+1}), which are defined from their distances relative to the leader bat ($x_i^t - x_g^t$) and the frequencies of the emitted pulses (f_i) (lines 7 to 9).

Once the new bat positions are determined, the bats perform a local search around the position occupied by the current leader bat (x_g^t) to get closer to the prey (lines 10 and 12). This search is done by applying the random operator $\varepsilon \in [-1,1]$ on the average amplitude of the pulses emitted by all bats (\bar{A}^t) (line 11).

Confirmation of the approach is done through an acceptance test (lines 14 to 18) that depends on the sound amplitudes (A_i) and performance evaluations between the bat positioned as a function of velocity (x_i^{t+1}) and the one positioned as a function of pulse rate (\hat{x}_i^{t+1}). If the test is true, the bats occupy positions close to the leader bat and, consequently, occupy positions closer to the prey (line 15).

Algoritmo 1: Bat Algorithm (BA)

```

1: Initialize constants:  $Nit, Nm, f_{min}, f_{max}, \alpha, \gamma, A_i^0, r_i^0$ 
2: Initialize Bat flocks:  $x_i$  e  $v_i$ , ( $i = 1, 2, \dots, Nm$ )
3: Evaluates the quality of each bat in the flock:  $f(x_i^0)$ 
   {objective function}
4: Identify the first bat leader of the flock:  $x_g^0$ 
5: while stop condition do {maximum number of iterations –
    $Nit$  }
6:   for  $i=1$  to  $N$  do
7:      $f_i = f_{min} + (f_{max} - f_{min}) \cdot \beta$ ,  $\beta \in [0,1]$ 
8:      $v_i^{t+1} = v_i^t + (x_i^t - x_g^t) \cdot f_i$ 
9:      $x_i^{t+1} = x_i^t + v_i^{t+1}$ 
10:    if  $\xi_1 < r_i$ ,  $\xi_1 \in [0,1]$  then {perform local search}
11:       $\hat{x}_i^{t+1} = x_g^t + \varepsilon \bar{A}^t$ ,  $\varepsilon \in [-1,1]$ 
12:    end if
13:    Performs perturbation in one dimension of  $x_{new}^{t+1}$ 
14:    if  $\xi_2 < A_i$  or  $f(\hat{x}_i^{t+1}) \leq f(x_i^{t+1})$ ,  $\xi_2 \in [0,1]$  then
   {update position:  $x_i^{t+1}$ }
15:       $x_i^{t+1} = \hat{x}_i^{t+1}$ 
16:       $A_i^{t+1} = \alpha A_i^t$  {increase pulse amplitude}
17:       $r_i^{t+1} = r_i^0 [1 - \exp(-\gamma t)]$  {decrease the pulse
   emission rate}
18:    end if
19:    Identifies the current global leading bat:  $x_g^{t+1}$ 
20:  end for
21: end while
22: Displays best bat ( $x_g^*$ ) {global leader bat}

```

The pulse amplitudes (A_i^{t+1}) are increased and the pulse emission rates (r_i^{t+1}) are decreased (lines 16 and 17), respectively.

At this point in the algorithm, the positions of all virtual bats in the flock have been updated, and it is therefore necessary to identify the current leader bat (x_g^{t+1}) of the flock (line 19).

Then the iterative cycle continues until the set stopping criterion (line 5), i.e., the maximum number of iterations, is reached (line 20). Finally, the leading bat of the whole flock is presented.

II.3 MODIFIED BAT ALGORITHM

The BA is a technique capable of finding good results in a reasonable convergence time. However, it can converge prematurely [34], i.e., it converges to a local optimal solution instead of to the global optimal solution. Premature convergence occurs due to the decrease in search diversification in the solution space [35], which leads the algorithm to a stagnant state.

To reduce the problems that can be caused by premature convergence, this paper proposes to add a search intensification operator ($int(.)$), after line (20). This operator acts on the current position of the current leader bat (x_g^{t+1}), positioning the leader bat (x'_g) at a new position. The proposed operator $int(x_g^{t+1})$ randomly changes several elements (Ne) of the vector (x_g^t), according to the rule in equation (8).

$$x'_g = int(x_{g,Ne}^{t+1}) = \begin{cases} x_g^{t+1} - 1 \text{ se } \xi > 0.5 \\ x_g^{t+1} + 1 \text{ se } \xi < 0.5 \end{cases} \quad (8)$$

III. MATHEMATICAL MODEL OF STNEPp

This section presents the mathematical MINLP model used in BATp to represent the STNEPp problem, without deterministic security constraint (reliability criterion N-0), with the transmission network represented by an pFCC and active power losses included in the constraints.

III.1 CALCULATION OF LOSSES IN CIRCUITS

The calculation of the active power loss (p_{ij}) in each branch ij of the network is done as a function of the angular aperture of the terminal bar voltages (θ_{ij}) and their conductance (g_{ij}), as shown in the approximate nonlinear expression (9) [36], where (r_{ij}) is the resistance and (x_{ij}) is the reactance of branch ij .

$$p_{ij} \approx g_{ij}\theta_{ij}^2, \quad g_{ij} = r_{ij}/(r_{ij}^2 + x_{ij}^2) \quad (9)$$

III.2 MODELING THE OPTIMIZATION PROBLEM

In the mathematical model of STNEPp, the active losses in the circuits are treated as virtual loads and equally distributed among the respective terminal bars. With the losses added to the terminal bars of the configuration, new values of angles, power flows in the circuits and generated power at the reference bar are obtained. In the model it was considered that the reference bus supplies the system losses, that is, it balances the active power of the current configuration.

Therefore, to consider the effect of active circuit losses, in the mathematical model of the STNEPp problem, a term was added in the equality constraint of the model presented in [37]. With this adjustment, the modified model takes the form presented in (10) to (16), where neither the circuits added to the existing transmission network nor the angles of the bars are initially known.

$$\begin{aligned} \text{Min } v &= \sum_{(ij) \in \Omega_C} c_{ij}n_{ij} + \alpha \sum_{i \in B} cc_i \\ \text{Subject to:} & \end{aligned} \quad (10)$$

$$g_i - \sum_{j \in \Omega_i} f_{ij} + cc_i = d_i + (\sum_{j \in \Omega_i} p_{ij})/2, \forall i \in \Omega_B \quad (11)$$

$$f_{ij} = \gamma_{ij}(n_{ij}^0 + n_{ij}) \cdot \theta_{ij}, \forall ij \in \Omega_L \quad (12)$$

$$|f_{ij} + p_{ij}/2| \leq (n_{ij}^0 + n_{ij})\bar{f}_{ij}, \forall ij \in \Omega_L \quad (13)$$

$$0 \leq g_i \leq \bar{g}_i, \forall i \in \Omega_B \quad (14)$$

$$0 \leq cc_i \leq d_i, \forall i \in \Omega_B \quad (15)$$

$$0 \leq n_{ij} \leq \bar{n}_{ij}, n_{ij} \in \mathbb{Z}, \forall ij \in \Omega_L \quad (16)$$

Where: Ω_C – set of all candidate circuits; B – set of all load shedding bars; Ω_i – set of circuits connected to bus i ; Ω_B – set of all buses (existing and candidate); Ω_L – set of all circuits (existing and candidate); v – total cost of each candidate solution; c_{ij} – cost of circuits added to branch ij ; n_{ij} – number of circuits added on branch ij ; α – penalty factor (\$/MW); cc_i – active load shedding at bus i ; g_i – generation of bus i ; d_i – active load of bus i ; f_{ij} – active power flow on branch ij ; p_{ij} – active power loss on circuit ij ; γ_{ij} – susceptance of circuit ij ; n_{ij}^0 – number of existing circuits on branch ij ; n_{ij} – number of circuits added on branch ij ; θ_{ij} – opening of the angles of the voltages of buses i and j ; \bar{f}_{ij} – maximum active power flow that can circulate in circuit ij ; \bar{g}_i – maximum generation that can be produced in bus i ; \bar{n}_{ij} – maximum number of circuits that can be added in branch ij .

Equation (10) represents the objective function of the problem that minimizes the total cost of circuits (lines and transformers) added to the existing transmission network, with the total cost of load shedding the solutions that have circuit loading limit violations. The second term is intended to enable solving problem (10) to (16) by the modified BA module of the BATp optimizer.

The constraint (11) models the active power balance (Kirchhoff's 1st law) of each bus. Constraint (12) models the active power flow through each branch, considering the active power loss. The channelization constraint (13) sets the limit on the active power flow that can flow through each branch.

Channeling constraints (14) to (16) set the limits on generation and load shedding at each bus and the number of new circuits that can be added to each branch.

The set of circuits for each feasible candidate solution is defined by a specific module of the BATp optimizer responsible for formulating candidate solutions. If the generated candidate solution is infeasible, i.e., has load shedding, another module of the optimizer acts to make it economically competitive

IV. STRUCTURE OF BATp OPTIMIZER

This section presents the proposed algorithm, called the BATp optimizer, for solving the STNEPp problem, whose structure and operation is similar to that used in [5].

IV.1 BATp ALGORITHM FLOWCHART

The BATp proposed to solve the STNEPp problem uses the structure composed of the eight stages described in Figure 2.

In each iteration of the BATp, the solutions proposed by the modified BA go through the sieve of feasibility (stage 4) and competitiveness (stage 5) procedures.

➤ STAGE 1

In this stage, the data required by the BATp optimizer is defined, that is, the data that the original BA uses and the data of the system to be planned. The data for the BA are the same as presented above.

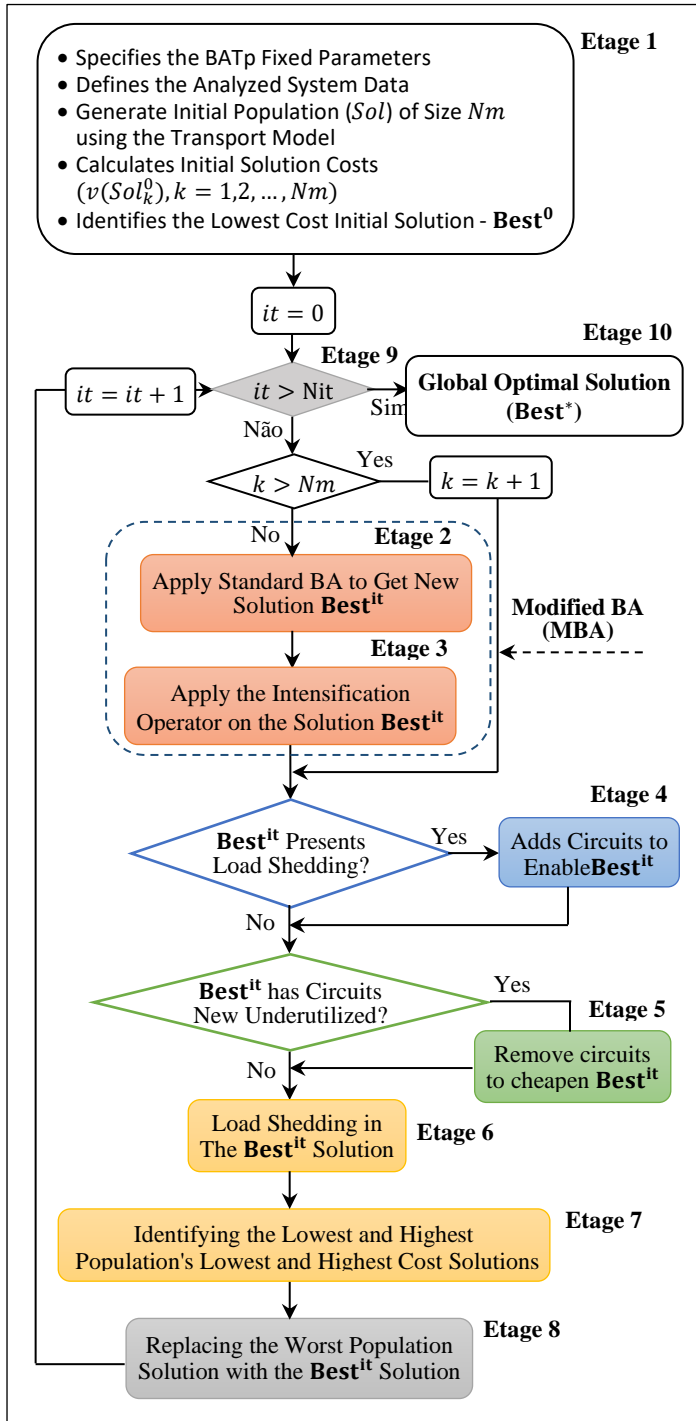


Figure 2: Simplified BATp optimizer flowchart.
Source: Authors, (2022).

The data related to the system are: existing transmission network topology; existing and future bar data (g_i, \bar{g}_i, d_i) ; existing and candidate circuit data $(n_{ij}^0, n_{ij}, \gamma_{ij}, c_{ij}, \bar{f}_{ij})$. The maximum number of circuits that can be added in each branch ($Ncir$) is also defined in this stage.

In this step, the first set of solutions to the problem is also defined, i.e., an initial population (Sol^0) composed of (Nm) bats (candidate solutions). Each candidate solution of the initial population ($Sol_k^0, k = 1, 2, \dots, Nm$), has dimension equal to the number of branches (NR) of the analyzed system and each element of the vector corresponds to a candidate branch to add one or more circuits (n_{ij}). The value of each element of Sol_k^0 , can assume a value between zero and $Ncir$.

The Figure 3 shows an example of a solution Sol_k^0 of a hypothetical system consisting of eight branches ($NR = 8$) and that $Ncir = 4$. In this solution, branches 1-2, 1-4, 1-5, 2-3, 2-4 have one circuit, branch 3-5, 4-6 have two circuits, and branch 2-6 have four circuits.

Ramos	#1-2	#1-4	#1-5	#2-3	#2-4	#3-5	#6-4	#6-2
n_{ij}	1	1	1	1	1	2	2	4

Figure 3: Representation of a candidate solution.
Source: Authors, (2022).

In the specialized literature, there is no rule that defines what should be the number of individuals in the population (Nm) and the number of iteration (Nit). In BATp, these values are defined as a function of the number of branches (NR) of the transmission network analyzed, as shown in equations (17) and (18). Note that NR is equivalent to the size (D) of the bats' hunting environment.

$$Nm \geq NR \quad (17)$$

$$Nit \geq 10 \cdot Nm \quad (18)$$

The way of defining the components of the initial solutions affects the qualities of the candidate solutions of the initial population and the number of iterations required for convergence, since the characteristics of the initial solutions are transferred to the descendant solutions throughout the iterations of the algorithm [38].

Therefore, generating a good initial population and using an appropriate population size tends to improve the performance of the algorithm [39]. In general, if the initial population is generated randomly, the computational effort tends to be high [5].

In the original BA, the initial population (Sol^0) is generated randomly (7), i.e., it does not consider the topology of the existing transmission network, the data of bars (g_i, \bar{g}_i, d_i) and circuits $(n_{ij}^0, n_{ij}, \bar{f}_{ij})$. This way of generating the initial population can delay the achievement of the global optimal solution, especially if the system to be planned is large.

In BATp, the initial population (Sol^0) is composed of (Nm) candidate solutions $(\{Sol_1^0, \dots, Sol_k^0, \dots, Sol_{Nm}^0\})$ being generated according to the system topology and its bus and circuit data. It is obtained in two steps:

Step 1: Solve the transport model, represented by the integer linear programming (ILP) problem (19) to (23) [37], [40], using the *linprog* function of MatLab, to obtain the first solution (Sol_1^0) of the initial population.

$$\text{Min } v(Sol_1^0) = \sum_{(i,j) \in \Omega_C} c_{ij} n_{ij} \quad (19)$$

Subject to:

$$g_i - \sum_{j \in \Omega_i} f_{ij} = d_i, \forall i \in \Omega_B \quad (20)$$

$$|f_{ij}| \leq (n_{ij}^0 + n_{ij}) \bar{f}_{ij}, \forall ij \in \Omega_L \quad (21)$$

$$0 \leq g_i \leq \bar{g}_i, \forall i \in \Omega_B \quad (22)$$

$$0 \leq n_{ij} \leq \bar{n}_{ij}, n_{ij} \in \mathbb{Z}, \forall ij \in \Omega_L \quad (23)$$

Step 2: Generate the other $(Nm - 1)$ initial candidate solutions $(\{Sol_2^0, \dots, Sol_k^0, \dots, Sol_{Nm}^0\})$ by randomly changing the positions and circuit numbers of the branches of the solution Sol_1^0 , until the population size (Nm) is reached.

This way of generation produces some infeasible solutions (solutions with load shedding), due to the simplified model (19) to (23), which considers only Kirchhoff's first law. However, these

solutions are systematically eliminated over the iterations (step 4) of the BATp optimizer.

Once the parameters (n_{ij}) and (c_{ij}) of each solution (Sol_k^0) of the initial population are known, the costs ($v(Sol_k^0)$) are determined by summation ($\sum c_{ij}n_{ij}$) and the solution of lowest overall cost ($v(Best_k^0) = \min(\sum c_{ij}n_{ij})$) is identified.

In this step, the load shedding $cc(Sol_{inf}^0)$ of the infeasible solutions (Sol_{inf}^0), i.e., those with violations of the maximum circuit capacities, are also calculated. The values of the load shedding are obtained by solving the linear programming (LP) problem (24) to (29), using the *linprog* function of MatLab.

$$\text{Min } cc(sol_{inf}^0) = \sum_{i \in \Omega_B} cc_i \quad (24)$$

Subject to:

$$g_i - \sum_{j \in \Omega_i} f_{ij} + cc_i = d_i, \forall i \in \Omega_B \quad (25)$$

$$f_{ij} = \gamma_{ij}(n_{ij}^0 + n_{ij})(\theta_i - \theta_j) = 0, \forall ij \in \Omega_L \quad (26)$$

$$|f_{ij}| \leq (n_{ij}^0 + n_{ij})\bar{f}_{ij}, \forall ij \in \Omega_L \quad (27)$$

$$0 \leq g_i \leq \bar{g}_i, \forall i \in \Omega_B \quad (28)$$

$$0 \leq r_i \leq d_i, \forall i \in \Omega_B \quad (29)$$

➤ STAGE 2

After the completion of step 1, BATp effectively sets out to search for the local optimal solutions ($Best^{it}$) of each iteration ($it = 1, 2, \dots, Nit$) and the global optimal solution ($Best^*$). To this end, it performs, at each iteration, the sequence of calculations and tests described in equations (30) to (44), which perform the steps of the modified BA (MBA). The round operator “*round*” and the absolute value operator “*abs*” were used because the number of circuits that must be added in each branch of the transmission network must always be integer and positive.

$$f_k^{it} = f_{min} + (f_{max} - f_{min}) \cdot \beta, \beta \in [0,1] \quad (30)$$

$$v_k^{it+1} = v_k^{it} + \text{abs}((sol_k^{it} - Best^{it}) \cdot f_k^{it}) \quad (31)$$

$$sol_k^{it+1} = sol_k^{it} + \text{round}(v_k^{it+1}) \quad (32)$$

$$\text{if } \xi_1 < r_k, \xi_1 \in [0,1] \quad (33)$$

$$\widehat{sol}_k^{it+1} = Best^{it} + \varepsilon \bar{A}^{it}, \varepsilon \in [-1,1] \quad (34)$$

$$\text{end if} \quad (35)$$

$$\text{if } \xi_2 < A_k^{it} \text{ or } f(\widehat{sol}_k^{it+1}) \leq f(sol_k^{it+1}), \xi_2 \in [0,1] \quad (36)$$

$$sol_k^{it+1} = \widehat{sol}_k^{it+1} \quad (37)$$

$$A_k^{it+1} = \alpha A_k^{it} \quad (38)$$

$$r_k^{it+1} = r_k^0 [1 - \exp(-\gamma t)] \quad (39)$$

$$\text{end if} \quad (40)$$

$$\text{if } f(\widehat{sol}_k^{it+1}) \leq f(Best^{it}) \quad (41)$$

$$Best^{it} = \widehat{sol}_k^{it+1} \quad (42)$$

$$f(Best^{it}) = f(\widehat{sol}_k^{it+1}) \quad (43)$$

$$\text{end if} \quad (44)$$

➤ STAGE 3

This stage has the purpose of applying a local search intensification operator ($int(\cdot)$) on the current global optimal solution ($Best^{it}$), obtained in step 2, to obtain a new solution $Best_{new}^{it}$ that subsequently passes the sieves of the infeasibility (stage 5) and competitiveness (stage 6) improvement procedures.

The operator $int(\cdot)$ changes the number of circuits of (Ne) branches of the solution $Best^{it}$ current by increasing or decreasing, by one unit, the number of circuits of the randomly selected branches (45). Where ξ_3 is an integer random number between $[1, NR]$ and ξ_4 is a random number between $[0,1]$.

$$Best_{new}^{it}(\xi_3) = \begin{cases} \text{int}(\xi_3) = Best^{it}(\xi_3) - 1 \text{ se } \xi_4 > 0.5 \\ \text{int}(\xi_3) = Best^{it}(\xi_3) + 1 \text{ se } \xi_4 < 0.5 \end{cases} \quad (45)$$

The parameter (Ne) is defined as a function of the size of the analyzed system, that is, it is defined as a function of the number of branches (NR) and the number of bars (NB), through equation (46). The floor function rounds the result of the division (NR/NB) towards negative infinity, and the ceil function rounds it towards positive infinity.

$$Ne = \begin{cases} \text{ceil}(NR/NB) & \text{se } NR/NB \geq 2,5 \\ \text{floor}(2NR/NB + 1) & \text{caso contrário} \end{cases} \quad (46)$$

➤ STAGE 4

This stage is intended to make the current $Best_{new}^{it}$ solution, modified in step 3, viable, in case it exhibits load shedding, to compete with the other solutions in the current population. The elimination of load shedding is done by adding in $Best_{new}^{it}$ a set of new circuits $\{n_{ij}^{VGS}\}$, which are obtained based on the sensitivity index (IS_{ij}) (47) that was used in the Villasana-Garver-Salon (VGS) constructive heuristic algorithm (CHA) [41], [42].

$$IS_{ij} = \max \{ n_{ij}^{VGS} \bar{f}_{ij} \}, n_{ij}^{VGS} \neq 0 \quad (47)$$

The solution resulting from joining the solution $Best_{new}^{it}$ with the set of circuits $\{n_{ij}^{VGS}\}$, called the solution $Best_{VGS}^{it}$, is submitted to the feasibility procedure, performed in stage 5, and the competitiveness procedure, performed in stage 6.

Obtaining the circuit set $\{n_{ij}^{VGS}\}$ is done by solving the LP problem (48) to (54), during the execution of the CHA steps of VGS [43].

$$\text{Min } v(n_{ij}^{VGS}) = \sum_{(i,j) \in \Omega_C} c_{ij} n_{ij}^{VGS} \quad (48)$$

Subject to:

$$g_i - \sum_{j \in \Omega_i} f_{ij}^{Best} - \sum_{j \in \Omega_i} f_{ij}^{VGS} = d_i, \forall i \in \Omega_B \quad (49)$$

$$f_{ij}^{Best} = \gamma_{ij} n_{ij}^{Best} (\theta_i - \theta_j), \forall ij \in \Omega_C \quad (50)$$

$$|f_{ij}^{Best}| \leq n_{ij}^{Best} \bar{f}_{ij}, \forall ij \in \Omega_C \quad (51)$$

$$|f_{ij}^{VGS}| \leq n_{ij}^{VGS} \bar{f}_{ij}, \forall ij \in \Omega_C \quad (52)$$

$$0 \leq g_i \leq \bar{g}_i, \forall i \in \Omega_B \quad (53)$$

$$0 \leq n_{ij}^{VGS} \leq \bar{n}_{ij}, \forall ij \in \Omega_C \quad (54)$$

The execution of the CHA steps ends when the solution coming from solving the results in $\{n_{ij}^{VGS} = 0\}$ and $v(n_{ij}^{VGS}) = 0$, which means that it is no longer necessary to add circuits to eliminate load shedding. That is, the system operates properly without overloads, with the circuits from the solution $Best_{new}^{it}$ and the $\{n_{ij}^{VGS}\}$ circuits from solving LP.

In this LP problem, the power flows in the branches are separated as follows: f_{ij}^{Best} – flow in the branch ij of the solution $Best_{new}^{it}$ current and f_{ij}^{VGS} – flow in the added circuit in branch ij during the execution of the CHA; n_{ij}^{Best} – number of circuits existing in branch ij of the solution $Best_{new}^{it}$ current; n_{ij}^{VGS} – number of circuits added in branch ij during the iterative process of the CHA; Ω_C – set of all candidate circuits.

➤ STAGE 5

In stage 4, some circuits added to the current solution $Best_{VGS}^{it}$ by the approximate CHA model may be unnecessary and should be removed to make this solution competitive, in terms of

investment cost. Thus, this stage is intended to eliminate the redundant circuits present in the current solution $Best_{VGS}^{it}$.

Elimination of redundant circuits is done as follows: first, all the circuits in the current solution $Best_{VGS}^{it}$ are placed in descending order of investment cost, and then each circuit is removed. If the removal of the circuits from the current solution $Best_{VGS}^{it}$ does not cause load shedding, it means that it is unnecessary being eliminated from the solution. Thus, only those circuits that if removed do not cause load shedding will be part of the current solution $Best_{VGS}^{it}$.

➤ **STAGE 6**

In this step, the cost of the current solution $Best_{VGS}^{it}$ ($v(Best_{VGS}^{it})$) and the load shedding ($c(Best_{VGS}^{it})$) are obtained if the current solution $Best_{VGS}^{it}$ has overloads. The investment cost is obtained by the product ($\sum c_{ij}n_{ij}^{VGS}$), given that the number of circuits added (n_{ij}^{VGS}) and their individual costs (c_{ij}) are known.

The amount of load shedding is obtained by the MatLab function *linprog*, which solves a LP problem similar to problem (24) to (29). The load shedding ($c(Best_{VGS}^{it})$) is used in the test for including the solution $Best_{VGS}^{it}$ in the current population, performed in stage 8, to replace the most expensive solution in the population.

➤ **STAGE 7**

This step aims to identify, among the solutions of the current population ($\{Sol_1^{it}, \dots, Sol_k^{it}, \dots, Sol_{Nm}^{it}\}$), the least cost ($v(Sol_{min}^{it})$) and highest cost ($v(Sol_{max}^{it})$) solutions, and the highest load shedding ($c(Sol_{max}^{it})$). These vectors are used in stage 8.

➤ **STAGE 8**

This step is intended to verify whether the current solution $Best_{VGS}^{it}$ can enter the current population in replacement of the one with the worst quality in terms of cost and load shedding.

Two conditions are imposed for the current solution $Best_{VGS}^{it}$ to be accepted into the current population: i) the current solution $Best_{VGS}^{it}$ must differ from all other solutions, i.e., it must present a circuit configuration that does not exist in the current population; ii) the current solution $Best_{VGS}^{it}$ must have a lower cost (if it is feasible) or lower load shedding (if it is infeasible) than all other solutions in the current population. Three situations are tested in the BATp optimizer:

- 1) the current solution $Best_{VGS}^{it}$ has load shedding ($c(Best_{VGS}^{it}) \neq 0$) and there is one or more solutions in the current population with load shedding, then $Best_{VGS}^{it}$ replaces the solution with the largest load shedding ($c(Sol_{max}^{it})$);
- 2) the solution $Best_{VGS}^{it}$ has no load shedding ($c(Best_{VGS}^{it}) = 0$) and there is one or more solutions in the current population with load shedding, then $Best_{VGS}^{it}$ replaces the solution with the highest load shedding ($c(Sol_{max}^{it})$);
- 3) the solution $Best_{VGS}^{it}$ has no load shedding ($c(Best_{VGS}^{it}) = 0$) and there are no solutions in the current population with load shedding, so $Best_{VGS}^{it}$ replaces the solution in the current population with the highest cost ($v(Sol_{max}^{it})$).

➤ **STAGE 9**

In this stage, the BATp optimizer checks whether the stopping criterion is met, i.e., if the current number of iterations (*it*) is greater than the specified maximum value (*Nit*). If it is greater, then the iterative process is terminated and stage 10 is executed. Otherwise, the algorithm increments the iteration counter and returns to stage 2.

➤ **STAGE 10**

In this step, the BATp optimizer presents the global optimal solution ($Best^*$) found in the iteration (*Nit*), in terms of investment cost and number of circuits added in each branch of the base transmission network.

V. CASE STUDIES AND ANALYSIS OF RESULTS

This section presents the results obtained with the BATp optimizer on three systems well known in the specialized literature: IEEE-24/41 and SB-46/79. The mathematical model of the BATp optimizer was implemented in MatLab R2008a language and the simulations were performed on a computer with Intel® Core™ i5 processor, 2.40 GHz CPU, 8 GB RAM. Some routines used in [5] were adapted to the computational model of the BATp optimizer. The (17) and (18) rules were used to define the number of simulations (*Nm*) and the number of iterations (*Nit*).

V.1. IEEE TEST SYSTEM (IEEE-24/41)

This test system was proposed by [44] to perform reliability analysis that, after modifications in generation and load data, was also used for STNEP studies [5], [45], [46], [9], [12], among others. Because it is known by the international community, it is a good option for testing new optimization techniques.

The Figure 4 shows the topology of this test system indicating the 34 existing circuits (solid lines), the 7 new candidate circuits (#1-8, #2-8, #6-7, #13-14, #14-23, #16-23, #19-23 in dotted lines) and the 17 load buses and 10 generation buses. The total load and generation of this system is 8.5550 MW, the number of buses is $NB = 24$, the number of candidate branches is $NR = 41$ and ($NR/NB = 1.708$). There are no isolated buses in this system. All the electrical data and costs of this system are given in [47], [48].

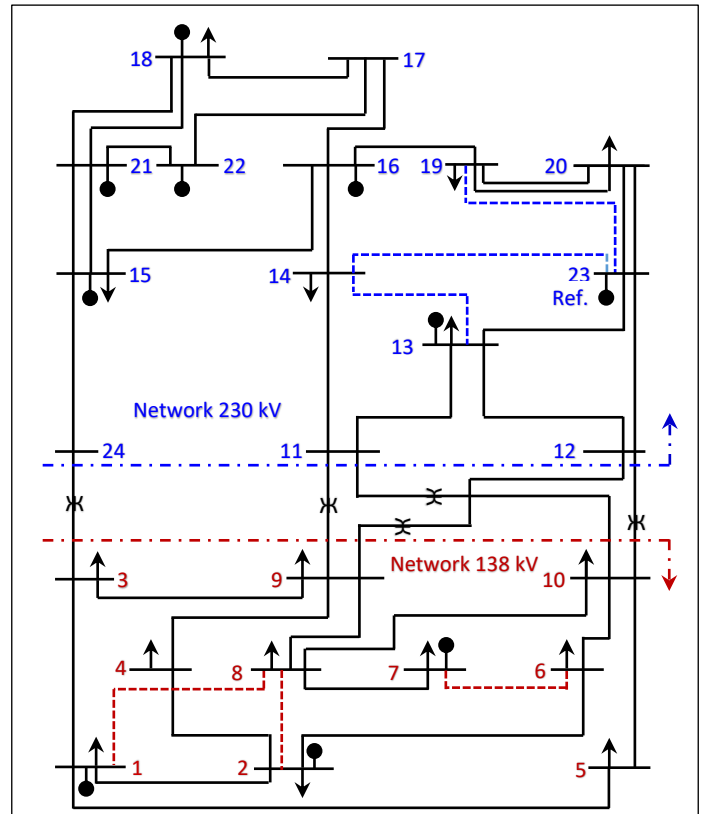


Figure 4: IEEE-24/41 test system topology. Source: Authors, (2022).

With this test system, two cases were simulated, where one allows generation redispatch and the other does not allow redispatch. The bus #3 was used to close the power balance.

The maximum number of circuit additions per branch allowed was three ($N_{cir} = 3$). With this assumption, the total number of circuits that can be added in the system branches is $3 \times 41 = 123$.

The number of possible combinations of additions is on the order of $441 \approx 4.84 \times 10^{24}$.

In the simulations for the two cases, the following data were used in the BATp: $N_e = \text{round}(2 \times 24 / 41) = 3$, $N_m > N_R = 50$ and $N_{it} = 10$. $N_m = 500$.

V.1.1 Lossless Optimal Solutions

According to [5], [12], [49] and several other authors, the optimal solution for this system, without considering the effect of active power losses but allowing generation redispatch (G0 generation scenario in [47]), is composed of five circuits connected in four branches (#6-10=1, #7-8=2, #10-12=1, #14-16=1) and costs US\$ 152 million.

Without considering losses, and not allowing generation redispatch (generation scenario G1 [47]), according to [50], [51] and other authors, the optimal solution is composed of fifteen circuits connected on nine branches (#1-5=1, #3-24=1, #6-10=1, #7-8=2, #14-16=1, #15-24=1, #16-17=2, #16-19=1, #17-18=2) and costs US\$ 390 million. The BATp optimizer, with $r_{ij} = 0$, has also found this solution.

V.1.2 Case With Generation Redispatch (WR)

The characteristics of the optimal solution obtained by the BATp optimizer, with less than 50 iterations (Figure 5), are as follows:

- Cost and number of circuits (#i-j) of the optimal solution: US\$ 182 million and #6-10=1, #7-8=2, #10-12=1, #14-16=1, #20-23=1 (Figure 6);
- Loading levels on the reinforced branches (Figure 7): branch #6-10 (87.63% of its capacity), #7-8 (98.72%), #10-12 (78.56%), #14-16 (74.47%), #20-23 (73.39%);
- Active power losses in the reinforced branches (Figure 7): 48.86 MW (22.82% of system loss). In the system, the active power loss is 214.09 MW (2.50% of the load).

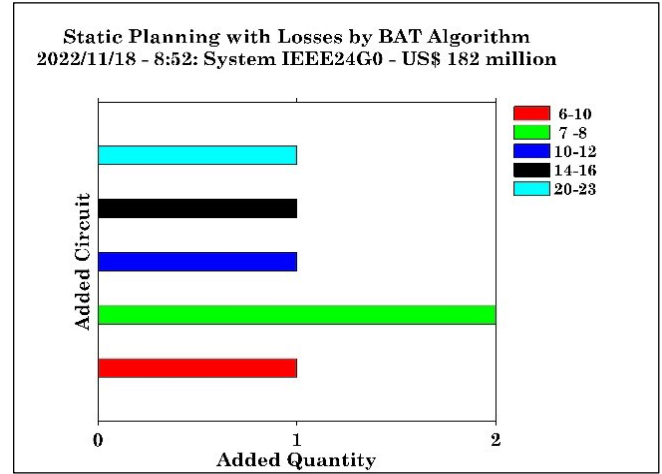


Figure 6: Case WR - IEEE-24/41 test system. Planned circuits. Source: BATp optimizer, (2022).

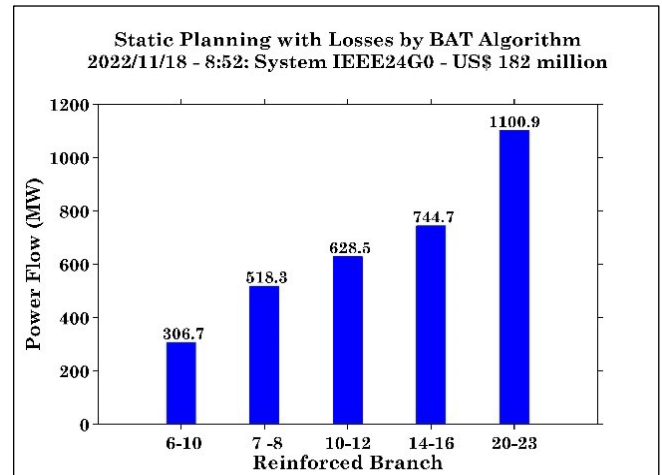


Figure 7: Case WR - IEEE-24/41 test system. Flows in the branches. Source: BATp optimizer, (2022).

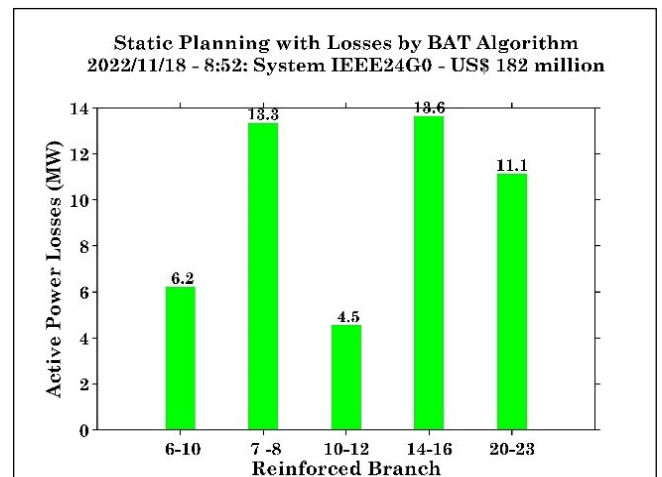


Figure 8: Case WR - IEEE-24/41 test system. Losses in the branches. Source: BATp optimizer, (2022).

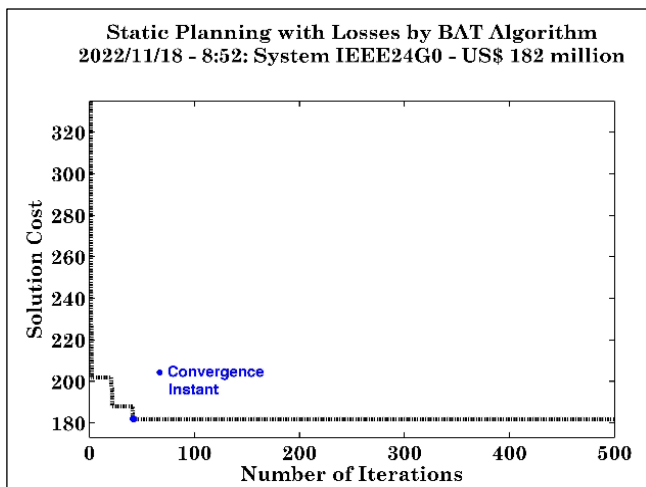


Figure 5: Case WR - IEEE-24/41 test system. Cost convergence curve. Source: BATp optimizer, (2022).

V.1.3 Case Without Generation Redispatch (WOR)

The characteristics of the optimal solution obtained by the BATp optimizer, with less than 100 iterations (Figure 9), are as follows:

- Cost and number of circuits on the branches of the optimal solution: US\$ 370 million and #6-10=1, #7-8=2, #10-12=1, #14-16=1, #20-23=1 (Figure 10);

- Loading levels on the reinforced branches (Figure 11): #1-5 (77.13% of their capacity), #3-24 (77.34%), #6-10 (81.40%), #7-8 (98.72%), #14-16 (82.00%), #15-24 (62.75%), #16-17 (82.18%); #16-19 (59.28%), #17-18 (82.99 %);
- Active power losses in the reinforced branches (Figure 12): 87.79 MW (37.26% of system loss). In the system, the active power loss is 235, 60MW (2.76% of the load).

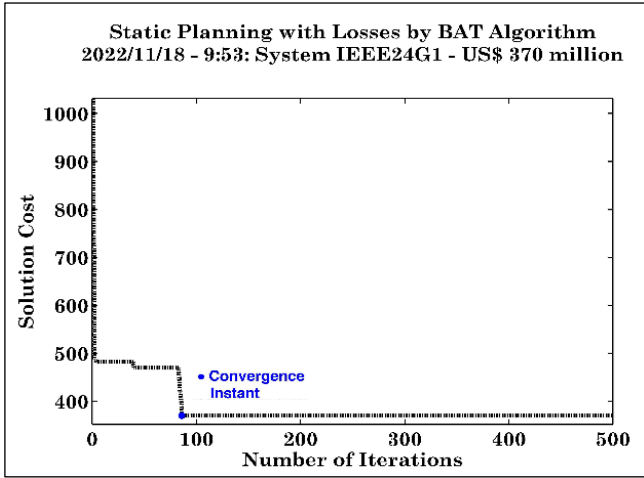


Figure 9: Case WOR - IEEE-24/41 test system. Cost convergence curve. Source: BATp optimizer, (2022).

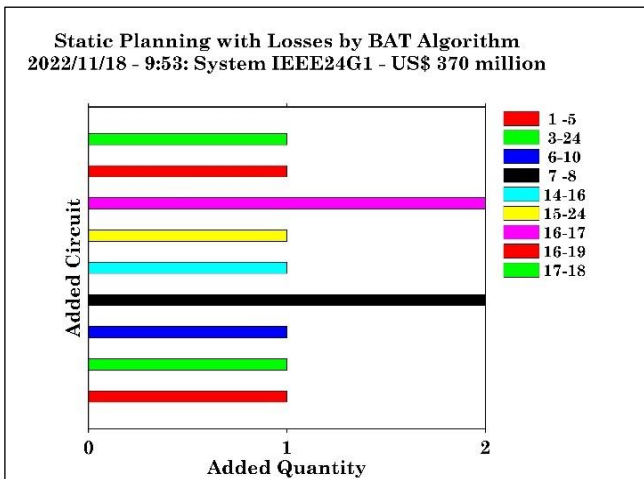


Figure 10: Case WOR - IEEE-24/41 test system. Planned circuits. Source: BATp optimizer, (2022).

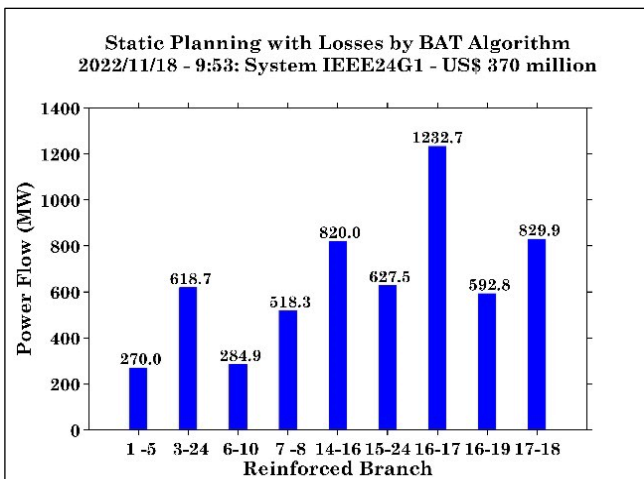


Figure 11: Case WOR - IEEE-24/41 test system. Flows in the branches. Source: BATp optimizer, (2022).

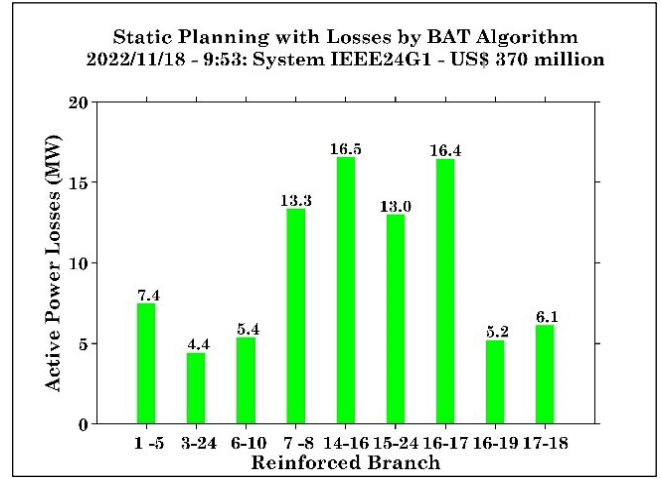


Figure 12: Case WOR - IEEE-24/41 test system. Losses in the branches. Source: BATp optimizer, (2022).

V.1.4 Summary of Results

The Table 4 shows the summary of the results, illustrated in Figures 21 and 24, where lower amounts of circuits added on the network branches, lower investment cost (US\$ million) and lower active power loss (MW) are observed when considering generation redispatch.

Table 4: IEEE-24/41 test system - Comparison of the cases.

Case	Number Circuits	Added Circuits	Cost	Loss
WR	6	#6-10=1, #7-8=2, #10-12=1, #14-16=1, #20-23=1	182 (49.19%)	49.37 (56.24%)
WOR	11	#1-5=1, #3-24=1, #6-10=1, #7-8=2, #14-16=1, #15-24=1, #16-17=2, #16-19=1, #17-18=1	370 (100%)	42.07 (100%)

Source: Authors, (2022).

V.1.5 Solutions Obtained by Other Authors

The Table 5 shows the solutions obtained by other authors, when considering active power losses and allowing generation redispatch (WR). In the articles, it is not explicit which power balance bus was used.

Table 5: IEEE-24/41 test system - Other authors' solutions.

Solution Costs (million) and Circuits	Author
US\$ 182: #6-10=1, #7-8=2, #10-12=1, #14-16=1, #20-23=1	[12]
US\$ 188: #6-10=1, #7-8=2, #10-12=1, #14-16=1, #16-17=1	[9]

Source: Authors, (2022).

V.2 SOUTH BRAZILIAN TEST SYSTEM (SB-46/79)

This system was first used in [52] to test an iterative method, and since then, it has been widely used to evaluate exact and approximate algorithms. This system, whose topology is shown in Figure 13, is widely used in several works about TNEP.

The total demand of this system is 6880 MW, it has 46 buses ($NB = 46$), 79 candidate branches ($NR = 79$), being 47 existing and 32 new. It has eleven isolated buses on the 230 kV and 500 kV networks (#3, #6, #10, #11, #15, #25, #28, #29, #30, #31, #41) and

virtually the same NR/NB ratio = 1.717 as the IEEE-24/41 test system.

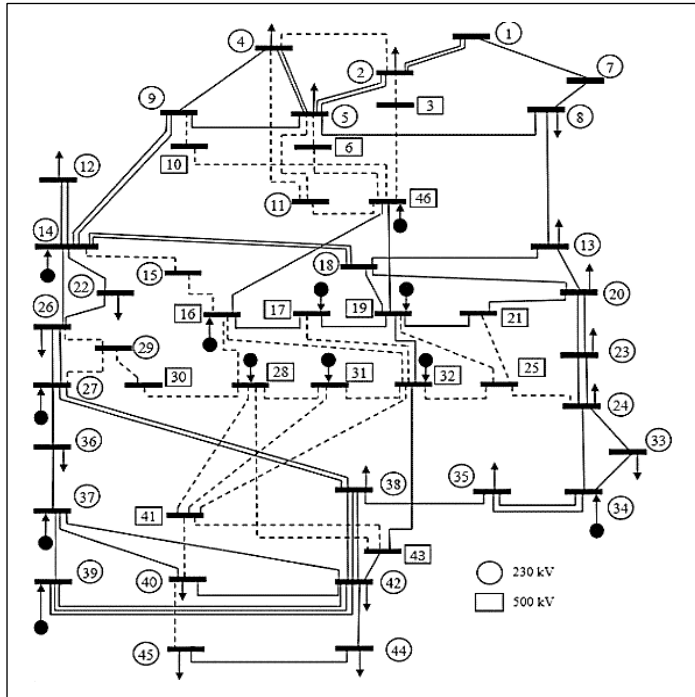


Figure 13: SB-46/79 test system topology. Source: Authors, (2022) - Adapted from [40].

The bus and circuit data (electrical parameters and costs) are described in [40]. The resistor values for all circuits are 10% of the reactance values.

With this system, two cases were simulated, where one allows generation redispatch and the other does not allow redispatch. The bus #16 was used to close the power balance.

The maximum allowed number of circuit additions per branch is three ($N_{cir}=3$). With this assumption, the total number of circuits that can be added in the system branches is $3 \times 79=237$.

The number of possible combinations of additions is on the order of $479 \approx 3.65 \times 10^{47}$, i.e., 1.18×10^{23} times larger than the possibilities of additions that can be made in the IEEE-24/41 test system, requiring BATp to run a larger number of simulations to reduce the risk of premature convergence to a suboptimal solution.

In the simulations for the two cases, the following data were used in BATp: $N_e = \text{round}(2 \times 79 / 46)$, $N_m > NR = 80$ and $N_{it} = 10 \cdot N_m = 800$.

V.2.1 Lossless Optimal Solutions

According to [5], [48] and several other authors, the optimal solution for this system, without considering the effect of active power losses but allowing generation redispatch is composed of nine circuits connected in seven branches (#2-5=1, #5-6=2, #13-20=1, #20-21=2, #20-23=1, #42-43=1, #46-6=1) and costs US\$72.870 million. The BATp optimizer, with $r_{ij}=0$, also found the same solution.

Without considering power losses, but not allowing generation redispatch, according to [53], [54] and several other authors, the optimal solution is composed of fifteen circuits connected in nine branches #20-21=1, #42-43=2, #46-6=1, #19-25=1, #31-32=1, #28-30=1, #26-29=3, #24-25=2, #29-30=2, #5-6=2) and costs US\$154.420 million.

V.2.2 Case With Generation Redispatch (WR)

The characteristics of the optimal solution obtained by the BATp optimizer with less than 50 iterations (Figure 14) are as follows:

- Cost and number of circuits on the branches of the optimal solution: \$75.895 million and #18-20=1, #20-23=1, #20-21=2, #42-43=1, #46-6=1, #5-6=2 (Figure 15);
- Loading levels on the reinforced branches (Figure 16): #18-20 (100.00% of its capacity), #20-23 (94.53%), #20-21 (78.00%), #42-43 (100.0%), #46-6 (51.67%), #5-6 (85.27%);
- Active power losses in the reinforced branches (Figure 17): 70.90 MW (19.83% of system loss). In the system, the active power loss is 357.56MW (5.20% of the load).

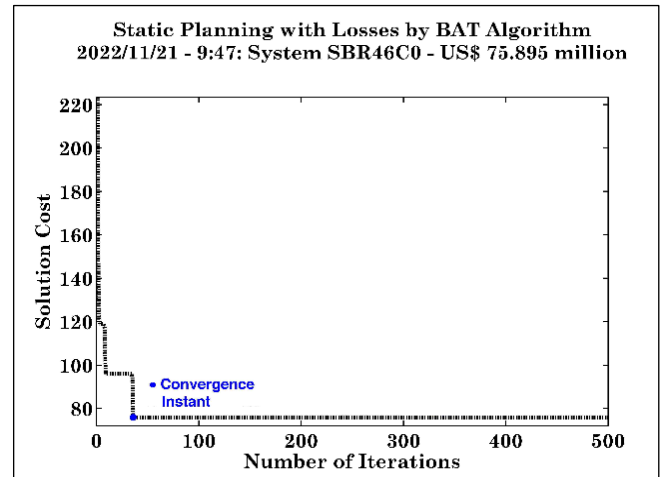


Figure 14: Case WR - SB-46/79 test system. Cost convergence curve. Source: BATp optimizer, (2022).

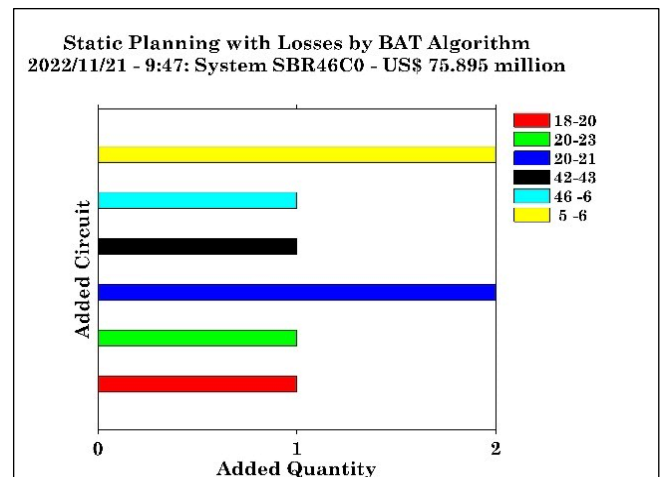


Figure 15: Case WR - SB-46/79 test system. Planned circuits. Source: BATp optimizer, (2022).

V.2.3 Case Without Redispatch (WOR)

The characteristics of the optimal solution obtained by the BATp optimizer with less than 150 iterations (Figure 18) are as follows:

- Cost and number of circuits on the branches of the optimal solution: US\$164.752 million and #20-21=2, #42-43=2, #46-6=1, #19-25=1, #31-32=1, #28-43=1, #24-25=2, #5-6=1 (Figure 19);
- Loading levels on the reinforced branches (Figure 20): #20-21 (92.05% of its capacity), #42-43 (99.94%), #46-6 (53.06%),

#19-25 (69.94%), #31-32 (15.49%), #28-43 (59.96%), #24-25 (80.06%), #5-6 (87.55%);

- Active power losses in the reinforced branches (Figure 21): 99.81 MW (35.18% of system loss). In the system, the active power loss is 283.68MW (3.83% of the load).

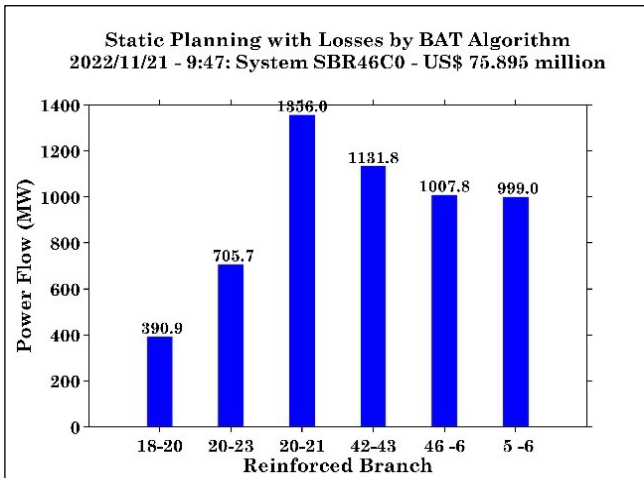


Figure 16: Case WR - SB-46/79 test system. Flows in the branches. Source: BATp optimizer, (2022).

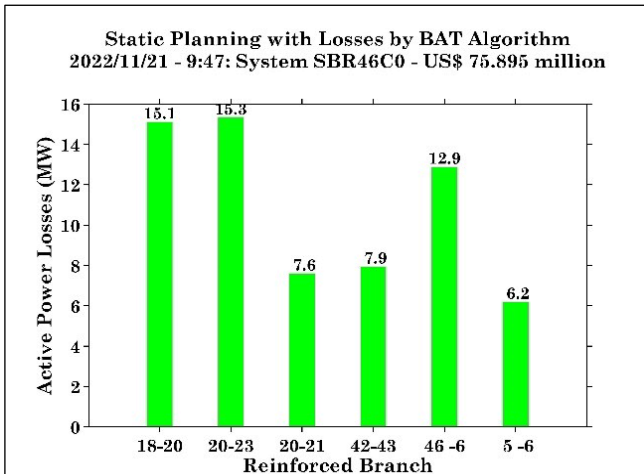


Figure 17: Case WR - SB-46/79 test system. Losses in the branches. Source: BATp optimizer, (2022).

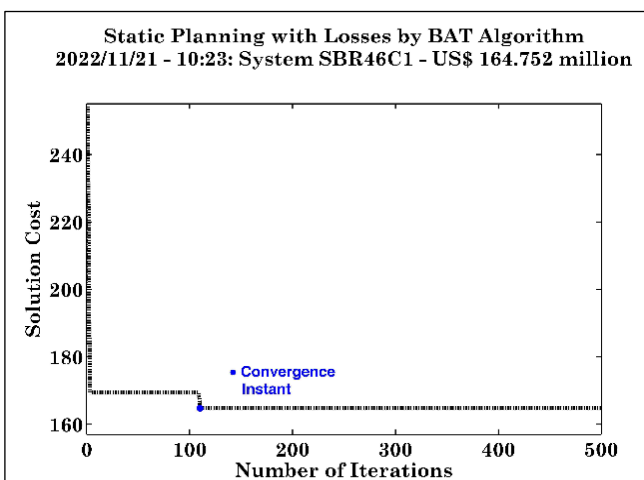


Figure 18: Case WOR - SB-46/79 test system. Cost convergence curve, Source: BATp optimizer, (2022).

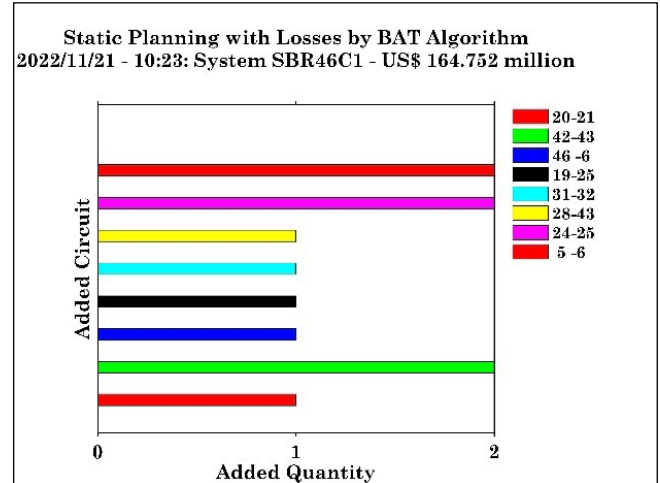


Figure 19: Case WOR - SB-46/79 test system. Planned circuits. Source: BATp optimizer, (2022).

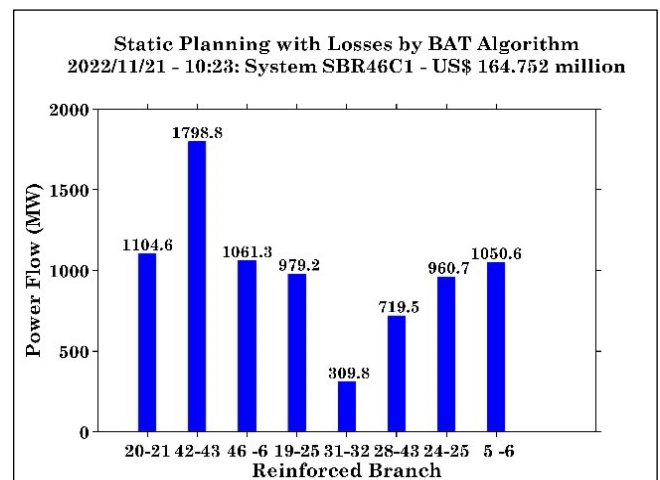


Figure 20: Case WOR - SB-46/79 test system. Flows in the branches. Source: BATp optimizer, (2022).

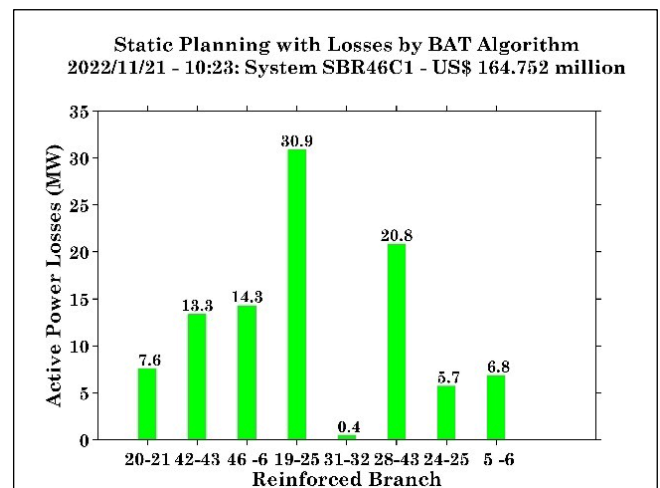


Figure 21: Case WOR - SB-46/79 Test System. Losses in the branches. Source: BATp optimizer, (2022).

V.2.4 Summary of Results

The Table 6 shows the summary of the results, illustrated in Figures 15, 17 and 19, 21, where lower amounts of circuits added on the network branches, lower investment cost (US\$ million) and lower active power loss (MW) are observed when considering generation redispatch.

Table 6: SB-46/79 test system - Comparison of the cases.

Case	Number Circuits	Added Circuits	Cost	Loss
WR	11	20-21=2, #42-43=2, #46-6=1, #19-25=1, #31-32=1, #28-43=1, #24-25=2, #5-6=1	75.895 (46.07%)	70.90 (71.03%)
WOR	8	18-20=1, #20-23=1, #20-21=2, #42-43=1, #46-6=1, #5-6=2	164.752 (100%)	99.81 (100%)

Source: Authors, (2022).

VI. CONCLUSIONS

This paper presents an optimization algorithm capable of solving the complex problem of planning the static expansion of transmission systems considering the effect of active power losses in circuits, which was represented in the equality constraints of the mathematical model. The choice of branches to perform circuit additions was made with the help of the bat algorithm, which was modified to intensify the search around the global optimal solution in each iteration. The modified bat algorithm used in the proposed algorithm belongs to the swarm intelligence paradigm and combines aspects of diversification and search intensification. Procedures for cost reduction of expensive solutions and elimination of discards of infeasible solutions were used together with a search intensification operator around the global optimal solution and with a rule that defines the population size as a function of the number of branches of the analyzed system. Given the complexity of the planning problem, the good quality results obtained with relatively low computational effort demonstrate the efficiency of the proposed optimization algorithm in all the analyzed systems, under various assumptions of generation redispatch and power balancing buses.

VII. AUTHOR'S CONTRIBUTION

Conceptualization: João Ricardo Paes de Barros.

Methodology: João Ricardo Paes de Barros.

Investigation: João Ricardo Paes de Barros.

Discussion of results: João Ricardo Paes de Barros.

Writing – Original Draft: João Ricardo Paes de Barros.

Writing – Review and Editing: João Ricardo Paes de Barros and Dimitri Albuquerque de Barros.

Resources: João Ricardo Paes de Barros.

Supervision: João Ricardo Paes de Barros.

Approval of the final text: João Ricardo Paes de Barros and Dimitri Albuquerque de Barros.

VIII. REFERENCES

- [1] G. Latorre, R. D. Cruz, J. M. Areiza, and A. Villegas, "Classification of publications and models on transmission expansion planning", *IEEE Transactions on Power Systems*, vol. 18, no. 2, pp. 938–946, 2003.
- [2] C.W. Lee, S.K.K. Ng, J. Zhong and F.F. Hu, "Transmission expansion planning from past to future", *IEEE Power System Conference*, pp. 257–265, 2006.
- [3] M. Mahdavi and H. Monsef, "Review of static transmission expansion planning", *Journal of Electrical and Control Engineering*, vol. 1, pp. 11–18, 2011.
- [4] R. Hammati, H. Ralmat-Allah and K. Amin, "State-of-art of transmission expansion planning: comprehensive review", *Renewable and Sustainable Energy Reviews*, vol. 23, pp. 312–319, 2013.
- [5] I.J. da Silva, M.J. Rider, R. Romero, A.V. Garcia and C.A. Murari, "Transmission network expansion planning with security constraints", *IEEE Proceedings, Generation, Transmission and Distribution*, vol.152, no. 6, pp. 827–836, 2005.

- [6] M.P. Moghaddam, H. Abdi and M.H. Javidi, "Transmission Expansion Planning in Competitive Electricity Markets Using AC OPF", *IEEE Power Systems Conference and Exposition*, pp. 1507–1512, 2006.
- [7] E.J. de Oliveira, I.C. da Silva Jr, J.L.R. Pereira and S. Carneiro Jr, "Transmission system expansion planning using a sigmoid function to handle integer investment variables", *IEEE Transactions on Power Systems*, vol. 20, no. 3, pp. 1616–1621, 2005.
- [8] S. de la Torre, A. J. Conejo, and J. Contreras, "Transmission expansion planning in electricity markets," *IEEE Transactions on Power Systems*, vol. 23, no. 1, pp. 238–248, Feb. 2008.
- [9] D.Z. Fitiwi, M.R. Olmos, F. de Cuadra and I.J. Pérez-Arriaga, "Finding a representative network losses model for large-scale transmission expansion planning with renewable energy sources", *Energy*, vol. 101, pp. 343–358, 2016.
- [10] E.J. de Oliveira, C.A. Moraes, L.W. Oliveira, L.M. Honório, R.P.B. Poubel, "Efficient hybrid algorithm for transmission expansion planning", *Electrical Engineering*, vol. 100, no. 4, pp. 2765–2777, 2018.
- [11] S.L. Gbadamosi, N. I. Nwulu and U. Damisa, "Impact of power losses on optimal expansion planning using quadratic programming", *IEEE 6th International Conference on Engineering Technologies and Applied Sciences*, 2019.
- [12] L.S. Nepomuceno, A.N. de Paula and E.J. de Oliveira, "Planejamento da Transmissão via Meta-Heurística Híbrida", *Simpósio Brasileiro de Sistemas Elétricos*, vol. 1, no. 1, pp. 1–6, 2020.
- [13] A. Domínguez, A.E. Zuluaga and R. Gallego, "A MILP model for the static transmission expansion planning problem including HVAC/HVDC links, security constraints and power losses with a reduced search space", *Electric Power Systems Research*, vol. 143, pp. 611–623, 2017.
- [14] A.H. Escobar, R.A. Gallego and R. Romero, "Multistage and coordinated planning of the expansion of transmission systems", *IEEE Transactions on Power Systems*, vol. 2, no. 19, p. 735–744, 2004.
- [15] S. Binato, M.V. Pereira and S. Granville, "A New Benders Decomposition Approach to Solve Power Transmission Network Design Problems" *IEEE Transactions on Power Systems*, vol. 16, no. 2, pp. 235–240, 2001.
- [16] D. Tejada, J.M. López-Lezama, M.J. Rider and G. Vinasco, "Transmission network expansion planning considering repowering and reconfiguration", *Electric Power and Systems*, no. 69, pp. 213–221, 2015.
- [17] A. Monticelli, A. Santos Jr., M.V.F. Pereira, S.H. Cunha, B.J. Park and J.C.G. Praça, "Interactive transmission network planning using least-effort criterion", *IEEE Transactions on Power Apparatus and Systems*, vol. 101, no. 10, pp. 3919–3925, 1982.
- [18] A. Mahmoudabadi and M. Rashidinejad, "An application of hybrid heuristic method to solve concurrent transmission network expansion and reactive power planning". *International Journal of Electrical Power & Energy Systems*, vol. 45, no. 1, pp. 71–77, 2013.
- [19] C.A. Moraes, E.J. de Oliveira, L.W. Oliveira and I.C. Silva Junior, "static planning of power transmission system expansion through bioinspired optimization technique". *12th CLAGTEE - Latin America Congress on Electricity Generation and Transmission (in Portuguese)*, pp. 1–8, 2017.
- [20] P.V. Gomes, and J.T. Saraiva, "State-of-the-art of transmission expansion planning: a survey from restructuring to renewable and distributed electricity markets", *International Journal of Electrical Power & Energy Systems*, no. 111, pp. 411–424, 2019.
- [21] L.F. Fuerte-Ledezma, G. Gutiérrez-Alcaraz and M.S. Javadi, "Static transmission expansion planning considering uncertainty in demand using BPSO", *North-American Power Symposium*, pp. 1–6, 2013.
- [22] X-S. Yang, "A new metaheuristic Bat-inspired algorithm", *Nature Inspired Cooperative Strategies for Optimization*, vol. 284, pp.65–74, 2010.
- [23] G. Wang and L. Guo, "A Novel Hybrid Bat Algorithm with Harmony Search for Global Numerical Optimization", *Journal of Applied Mathematics*, pp. 1–22, 2013.
- [24] S. Yilmaz and E.U. Kucuksille, "Improved at algorithm (IBA) on continuous optimization problems", *Lecture Notes on Software Engineering*, vol. 1, no. 3, 2013.

- [25] S. Yilmaz and E.U. Kucuksille and Y. Cengiz, "Modified bat algorithm", *Elektronika ir Elektrotechnika*, vol. 20, no. 2, pp. 71-78, 2014.
- [26] T-S. Pan, T-K. Dao, T-T. Nguyen, S-C. Chu, "Hybrid particle swarm optimization with Bat algorithm", *Genetic and Evolutionary Computing, Advances in Intelligent Systems and Computing*, 329, pp. 37-47, 2015
- [27] S. Vijayaraj and R.K. Santhi, "Multi-Area economic dispatch with valve point effect using improved Bat algorithm", *International Journal for Research in applied Science & Engineering Technology*, vol. 4, no. X, pp. 477-484, 2016.
- [28] M.R. Ramli, Z.A. Abas, M.I. Desa, Z.Z. Abidin and M.B. Alazzam, "Enhanced convergence of Bat algorithm based on dimensional and inertia weight factor", *Journal of King Saud University - Computer and Information Sciences*, pp. 1-8, 2018.
- [29] C.A. Moraes, E.J. de Oliveira, L.W. Oliveira and I.C. Silva Junior, "Static planning of power transmission system expansion through bioinspired optimization technique", *12th Latin-American Congress on Electricity Generation and Transmission*, pp.1-5, 2017.
- [30] K. Veeresham and K. Vaisakh, "Bat algorithm based optimal transmission expansion planning with generator/load models and frequency controls", *International Journal of Electrical, Electronics and Data Communication*, vol. 3, no. 11, pp. 44-50, 2015.
- [31] P.C. Chu and J.E. Beasley, "A genetic algorithm for the generalized assignment problem", *Computer & Operations Research*, vol. 24, no. 1, pp. 17-23, 1997.
- [32] J.R.P. Barros and D.A. Barros, "Transmission network expansion planning considering security constraints via African buffalo algorithm", *Journal of Engineering and Technology for Industrial Applications*, vol. 8, pp. 44-52, 2022.
- [33] R.Y.M. Nakamura, L.A.M. Pereira, K.A. Costa, D. Rodrigues, J.P. Papa and X-S Yang, "BBA: A binary Bat algorithm for feature selection", *Brazilian Symposium of Computer Graphic and Image Processing*, pp. 291-297, 2012.
- [34] G. Wang and L. Guo, "A Novel Hybrid Bat Algorithm with Harmony Search for Global Numerical Optimization", *Journal of Applied Mathematics*, pp. 1-22, 2013.
- [35] G.I. Evers and M.B. Ghalia, "Regrouping particle swarm optimization: A new global optimization algorithm with improved performance consistency across bench-marks", *IEEE International Conference on Systems, Man and Cybernetics*, pp. 3901-3908, 2009,
- [36] A.J. Monticelli, "Fluxo de carga em redes de energia elétrica", Editora Edgard Blücher Ltda, 1983.
- [37] R. Romero R. Romero, A. Monticelli, A. Garcia and S. Haffner, "Test systems and mathematical models for transmission network expansion planning", *IEE Proceedings Generation, Transmission and Distribution*, vol. 149, no. 1, pp. 27-36, 2002.
- [38] S.M. Sait and H. Youssef, "Iterative computer algorithms with applications in engineering: Solving combinatorial optimization problems", *IEEE Computer Society Press*, 1999.
- [39] R.A. Gallego, A. Monticelli and R. Romero, "Transmission system expansion planning by an extended genetic algorithm", *IEEE Proceedings, Generation, Transmission and Distribution*, vol. 145, pp. 329-335, 1998.
- [40] S. Haffner, A. Monticelli, A. Garcia, J. Mantovani and R. Romero, "Branch and bound algorithm for transmission system expansion planning using a transportation model", *IEE Proceedings Generation, Transmission and Distribution*, vol. 147, no. 3, pp. 149-156, 2000.
- [41] I.J. da Silva, M.J. Rider, R. Romero, A.V. Garcia and C.A. Murari, "Genetic algorithm of Chu-Beasley for static and multistage transmission expansion planning", *Power Engineering Society General Meeting*, pp. 1-7, 2006.
- [42] R. Villasana, L. L. Garver and S. J. Salon, "Transmission network planning using linear programming", *IEEE Transactions on Power Systems*, PAS-104, pp. 349-356, 1985.
- [43] S.L.S. Tagliarenha, "Novas Aplicações de Metaheurísticas na Solução do Problema de Planejamento da Expansão do Sistema de Transmissão de Energia Elétrica", *Tese de Doutorado em Engenharia Elétrica, Universidade Estadual Paulista - UNESP, Ilha Solteira*, 2008.
- [44] C. Grigg, P. Wong, P. Albrecht et al., "The IEEE Reliability Test System-1996. A report prepared by the Reliability Test System Task Force of the Application of Probability Methods Subcommittee", *IEEE Transactions on Power Systems*, vol. 14, no. 3, pp. 1010-1020, 1999.
- [45] N. Alguacil, A. L. Motto, and A. J. Conejo, "Transmission expansion planning: a mixed-integer LP approach," *IEEE Transactions on Power Systems*, vol. 18, no. 3, pp. 1070-1077, 2003.
- [46] M.J. Rider, A.V. Garcia, and R. Romero, "Transmission system expansion planning by a branch-and-bound algorithm", *IET Generation, Transmission and Distribution*, vol. 2, no. 1, pp. 90-99, 2008.
- [47] R. Fang and D.J. Hill, "A new strategy for transmission expansion in competitive electricity markets", *IEEE Transactions on Power Systems*, vol. 18, no. 1, pp. 374 - 380, 2003.
- [48] R. Romero, C. Rocha, J.R.S. Mantovani and I.G. Sanches, "Constructive heuristic algorithm for DC model in network transmission planning", *IEE Proceedings Generation, Transmission and Distribution*, vol. 152, no. 2, pp. 277-282, 2005.
- [49] H. Mori and Y. Iimura, "Transmission Network Expansion Planning with a Hybrid Meta-heuristic Method of Parallel Tabu Search and Ordinal Optimization", *14th International Conference on Intelligent System Applications to Power Systems*, pp. 1-6, 2007.
- [50] C. Rathore, R. Roy, S. Raj and A.K. Sinha, "Mosquitoes-behavior based (MOX) evolutionary algorithm in static transmission network expansion planning", *IEEE International Conference on Energy Efficient Technologies for Sustainability*, pp. 1006-1011, 2013.
- [51] C. Rathore, S. Raj, A.K. Sinha, R. Roy, "Improved-mosquitoes-behavior based (I-MOX) evolutionary algorithm in transmission network expansion planning", *IEEE International Conference on Control Instrumentation, Energy & Communication (CIEC)*, pp. 538-543, 2014.
- [52] A. Monticelli, J. R. Santos, M. V. F. Pereira, S. H. A. Cunha, B. J. Parker, and J. C. G. Praça, "Interactive transmission network planning using a least-effort criterion", *IEEE Transaction on Power Systems*, vol. 101, pp. 3919-3925, 1982.
- [53] E.L. da Silva, J.M.A. Ortiz, G.C. Oliveira and S. Binato, "Transmission network expansion planning under a tabu search approach", *IEEE Transactions on Power Systems*, vol. 16, no. 1, pp. 62-68, 2001.
- [54] A. Verma, B. K. Panigrahi and P. R. Bijwe, "Harmony search algorithm for transmission network expansion planning", *IET Generation, Transmission and Distribution*, vol. 6, No. 4, pp. 663-673, 2010.



NATURE OF DISPERSION: ITS RELATIONSHIP WITH SOME FRACTAL AND THERMODYNAMIC PHENOMENA

Alfredo José Constain¹, Gina Peña Olarte² and Carlos Peña Guzman*³

^{1,2} FLUVIA SAS. Bogotá, Colombia.

³ Environmental and Sanitary Engineering Program, La Salle University, Bogotá, Colombia.

¹ <http://orcid.org/0000-0001-6442-0715> , ² <http://orcid.org/0000-0002-8727-9088> , ³ <http://orcid.org/0000-0003-0496-9612> 

Email: alfredo.constain@gmail.com, ginap.olarte@fluvia.co, *carpeguz@gmail.com

ARTICLE INFO

Article History

Received: January 30th, 2023

Accepted: February 21th, 2023

Published: February 28th, 2023

Keywords:

Tracers,
Thermodynamics,
Dispersion,
Chaos,
Fractals.

ABSTRACT

Water quality studies, vital for the development of human civilization, critically depend on the reliability and accuracy of the environmental and geomorphological data fed by the models. Nowadays, tracers are widely used to obtain this kind of data, however, many methodological and technical problems persist about them, which make it difficult for the specialist to properly manage time and costs. This article presents an alternative methodology, based on a state function, which accurately describes the phases of evolution of the solutes in the flow. From their analysis it is clear that the "abnormal bias" observed in the tracer curves correspond not to effects of flow (as stated in the dead zone theory) but to effects of the chemistry of the solute dissolving in water. This different approach allows to improve the corresponding interpretations and calculations of tracers used in field. Experiments are presented at the end that are interpreted with the proposed state function.



Copyright ©2023 by authors and Galileo Institute of Technology and Education of the Amazon (ITEGAM). This work is licensed under the Creative Commons Attribution International License (CC BY 4.0).

I. INTRODUCTION

Water Quality studies have become essential tools for the control and improvement of the conditions of use of water resources, so threatened by a growing anthropic activity. However, currently, and despite spectacular advances in digital computing, theoretical tools suffer from great backwardness, since they correspond to complex models, developed in the last quarter of last century.

This article presents new developments in the understanding of the Advection-Diffusion phenomenon, especially with the development of a state function, $\phi(U, E, t)$, which describes the evolution of the tracer cloud at different stages. This function connects with certain contemporary notions, corresponding to Feigenbaum's infinite bifurcation model, and also puts into play experimental results of great importance, such as the Svedberg constant, obtained in his investigations of Brownian particles in aqueous media, carried out with ultra-centrifugation, at the beginning of the 20th century.

These new concepts put in mutual connection, allow us to have new and powerful tools to properly interpret the complex phenomena of water pollution in the modern world. In this article, the word "solute" and "tracer" are used interchangeably. On the understanding that current engineering techniques used almost exclusively saline tracers, or fluorescent tracers, which dissociate into charged units (ions) as a result of their interaction with water.

II. DISPERSION AS A MOLECULAR PHENOMENON

II.1 ELEMENTARY DIFFRACTION OF PARTICLES IN THE FLOW, AND ITS MEANING

The molecular vision of dispersion has been defined by the author [1] as the random separation of any pair of particles, N and W , by the effect of a "diffraction" element, D , (which can be a physical obstacle or a velocity differential in the shear dynamic field of the flow), which generates a characteristic separation, Δ , at a characteristic time, τ , valid for multiple scales. Figure 1.

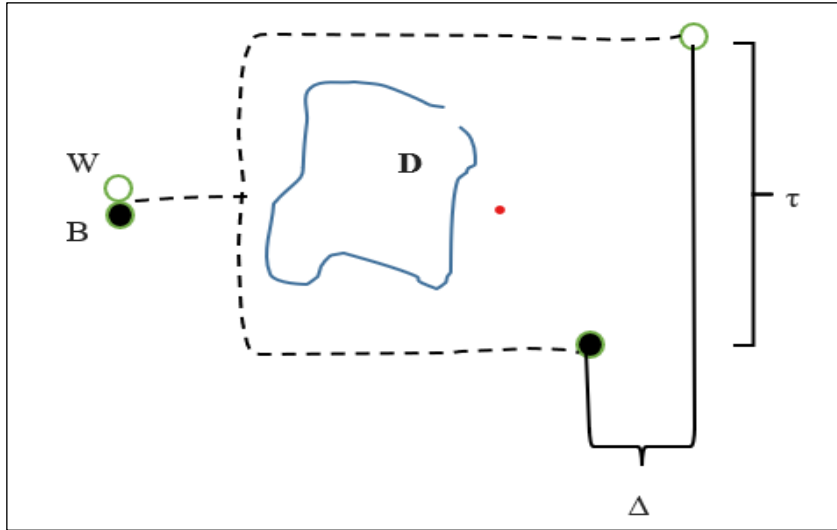


Figure 1: Random separation of a couple of particles.
Source: Authors, (2023).

It is now necessary to give a more precise meaning, both to Δ , and to τ , from concepts of the kinetic theory of liquids [2] developed by Y. Frenkel, as follows [3]:

Let be a group of tracer particles you inject suddenly into a flow, generating a concentration gradient between its center of mass and the liquid environment. The one-dimensional motion of each particle is random, insofar as it is immersed in a thermal environment, with equal probability of going left or right. Despite the individual randomness of motion of each particle, at each point of the distribution there will be a "previous point" at which the concentration is greater than at a "posterior point", Farther from the center of mass, therefore there will be more mobile particles at that first point than at the second, which generates an imbalance in the number of particles that move away from the center, from those that move away. The average displacement of the set, called "Diffusion", must be calculated by means of the squares of the individual displacements, x_j^2 for its definition to make experimental sense:

$$\langle x^2 \rangle \approx \frac{x_1^2 + x_2^2 + \dots + x_n^2}{N} \quad (1)$$

Since the number of observed displacements is proportional to time, the following one-dimensional proportionality can be written as:

$$\langle x^2 \rangle \approx 2 * D * t \quad (2)$$

If the motion of the particles of the solute within the fluid is interpreted as in sequence of jumps, whose number is precisely "N", then for a single hop ($N = 1$) one can write, with " τ " the characteristic time for a jump:

$$\Delta^2 \approx 2 * D * \tau \quad (3)$$

Therefore:

$$\Delta \approx \sqrt{2 * D * \tau} \quad (4)$$

And one can then define a "dispersion" velocity, related to Figure 1, as follows: [4].

$$V_{disp} \approx \frac{\Delta}{\tau} \approx \frac{\sqrt{2 * D * \tau}}{\tau} \approx \sqrt{\frac{2 * D}{\tau}} \quad (5)$$

It is useful then to define a dimensionless function of the form:

$$\phi \approx \frac{V_{disp}}{u} \quad (6)$$

This function can be shown to be a "thermodynamic potential" since it satisfies Schwartz conditions [5]:

$$\oint d\phi = 0 \quad (7)$$

In addition, its expanded form is:

$$U \approx \frac{1}{\phi} \sqrt{\frac{2 * D}{\tau}} \quad (8)$$

Equation for the mean velocity of flow, which has an analytic form similar to the Chezy-Manning equation for uniform flow.

II.2 BALANCE OF ENERGIES IN THE TRACER SYSTEM AND ITS RELATIONSHIP WITH THE CURVE OF THE STATE FUNCTION AND THE PROCESSES OF EVOLUTION OF THE TRACER PLUME

When the tracer suddenly enters the turbulent flow, it is accompanied by an energy of its structure, called "enthalpy of formation", ΔH_o [6].

This energy is used to configure the different interactions of the particles of the solute, and are of two types:

A.- Initial energy associated with the static crystal itself, ΔX_{tal} at the beginning of the process;

B.- Energy associated with the distribution of the chemical potential, in the later stage, ΔChe .

$$\Delta H_o \approx \Delta X_{tal} + \Delta Che \quad (9)$$

In the initial process, called "solvation", the dipole particles of water act electrically on the ions of the solute, surrounding them and forming complex units, destroying their initial structure. In a second process, with the solvated particles already "loose", a

distribution is established in the flow that is associated with a gradient of chemical potential.

In this process of destruction, water uses a certain thermal energy, Δq_{ext} , which equals Δx_{tal} . [7]

$$\Delta q_{ext} \approx \Delta x_{tal} \quad (10)$$

In addition to this balance, energies enter the system from outside, consisting of a kinetic part, ΔK , (flow velocity), and a potential part, ΔE , which constitute the gravitational part (of the slope of the flow), and also heat is expelled to the outside, ΔQ , product of all the processes of irreversible degradation. Figure 2. [8].

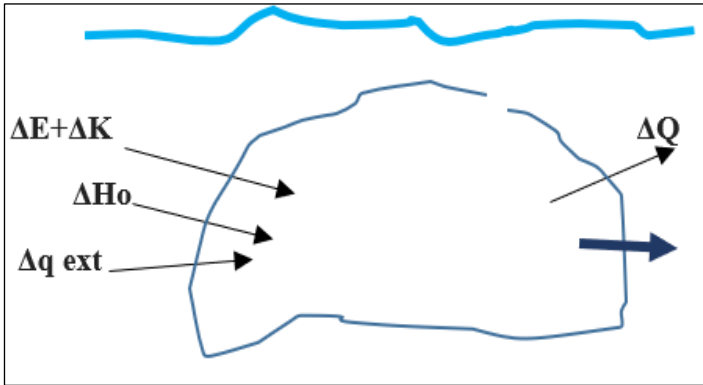


Figure 2: System's energies and in its surroundings. Source: Authors, (2023).

The general balance is:

$$\Delta E + \Delta K \approx \Delta Q \quad (11)$$

To represent the evolution of the plotter cloud, one has that the variation of the State function, $\phi(t)$ is. Figure 3:

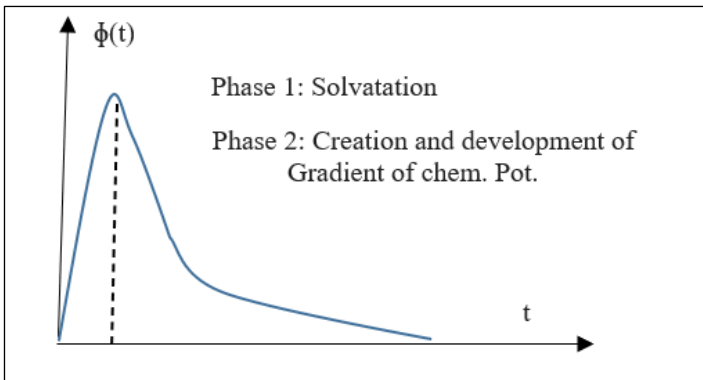


Figure 3: Variation of state Function. Source: Authors, (2023).

The first process (Phase 1) is relatively fast and $\phi(t)$ goes from 0 to $\phi_{max} \approx 2.16$, and the second (Phase 2) is much slower and goes from the peak of the state function to its extinction at equilibrium. Phase 1 (ascending) corresponds to the "dipole-ion" interaction that is associated with solvation, while phase 2 (descending) corresponds to the "ion-ion" interaction, which represents the formation of an "ionic cloud" that surrounds each ion, and that is diluted as time passes [9-10].

In phase 2, the "ionic clouds" generate an extra volume to each particle, which offers an additional effect of resistance by viscous friction, called "Einstein-Stokes", which is diluted over

time by gradual destruction of these clouds. This effect leads to a "delay" of the plotter that moves with a velocity, u , less than that of the flow, U .

As the tracer plume advances in the flow, the gradual destruction of the aforementioned "ionic clouds" decreases the effective radii of the tracer particles, that is, decreasing the viscous resistance, and therefore increasing the effective speed of these particles. When a point is reached where the "clouds" disappear, the plotter particles are coupled in speed to the flow itself. Figure 4.

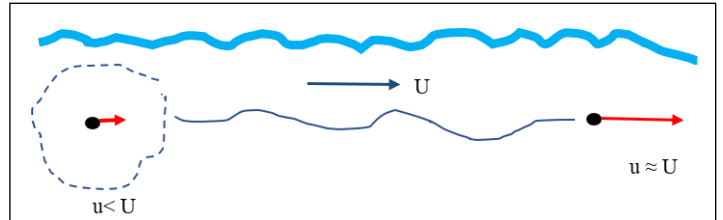


Figure 4: Retardant effect of the ionic atmosphere by the Einstein-Stokes effect. Source: Authors, (2023).

II.3 THE "EINSTEIN-STOKES" EFFECT AS A REAL CAUSE OF "NON-FICKIAN" BIAS IN REAL TRACER CONCENTRATION CURVES

From the Fick Adveccion-Dispersion transport equation, (12) the following analysis can be made with respect to the pronounced "bias" that is detected in the experimental curves, but which does not correspond to this theoretical model, therefore called "non-Fickian bias":

$$C(x, t) \approx \frac{M}{Ayz\sqrt{4\pi+E}t} * e^{-\frac{(Xo-U*t)^2}{4+E*t}} \quad (12)$$

While a certain "normal" bias effect of the Galileo transformation must appear in this equation, (Black Curve) Figure 5.

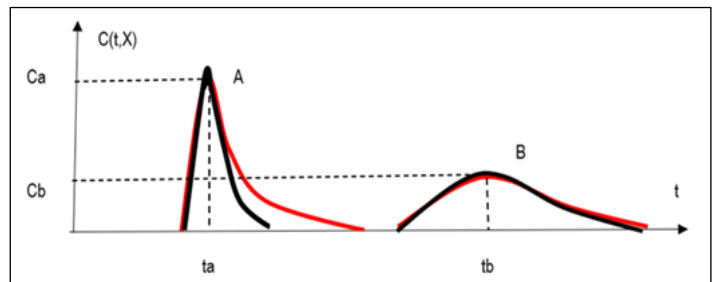


Figure 5: Decreasing bias over time of sequential Fickian tracer curves in the flow. Source: Authors, (2023).

Represented with the difference $(Xo-U*t)$ in the exponential quadratic argument, seen by a fixed observer on the banks of the channel (Beiser, 1977), the degree of "asymmetry" of this bias in the experiments (red curve) [11-12], has been much greater than expected, especially in the initial phase of the evolution of the tracer in the flow, forming a long "unexplained" tail (Curve A) that becomes more symmetrical over time. (Curve B).

At the same time, several alternatives have been proposed to solve this enigma, generally derived from the reactor models of chemical engineering. among them the theories ("Aggregated Dead zone", ADZ, and Transient storage" TS), which base the existence

of non-Fickian "bias" in the operation of the so-called "Dead Zones", Those located on the periphery of the channels, perform a "trapping" of the particles of the solute, and then release this mass, and thus configure a supposed mechanism that delays the tracer. [13-14].

This mechanism operates on the basis of a mass exchange between the central zone (Bulk zone) with Concentration " C_b ", completely mixed, and the peripheral zones, with concentrations " C_d ", and therefore bases the nature of the anomaly of the "long tails" in an exclusive defect of the flow, Figure 6.

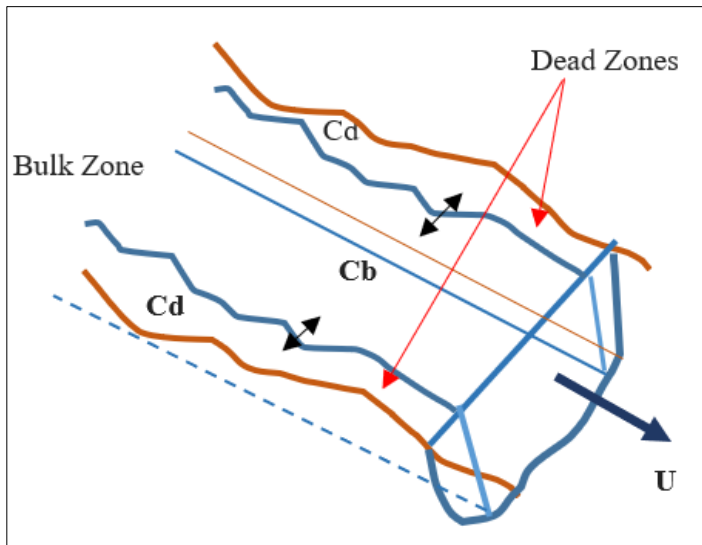


Figure 6: Geometric model of "Dead Zones".
Source: Authors, (2023).

The truth is that although they yield correct results, their mechanisms suffer from great mathematical complexity, and present the problem that the "trapping" of tracer particles in the peripheral zone necessarily requires the realization of a certain work against the forces of interaction, which the system cannot perform because being a "totally irreversible" process, all the energy that is delivered from the outside is transformed into heat, as the 2nd Principle preaches. The only alternative would be to provide this work from the outside, but this is not feasible either because it is assumed that the tracer is totally conservative, and nothing can hold it back.

Additionally, the results of the equations of the ADZ and TS methods are supported by computer programs (of the Monte Carlo type) that greatly obscure their analytical effectiveness. [15-16]. These methods give the flow (and not the tracer) the very mechanics of scattering with pronounced biases.

As seen earlier in this article, if the "Einstein-Stokes" effect is considered, due to the dependence of the speed of the tracer cloud (of its centroid), u , with this effect, it gradually couples its velocity with the velocity of the flow, U , until finally all the mass of the tracer is transported with this average velocity. It is evident that the "non-Fickian bias" is due not to a defect of the flow, but to the physico-chemical of the solute in the water, dependent that if on the turbulence of the medium.

II.4 THE MECHANISM OF IRREVERSIBILITY: BROWNIAN MOTION, AND ARROW OF TIME

The nature of the motion of solute particles in a flow undergoing a concentration gradient (actually of chemical potential) has a double facet: At the basic (individual) level each particle, " P ", has the possibility of going "back" or "forward"

(contrary arrows), but at the collective level there is a net movement of the tracer pen, expanding radially, relative to its center of mass Figure 7.

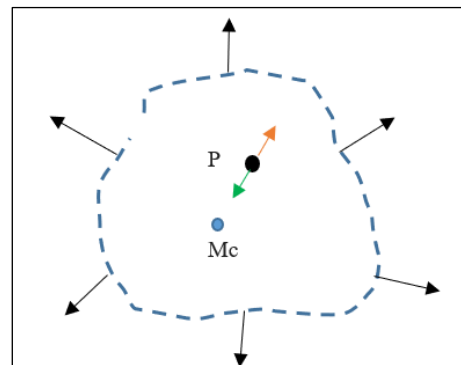


Figure 7: Complex movement of the tracer plume.
Source: Authors, (2023).

It can be seen then that at the same time that there is the basic randomness in each step of the Brownian motion (zigzag, forward backward), of each particle, there is an "arrow of time" (unidirectional) related to the increase in volume of the tracer with time.

This behavior can be put graphically as a tree of bifurcations in time and space, indicating that the individual random "decisions" of each particle are made in very short, medium and large times (distances), and the advance of the whole was getting bigger and bigger, Figure 8.

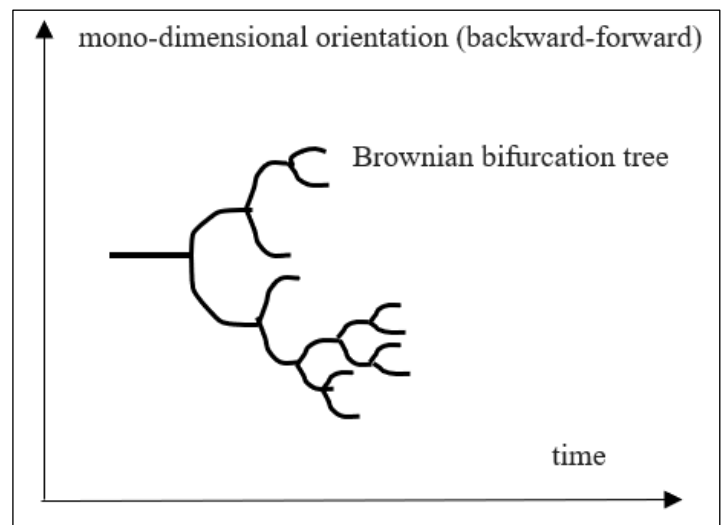


Figure 8: Brownian branching tree of the tracer.
Source: Authors, (2023).

As can be seen, these bifurcations occur on all scales, that is, it is a fractal phenomenon, mathematically defined by a "Law of powers", also called "Law of self-similarity". For this reason, it can be accepted that both the characteristic distance and time, Δ and τ of the Brownian jumps in Figure 1, they occur at all scales.

II.5 RELATION BETWEEN " τ " and " t ", FEINGENBAUM'S CONSTANT, AND SVEDBERG'S CONSTANT

Since the mid-1960s the foundations of the nonlinear theory of phase transitions were established through the technique of "renormalization", and from which R. Feigenbaum developed the concept of "period doubling" in nonlinear physical systems

(monomodal), such as the logistic function of growth [17], arriving at the definition of the ratio of "scaling", with a definition of geometric progression of the type:

$$\delta = \lim \frac{\lambda(n) - \lambda(n-1)}{\lambda} \approx 4.6692 \quad (13)$$

The adjacent values of " λ " are getting closer and with shorter branches, progressing geometrically, accumulating duplications towards chaos, being strictly an "eigenvalue" of an operator. For this case, values of " λ " correspond to the independent variable, which defines the points at which the bifurcations occur, and when " λ " is the time, we speak of "period doubling". Since Feigenbaum presented his formula, it has been proven that this ratio is a universal value of self-equal phenomena (fractals) including turbulence and diffusion.

It can then be proposed that the times involved in the tree of Brownian bifurcations will be subject to a pattern of geometric progression of the Feigenbaum type. For this it must be remembered in principle, that Brownian motions are normally distributed, and therefore fulfill the probabilistic function of Gauss. In this sense, an arbitrary particle that runs through a Brownian system will spend different "residence times", $\theta\sigma$ and $\theta\infty$, depending on whether it travels the curve between $-\sigma$ and $+\sigma$, or that it travels from $-\infty$ to $+\infty$, as shown in Figure 9.

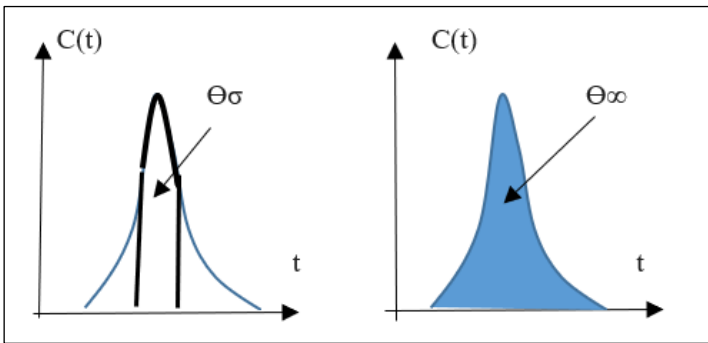


Figure 9: Two residence times of the particle. Source: Authors, (2023).

Their ratio is, in terms of notable areas and values of concentration [18]:

$$r = \frac{\theta\sigma}{\theta\infty} \approx \frac{\int_{-\sigma}^{+\sigma} c(t)dt}{\int_{-\infty}^{+\infty} c(t)dt} \approx \frac{\int_{-\sigma}^{+\sigma} c(t)dt}{\int_{-\infty}^{+\infty} c(t)dt} \approx \frac{0.683}{0.997} \approx 1.54 \quad (14)$$

This is an average value found by T. Svedberg in his studies of the distribution of Brownian particles in the ultracentrifuge, being a characteristic value of these distributions. [19] Now, if one considers that the Poisson probabilistic distribution is widely used in physics for counting "rare" events in infinite succession. [20] The count of the arrival time of Brownian particles, as "rare" particles (scarce in the flow) can then be performed with this distribution, around the mean value " $r \approx 1.54$ ", and from the characteristic time, τ , and $n \approx \infty$:

$$t \approx \tau \left(1 + 1.54 + \frac{1.54^2}{!} + \dots + \frac{1.54^n}{n!} \right) \approx \tau * 4.669 \quad (15)$$

This result is remarkable, because it shows the intimate relationship between Brownian motion (fractal) and the geometric

progression of Feigenbaum bifurcations, establishing that time in the Brownian sequence is an infinite process towards chaos, [21].

III. ADVECTION-DISPERSION AS A MACROSCOPIC PHENOMENON

Based on previous theoretical developments, it is proposed to analyze different aspects of Adveccion-Dispersion as a phenomenon on a human scale, especially the explanation of the effect of "bias" in the experimental curves of tracer, and the relationship between the different magnitudes in the evolution of the conservative solute cloud.

III.1 SCOPE OF THE CALCULATION OF DISTANCE, Δ AND VARIANCE, σ , FOR DISPERSION

As we have seen, the characteristic distance, Δ , has a "local" meaning, closer to molecular concepts of Brownian motion, and likewise the characteristic time, τ , which of course has an essential nature, of passage from one equilibrium point to another equilibrium point in the quasi-crystalline lattice of the liquid, [22]. These equilibrium points are places of "vacancy" that fill the tracers ions, before and after the jump, Figure 10.

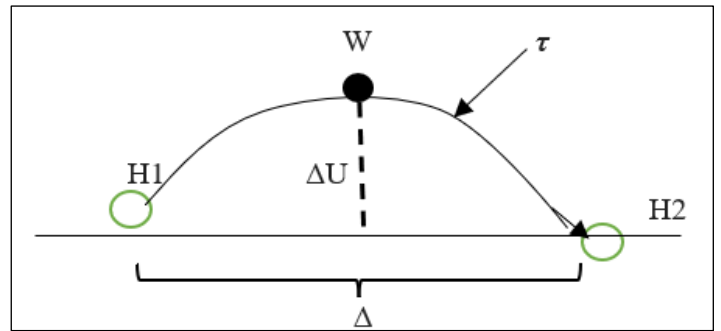


Figure 10: Jump of the particle, from one hole to another. Source: Authors, (2023).

This passage of a particle from one point to another of the liquid of the flow is actually made from "energy jumps," from one "hole" to another, for which the particle must have sufficient energy to cross the "potential barrier", ΔU , which separates one "hole" from the other, [23]. That energy needed for that jump is called " W ," and it's called "activation energy".

When talking about diffusion in macroscopic domains, the "local", Brownian approach is transcended, and the concept of Statistical Distribution must be used, in which "local" events add to infinity. There operates the probabilistic distribution "Normal" (Gaussian), Figure 11.

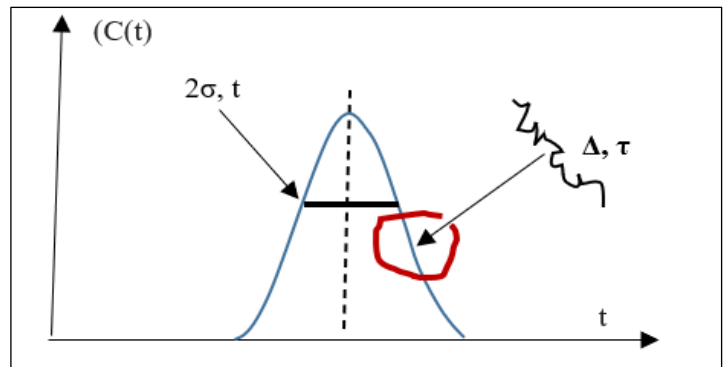


Figure 11: Macro and micro vision in dispersion. Source: Authors, (2023).

For the macroscopic field the following expression is valid, in which due to its general character the Longitudinal transport coefficient, E, and the macroscopic time, t: [24].

$$\sigma_x \approx \sqrt{2 * E * t} \quad (16)$$

It must be compared with the expression "local", equation (4), and the relationship between σ_x , and Δ is:

$$\Delta \approx \frac{\sigma_x}{\sqrt{\delta}} \quad (17)$$

Now, to estimate the temporal variance, σ_t , the average velocity of the flow must be used.

$$\sigma_t \approx \frac{\sigma_x}{U} \quad (18)$$

Combining equation (4) with the previous ones, from (16) to (18), we have:

$$\tau \approx \frac{\sigma_t}{\phi * \sqrt{\delta}} \quad (19)$$

In this way we have the definitions that allow to elucidate the mechanics of the Dispersion in turbulent natural flows, including "local" and general parameters.

III.2 APPLICATION OF THE "COMPLETE MIXTURE" CRITERION BASED ON THE "EINSTEIN-STOKES" EFFECT

It is interesting to apply the above criterion in the experimental tracer curves. As an exercise it would be calculated as follows.

A.- The value of ϕ for the most initial condition, moments after injection, when the solute has been solvated in a first phase of the evolution of the tracer pen. This occurs when the macroscopic time, "t", is worth $tp \approx \sigma t$, which is the smallest possible value, Figure 12.

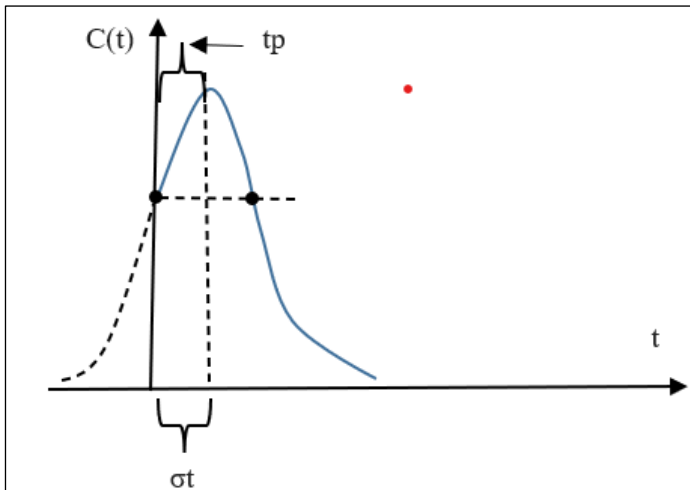


Figure 12: Minimum time in the evolution of the plume. Source: Authors, (2023).

In this case. At the very beginning of the evolution of the pen, we will have:

$$\tau \approx \frac{tp}{\delta} \approx \frac{tp}{\phi * \sqrt{\delta}} \quad (20)$$

Therefore, at the very beginning of Phase 2: $\phi \approx \sqrt{\delta} \approx 2.16$

B.- The value of ϕ when there is "Complete mixture", that is, when the tracer cloud has achieved a time $tp \approx 4\sqrt{2} * \sigma t$, since for that circumstance approximately 99.7% of the mass of the solute is "free" to participate in transport with a speed equal to that of the flow itself, that is, the effect of additional viscous friction has practically disappeared. This situation is shown in Figure 13.

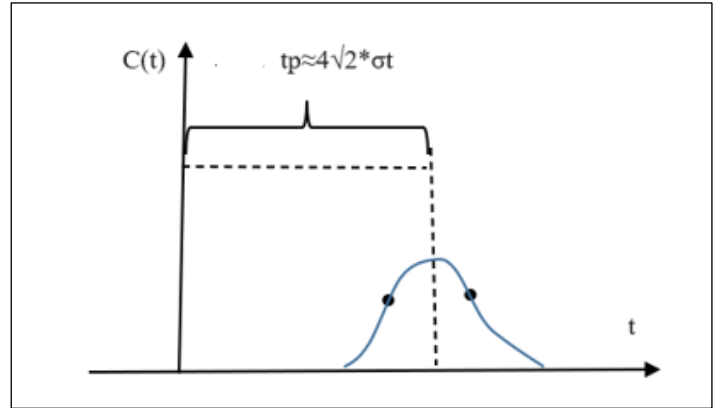


Figure 13: "Complete mix" condition on tracer. Source: Authors, (2023).

If we replace the value of the longitudinal dispersion coefficient of equation (8) into Fick's classical equation (12) an extension of that equation remains, containing the Flow, the Feigenbaum fractal constant, and the State function [25]:

$$C(x, t) \approx \frac{M}{Q * \phi * t^{1.16}} * e^{-\frac{(x-t)^2}{2 * (\frac{E}{\delta}) * (\phi * t)^2}} \quad (21)$$

Note how this new longitudinal tracer transport equation includes both the state function, the Feigenbaum's number and the flow, likewise, it is verified that this new equation adequately represents the experimental tracer curves with the appropriate bias, even under medical conditions close to the time of injection.

IV. VERIFICATION OF THE CALIBRATION OF TRACER MEASUREMENT EQUIPMENT

One of the recurring themes in the experimental work is the verification of the calibration of the equipment, that is, to have technical criteria that indicate when a team is out of specification in terms of its precision and accuracy [26].

IV.1 ECUACIONES PARA VERIFICAR LA CALIBRACION DE EQUIPOS DE FLUORIMETRIA

The authors have previously proposed formulas to estimate $\phi(t)$, and $Cp(t)$, linked as basic data to perform such verifications. As follows: [27].

$$Cp(t) \approx \alpha * tp^{-b} \quad (22)$$

Where "b" is an exponent that is chosen in such a way that the equations agree but is usually set around $b \approx 2/3$ [28].

$$\phi(t) \approx \frac{M}{Q * \alpha^{1.16}} * \frac{1}{t^{(1-b)}} \quad (23)$$

Note that equation (22) actually defines the envelope of concentrations at subsequent points in time. Note also, that the numerical value of " α " is a common element to magnitudes that depend only on time ("horizontal"), as well as magnitudes that depend only on the Concentration ("vertical"), so in principle, when calculated "independently", and if they converge to the expected common result, the Measurement (and therefore the Calibration) can be considered adequate. Figure 14.

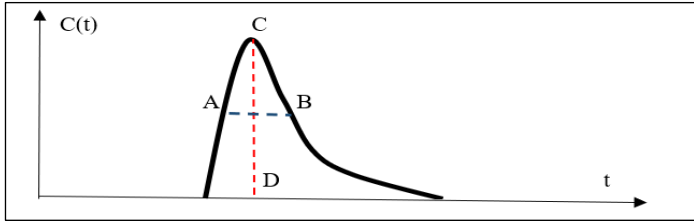


Figure 14: Independent "horizontal" and "vertical" measurements. Source: Authors, (2023).

For a case being studied, $\phi(t)$ is a "horizontal" magnitude (which depends EXCLUSIVELY on time, and is measured between the two inflection points A and B, blue), while $Cp(t)$ is a "vertical" magnitude, which depends EXCLUSIVELY on the Calibration, and is measured between points C and D, red), and therefore its analysis can yield clues as to whether the calibration is correct, or eventually if there is a problem with the sensor.

Then, if calculated Cp (C-D) with the data of ϕ (A-B) and do not match experimentally, it must be investigated if it is a problem of CALIBRATION, or if for any other reason the sensor is not measuring properly, and it should be relocated.

IV.2 DOCUMENTED EXPERIMENTS ON THE RIVER SEVERN, IN THE UNITED KINGDOM[29] IN 1986 WITH RHODAMINE WT. ANALYSIS OF THE BEHAVIOR OF " α "

This experimental study of scattering using fluorescent tracers was conducted in the River Severn (Wales) by T.C. Atkinson, P.M. Davies, and T.M. L. Wingley of the United Kingdom (Davis et al, 2000). For the original study, tracer measurements are made over a long stretch of 14 kilometers (between Llanidloes and Caersws) using six gauging points (stations A to G) placed one behind the other at this distance.

The tracer used is Rhodamine WT 20% ($M \approx 1\text{kg in } 5\text{ Liters}$, H_{20} distilled). The area of the mean cross section is $A_{yz} \approx 12.72\text{ m}^2$, the average velocity of flow is $\langle U \rangle \approx 0.70\text{ m/s}$, so the average estimated flow rate is $\langle Q \rangle \approx 7.54\text{ m}^3/\text{s}$. Appearance of the channel in Caersws is shown in Figure 15.



Figure 15: Aspects of the River Severn (Caersws, Wales). Source: Authors, (2023).

The experimental curves of Rhodamine WT of $Cp(tp)$ for the different distances are shown. Figure 16.

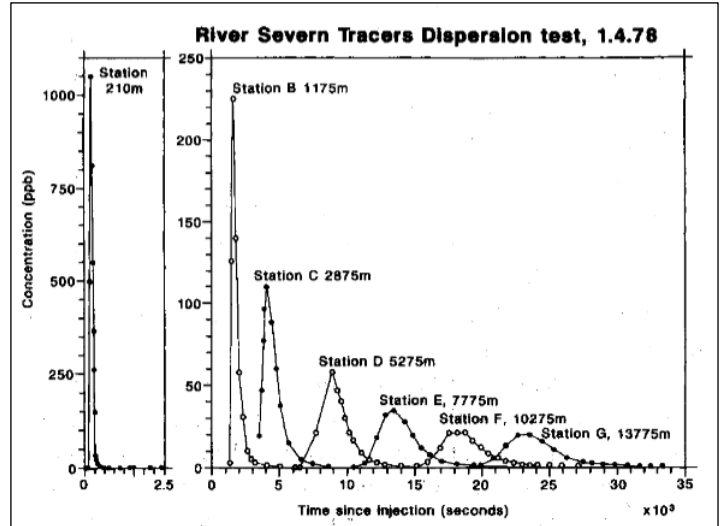


Figure 16: Distribution of Cp vs tp in the river Severn. Source: Authors, (2023).

The following Table 1 condenses the basic data of these 7 experiments with RWT, which are plotted with a potential experimental modeling of EXCEL in Figure 17.

Table 1: Main data on 7 tracer experiments in River Severn.

	A	B	C	D	E	F	G
Cp (Ppb)	1050	225	110	58	34.5	21	20
tp (s)	300	1740	4140	8880	13440	18120	23533
X (m)	210	1175	2875	5275	7775	10275	13775

Source: Authors, (2023).

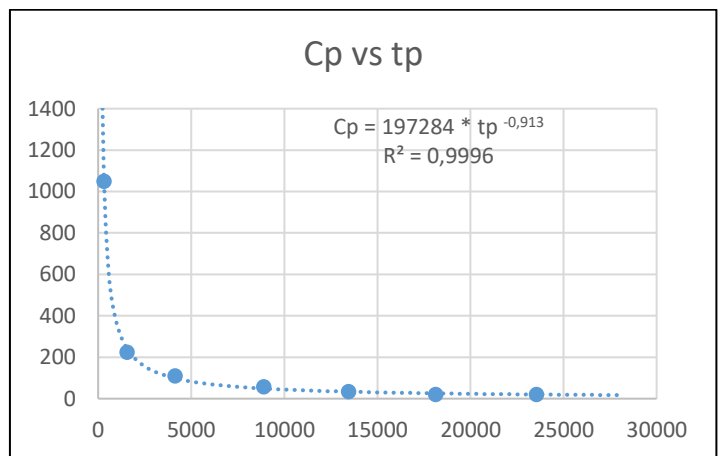


Figure 17: Cp vs tp , Severn River, with 1kg RWT injection. Source: Authors, (2023).

The potential relationship in Excel of the $Cp(tp)$ values is:

$$Cp(tp) \approx 197284 * tp^{-0.913} \quad (24)$$

This means that approximately $\alpha \approx 197284$, for the RWT, and the parameter " b " is $b \approx 0.913$.

To determine the state function, $\phi(tp)$, equation (23) is used:

$$\phi \approx \frac{10^9 (\mu g)}{7540 \left(\frac{L}{s}\right)^{1.16}} * tp^{-0.087} \approx 0.58 * tp^{-0.087} \quad (25)$$

The resulting values of ϕ (tp) are shown in the following Table 2:

Table 2: Resulting values of equation (25).

Site	tp (s)	ϕ
A	300	0.35
B	1740	0.30
C	4140	0.28
D	8880	0.263
E	13440	0.254
F	18120	0.247
G	23533	0.242

Source: Authors, (2023).

Now, using equation (21) for the peak concentration as a function of ϕ , the Cp values are calculated for the curves from A to G:

$$Cp \approx \frac{M}{\phi * Q * tp * 1.16} \quad (26)$$

The following data are then left, Table 3:

Table 3: Comparison of measured vs calculated values of Cp(t) in each site.

	A	B	C	D	E	F	G
Cp (Ppb) measured	1050	225	110	58	34.5	21	20
Cp (Ppb) calculated	1080	217	95.5	49.0	33.5	25.5	20.1
$\Delta\%$	3%	4%	16%	18%	3%	21%	0.5%

Source: Authors, (2023).

With these results within compatible error percentages as acceptable for hydraulics, it is shown that the calibration of the instruments in the tracer measurements, are compatible in this case for RWT in the Welsh channel.

V. CONCLUSIONS

1. In this article it is noted that diffusion as a phenomenon of random diffraction of tracer particles, corresponds to "jumps" between "gaps" (vacancies) in the semi-crystalline structure of the liquid, according to the model of J. Frenkel, but that these jumps occur at all scales, in a fractal way, and regulated by the sequence of bifurcations towards the chaotic state, according to Feigenbaum's model.

2. The dispersive evolution of tracers in turbulent flows, from the molecular point of view, can be seen as a process in two phases that depend on the tracer itself and not so much on the flow itself, unlike what is maintained by contemporary models that propose a trapping of the tracer in the peripheral zone (ADZ and TS) with thermodynamic questions.

A first phase corresponds to the "ion-dipole" interaction of the solute and water, which destroys the solid configuration of the tracer. And a second phase dependent on the "ion-ion" interaction, in which the "ionic clouds" of the electrolyte itself, slow down its movement, thanks to the "Einstein-Stokes" effect, which adds additional viscous friction, delaying the σ tracer cloud of the flow itself. This mechanism directly explains the "non-Fickian bias" of experimental curves.

3. Based on the existence of a state function, $\phi(t)$, these interactions can be explained, from the definition of a relationship between "residence times" of the plotter particles, for a Normal distribution, covering the Gaussian curve only between $-\sigma$ and $+\sigma$, and another between $-\infty$ and $+\infty$, which leads to define the Brownian process in terms of the Svedberg constant, $\alpha \approx 1.54$, which connects to Feigenbaum's constant.

4. Several equations are developed, based on " ϕ " and " α ", a factor that relates "horizontal" and "vertical" magnitudes in the dynamics of the tracers, and therefore allows to analyze the reliability of the measurements, since if they are calculated separately, and if they coincide appropriately, they give a vision of the goodness of the calibration of the measurements.

5. These equations are applied to Fluorimetric tracer (RWT) measurements in Wales, and the results of which are documented with great precision in articles reviewed in the literature. The results are satisfactory, and allow to open an interesting door to the analysis of Water Quality studies.

VI. AUTHOR'S CONTRIBUTIONS

Conceptualization: Alfredo José Constain, Gina Peña Olarte and Carlos Peña Guzman.

Methodology: Alfredo José Constain, Gina Peña Olarte and Carlos Peña Guzman.

Investigation: Alfredo José Constain, Gina Peña Olarte and Carlos Peña Guzman.

Discussion of results: Alfredo José Constain, Gina Peña Olarte and Carlos Peña Guzman.

Writing – Original Draft: Alfredo José Constain and Carlos Peña Guzman.

Writing – Review and Editing: Alfredo José Constain and Carlos Peña Guzman.

Resources: Alfredo José Constain and Carlos Peña Guzman.

Supervision: Alfredo José Constain and Carlos Peña Guzman.

Approval of the final text: Alfredo José Constain, Gina Peña Olarte and Carlos Peña Guzman.

VII. ACKNOWLEDGMENTS

The support of the company FLUVIA TECH, as well as the University of La Salle of Colombia for the realization of this Article, is appreciated.

VIII. REFERENCES

- [1] Constain A. "Definición y análisis de una función de evolución de solutos dispersivos en flujos naturales". Dyna, Volumen 175. Pp. 173-181. 2012
- [2] Bockris J. & Reddy A. Electroquímica moderna. Vol 1. 1980.
- [3] Frenkel J. "Kinetic theory of liquids". Dover. USA, 1955.
- [4] Constaín A. & Lemos R. "Una ecuación de la velocidad media del flujo en régimen no uniforme, su relación con el fenómeno de dispersion como función del tiempo y su aplicación a los estudios de calidad de agua". Ing. Civ. Vol 146 pp. 114-135. 2011.
- [5] Constaín A. "A thermodynamic view of tracer plume evolution: Complete mixing condition evaluation". EPJ Web of conferences, 50, 03002: pp. 03001.p1-030001.p7. 2013.
- [6] Gerasimov YA., Dreving V., Eriomina E., Kiseliov A., Lebedev V, Panchenkov G. & Shliguin. "Curso de Química-Física", Vol. 2. Editorial MIR. 1980.
- [7] Damaskin B.B. & Petri O.A. "Fundamentos de la electroquímica teórica". Editorial MIR, 1981.

- [8] Prigogine I. "El fin de las certidumbres". Editorial Andrés Bello. 1997,
- [9] Kondepudi D. & Prigogine I. "Modern Thermodynamics". Wiley. 1998
- [10] Kirillin V.A, Sichev V.V & Scheindlin A.E. "Termodinámica técnica". Editorial MIR.1986.
- [11] Constaín A. , Peña-Olarte G. & Peña-Guzmán C. "Dispersion and turbulence: A close relationship by means of a State Function". Itegam-Jetia. V7. n. 30 pp 18-28. 2021.
- [12] Lees M.J, Camacho L.A. & Chapra S. "On the relationship of Transient storage and aggregated dead zone models of longitudinal solute transport in streams". Water Resources research, 36(1): pp. 213-224. 2000.
- [13] Atkinson T.C. & Davis P.M. "Longitudinal dispersion in natural channels; 1. Experimental results from the River Severn", 1, UK. Hydrology and Earth systems Sciences, 4(3): pp. 345-353. 2000.
- [14] Atkinson T.C. & Davis P.M. "Longitudinal dispersion in natural channels; 1. Experimental results from the River Severn", 2, UK. Hydrology and Earth systems Sciences, 4(3): pp. 345-353. 2000.
- [15] Bunge M. "Teoría y realidad". Ariel. 1981.
- [16] Miller J.H. "A crude look at the whole". Basic Books, 2015.
- [17] Stewart I. Does God play dice? The new mathematics of chaos". Penguin Books. 1986.
- [18] Constain A, Peña Olarte G. & Peña-Guzmán C. "Función de estado de evolución de trazadores, $\phi(U,E,t)$ aplicada a una función de potencia que describe las etapas de la turbulencia".. Revista Ingeniería Civil CEDEX, No. 199: pp. 91-107. 2021
- [19] Von Mises R. "Probability, statistics and truth". Dover. 1957.
- [20] Kreyszig E. "Advanced Engineering mathematics". Wiley, 1968.
- [21] Nicolis G.& Prigogine I. " La estructura de lo complejo". Alianza. 1987.
- [22] Bockris J. & Reddy A. Electroquímica moderna. Vol 1. 1980.
- [23] Frenkel J. "Kinetic theory of liquids". Dover. USA, 1955.
- [24] Constaín A. "Definición y análisis de una función de evolución de solutos dispersivos en flujos naturales". Dyna, Volumen 175. Pp. 173-181. 2012
- [25] Constaín A. , Peña-Olarte G. & Peña-Guzmán C. "Dispersion and turbulence: A close relationship by means of a State Function". Itegam-Jetia. V7. n. 30 pp 18-28. 2021.
- [26] Constain A. & Bernal E. "Metodología básica de instrumentación industrial y electrónica". Editorial U. de la Salle. 2013.
- [27] Constain A. & Lemos R. "Una ecuación de la velocidad media del flujo en régimen no uniforme, su relación con el fenómeno de dispersion como función del tiempo y su aplicación a los estudios de calidad de agua". Ing. Civ. Vol 146 pp. 114-135. 2011.
- [28] Atkinson T.C. & Davis P.M. "Longitudinal dispersion in natural channels; 1. Experimental results from the River Severn", 2, UK. Hydrology and Earth systems Sciences, 4(3): pp. 345-353. 2000.










BEST LABORATORY PRACTICES FOR REDUCING UNCERTAINTY IN THE PRESSURE DIFFERENTIAL (ΔP) MEASUREMENTS IN CORE-FLOODING TESTS FOR THE PETROPHYSICAL CHARACTERIZATION OF RESERVOIRS

Jorge Alberto Rojas P.¹, Jenny Paola Rueda M.*², Jorge Alejandro Sarmiento G.³, Pedro Juan Rojas M.⁴, Jose Luis Mendoza⁵, Cesar Augusto Romero R.⁶ and Carlos Humberto Amaya A.⁷

^{1,2} Ecopetrol, Technology and Innovation Center, ICP, Colombia.

^{3,4,5,6} PSL, Proanálisis, Colombia.

⁷ Industrial University of Santander, Colombia.

¹ <http://orcid.org/0000-0003-2084-2611> , ² <http://orcid.org/0000-0002-4243-2288> , ³ <http://orcid.org/0000-0003-3595-5272> ,
⁴ <http://orcid.org/0000-0002-0712-268X> , ⁵ <http://orcid.org/0000-0003-0373-9786> , ⁶ <http://orcid.org/0000-0001-7775-3527> ,
⁷ <http://orcid.org/0000-0002-9557-7800> 

Email: jorgeal.rojas@ecopetrol.com.co, *jennypa.rueda@ecopetrol.com.co, alejosarmientogalindo@gmail.com, pedro.rojas67@hotmail.com,
jlmendoza.33@gmail.com, carr1214@yahoo.com, carlosh.amaya@correo.uis.edu.co

ARTICLE INFO

Article History

Received: November 25th, 2022

Accepted: February 22th, 2023

Published: February 28th, 2023

Keywords:

SCAL,
Coreflooding,
Permeability test,
Pressure differential (ΔP),
Uncertainty.

ABSTRACT

Special Core Analysis (SCAL) as a tool for characterization of conventional reservoirs in the laboratory reduces the petrophysical uncertainty and optimizes the resolution and precision of rock-fluid petrophysical models to refine reserve estimates, calculate oil in place, and select the best oil-field development mode. Within the SCAL program, measurements of fluid flow capacity through porous media (permeability [Darcy]) are used to characterize geological formations of interest, with the fluctuation of “pressure differential” values being decisive in the calculation of this property. This research focuses on determining the sources that generate these fluctuations and implements a significant reduction by varying certain parameters in the laboratory. Through detailed analysis of the experimental procedure and equipment operation, as well as a statistical analysis, the sources impacting the quality of the measurements were identified. It was found that the precision and accuracy of pressure differential values were considerably low and directly related to: (1) the pressure pulses created in the backpressure system; (2) the high dead volume in the signal conduction lines (piping); and (3) the influence of temperature variation of the measurement environment. Modifications were implemented both in the experimental protocol and the core-flooding equipment, and tests were conducted under the same conditions to observe the changes produced. It was possible to significantly reduce the standard deviation in the measurements of the pressure differential value from 7.08% to 1.45% with respect to the mean. Consequently, these modifications reduced data dispersion, obtaining more-accurate readings of the stability behaviour of the pressure differential value and, thus, generating more-reliable results. The relevance of this work is demonstrated by the improvement in quality and reliability of petrophysical measurements, in addition to the optimization of turnaround times considering that, by reducing dispersion of pressure differentials values, flow stability state in the porous medium is reached in less time, which is a critical condition for permeability evaluations.



I. INTRODUCTION

This study responds to the need to ensure the quality and reliability of the measurements in the coreflooding tests carried out in the laboratories of Ecopetrol's Innovation and Technology Center ICP, likewise due to the representativeness of the results it is suggested if this is the case to apply in external laboratories where *Coreflooding* tests are conducted.

Previous observations [1-2] revealed parameters in the measurements that impact the accuracy and precision of the coreflooding tests and, consequently, the reliability of the results. Therefore, through the development of numerous studies that have been carried out in the laboratory, the causes of uncertainty were identified, solutions were sought to reduce it, and protocols for *coreflooding* tests were adjusted and implemented.

II. EXPERIMENTAL UNCERTAINTY SOURCES

According to statistical studies, no physical quantity can be measured with perfect certainty; there are always errors in any measurement, e.g. [3,4,5]. This means that if you measure a quantity and then repeat the measurement, you will surely get a different value the second time. However, if extreme care is taken in the measurements and more refined experimental methods are applied, errors can be reduced and therefore greater confidence or certainty in the measurements can be obtained.

II.1 ERROR, ACCURACY AND PRECISION

According to *ASTM E177-20 (Use of the Terms Precision and Bias in ASTM Test Methods)* [6] and *ASTM E456 13a-2022 (Standard Terminology Relating to Quality and Statistics)* [7], the **error** of result, is a test result minus the accepted reference value of the characteristic, where *accepted reference value*, is a value that serves as an agreed-upon reference for comparison, and which is derived as: (1) a theoretical or established value, based on scientific principles, (2) an assigned or certified value, based on experimental work of some national or international organization, or (3) a consensus or certified value, based on collaborative experimental work under the auspices of a scientific or engineering group.

The experimental error itself is quantified by its accuracy and by its precision, where **accuracy** is the closeness of agreement between a test result and an accepted reference value and involves a combination of a random component and of a common systematic error or bias component, **precision** is the closeness of agreement between independent test results obtained under stipulated conditions and depends on random errors and does not relate to the accepted reference value [6].

Precision is also known as repeatability or reproducibility. A measurement with a high repeatability tends to give values that are very close to each other.

II.2 TYPES AND SOURCES OF EXPERIMENTAL ERROR

An estimate of measurement uncertainty would be required in a case, in which the uncertainty is an indication of the magnitude of error associated with a value that considers both systematic errors and random errors associated with the measurement or test process [7].

As indicated by Taylor 1997 [3], experimental uncertainties that can be revealed by repeating the measurements are called **random errors**; those that cannot be revealed in this way are called **systematic**. In practice, since a "true" or "correct" value cannot be absolutely determined, an accepted **reference value** can

be used instead for the comparison [8]. In the Figure 1 is explained the terminology from the typical example (e.g., [3], [8]) which use the pattern shots on a target where *the center of the target represents the true value of a measurand*, and results of repeated measurements are compared to shots at the target. Where **Trueness** (the closeness of agreement between the population mean of the measurements or test results and the accepted reference value [7]) improves with the positive direction of the y-axis as it moves up, moving the average results towards the center of the target [8].

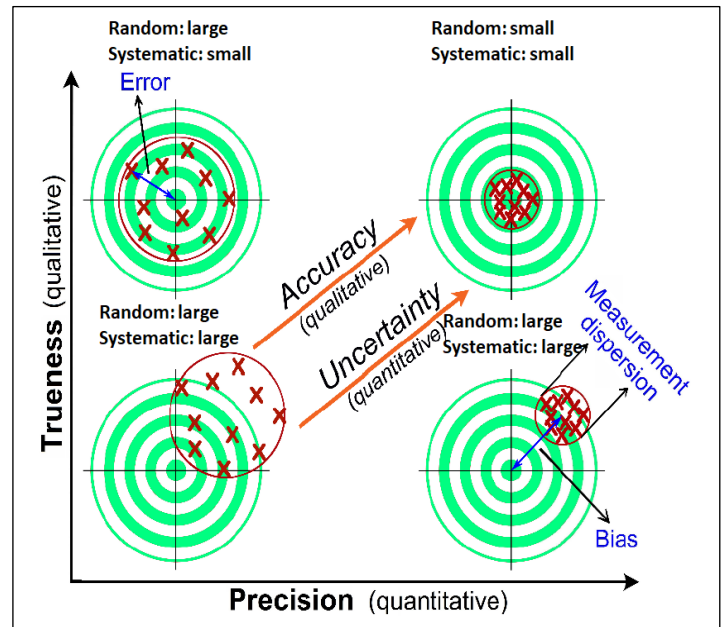


Figure 1: Accuracy and Precision, Systematic and Random Error. With increasing trueness and increasing precision, there is an increasing accuracy and a decreasing uncertainty.

Source: Modified [3, 8].

When the results are offset from the center in the same area of the target, as in the lower quadrants, there is a significant **systematic error**, or **bias** (*the difference between the expectation of the test results and an accepted reference value*), which is shown in the lower right quadrant as the difference between average results and the center of the target. The upper left quadrant demonstrates a number of results exhibiting no significant bias for their average result but large random error for individual trials, and the error of a result is shown as the difference between a single result and the center of the target. The lower left quadrant shows a set of results having both large systematic and random error. In contrast, the upper right quadrant demonstrates a number of results having small random error and no significant bias [8].

Random error of result, is a component of the error that, in the course of a number of test results for the same characteristic, varies in an unpredictable way while systematic error of result, is a component of the error that, in the course of a number of test results for the same characteristic, remains constant or varies in a predictable way [6].

Systematic errors [5] have a non-random character and distort the result of a measurement. They result from erroneous calibration or just from a lack of proper calibration of a measuring instrument, from careless measurements (uncorrected parallax, uncorrected zero-point deviations, time measurements uncorrected for reaction time, etc.), from impurities in materials, or from causes the experimenter is not aware of. The latter are certainly the most dangerous type of error; such errors are likely to show up when results are compared to those of other experimentalists at other

laboratories. Therefore independent corroboration of experimental results is required before a critical experiment (e.g. one that overthrows an accepted theory) can be trusted. These types of errors are corrected or minimized by predicting the behavior of the experimental process. [4].

Random errors [5] are unpredictable by their very nature. They can be caused by the limited precision of instrumental readings, but are ultimately due to physical noise, i.e. by natural fluctuations due to thermal motions or to the random timing of single events. Since such errors are unavoidable and unpredictable, the word “error” does not convey the proper meaning and its prefer to use the term uncertainty for the possible random deviation of a measured result from its true value. Statistical methods are applied to determine its magnitude. [4].

If a measurement is repeated many times, the results will show a certain spread around an average value, from which the estimated inaccuracy in the average can be determined. The probability distribution, from which the measured values are random samples, is supposed to obey certain statistical relations, from which rules to process the uncertainties can be derived. In the case of a single measurement one should estimate the uncertainty, based on knowledge of the measuring instrument [5].

II.3 CALCULATION OF THE EXPERIMENTAL ERROR

An error of theoretical importance [4], is the basis for the development of the theory of errors and their propagation, is the real uncertainty or real error, E_x , of a x number –result of a measurement or a calculation–, defined as: the difference between the values: real, X , and approximate or measured, x , that is: (1).

$$E_x = X - x \quad (1)$$

where: X = numerical data obtained through a measurement or calculation, but which remains constant during the measurement process (wherefore the name real value), and x = measured value or numerical value obtained through a calculation.

II.4 THE MEAN AND THE STANDARD DEVIATION

Mean or Arithmetic Average, of a population, μ , average or expected value of a characteristic in a population – of a sample, \bar{x} , sum of the observed values in the sample divided by the sample size. The mean is a measure of centrality or central tendency of a distribution of observations. It is most appropriate for symmetric distributions and is affected by distribution nonsymmetry (shape) and extreme values [9, 10]. The calculation of the mean is the sum of the n sample values divided by the number of values, n . This equation is (2):

$$\bar{x} = \frac{1}{N} \sum_{i=1}^N x_i = \frac{1}{N} (x_1 + x_2 + \dots + x_{N-1} + x_n) \quad (2)$$

Where x_i is the i -th value of x measured.

Standard deviation—of a population, σ , the square root of the average or expected value of the squared deviation of a variable from its mean; —of a sample, s , the square root of the sum of the squared deviations of the observed values in the sample from their mean divided by the sample size minus 1 [10].

$$\sigma_x = \sqrt{\frac{1}{N-1} \sum_{i=1}^N (x_i - \bar{x})^2} \quad (3)$$

The meaning of the standard deviation is observed in figure 2, which shows data with a mean μ , as it is observed, the greater the standard deviation, the greater the dispersion of the data around the mean. The normal distribution is a symmetrical, bell-shaped curve and is completely determined by its mean, μ , and its standard deviation, σ . The parameter μ locates the center, or peak, of the distribution, and the parameter σ determines its spread. The distance from the mean to the inflection point of the curve (maximum slope point) is σ .

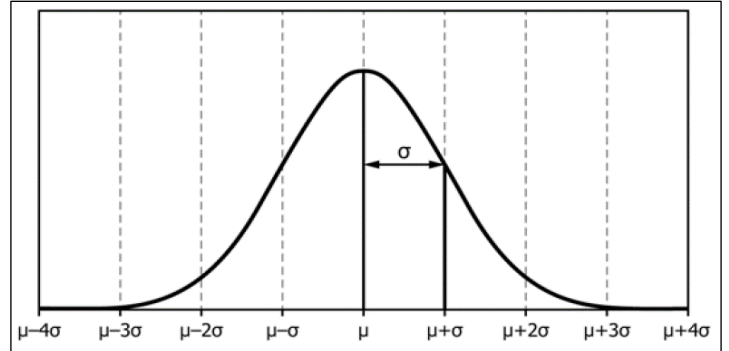


Figure 2: Normal Distribution and Relationship to Parameters μ (\bar{x}) representing the “center” and σ (s) representing the “spread”. Source: [10].

For measurements with only random errors, as seen in Figure 3, 68% of the data values are in an interval around mean ± 1 standard deviation; 95% of the data values are in an interval around mean ± 2 standard deviations, 99.7% of the data values are in an interval around mean ± 3 standard deviations.

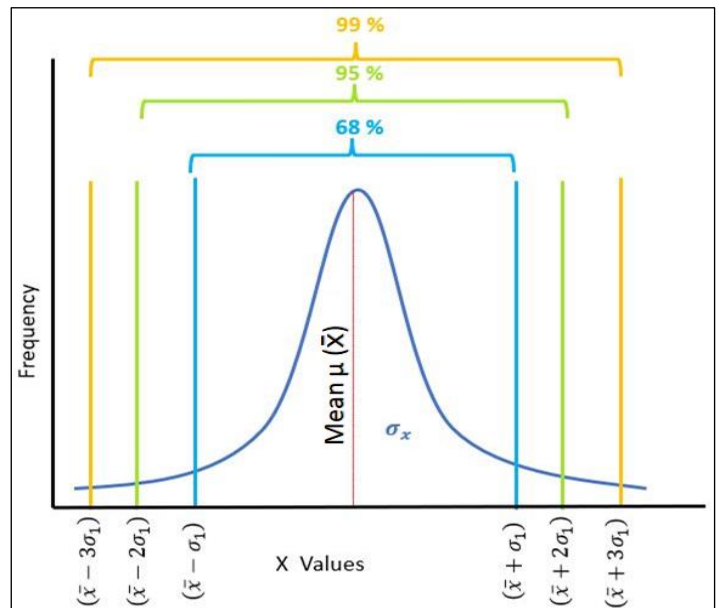


Figure 3: Probabilities in the normal distribution. 99%, 95% y 68%. Source: Authors based on [9].

II.5 REPORT OF RESULTS OF EXPERIMENTAL MEASUREMENTS

When the result of the experimental measurement of a quantity x is reported, the result should be reported in two parts. First, the best estimate of the measurement is reported. The best estimate of a set of measurements is usually reported as the mean μ (\bar{x}) of the measurements. The variation in measurements is usually reported as the standard deviation of the measurements. The measured quantity may then be presented in the following ways:

- $\bar{x} \pm (\sigma_x)$ for 68% confidence
- $\bar{x} \pm (2 * \sigma_x)$ for 95% confidence
- $\bar{x} \pm (3 * \sigma_x)$ for 99% confidence

The point of using a statistic is to summarize the data set and estimate a corresponding population characteristic or parameter, or to test a hypothesis [10].

III. MATERIALS AND METHODS

The laboratories where rock-fluid interaction is evaluated base their experiments on the forced flow of fluids through a porous medium. This porous medium is usually a rock sample taken from a core or sometimes the sample is a sand pack. These laboratory tests are usually known as *coreflooding*.

In the laboratory, coreflooding tests are made to carry out the petrophysical characterization of a Formation of interest, through a formation water sensitivity analysis, critical rates, relative permeabilities; coreflooding tests are also carried out for recovery tests, optimization, and productivity of wells. Therefore,

in this report, the term *coreflooding* is used to refer to any of these experiments.

The purpose of this work is to evaluate the quality of the measurements during a coreflooding. The most determining measurement in coreflooding is the pressure differential or pressure drop (ΔP) across the sample. The pressure differential measurements is used to calculate the permeability of the rock using Darcy's law (4), Fundamental law governing the flow of fluids through porous media, formulated by civil engineer Henry Darcy in 1856 [11, 12, 13] based on his experiments in filtration of water in vertical sand beds.

$$Q = \frac{-KA (P_b - P_a)}{\mu L} \tag{4}$$

Where Q is the volumetric flow rate [m^3/s], K is the permeability of the porous medium [mD] μ is the viscosity of the fluid [$Pa \cdot s$], A is the cross-sectional area of the rock [m^2], L is the length of the sample [m], and the pressure drop through the medium ($P_b - P_a$) or pressure differential ΔP [Pa].

III.1 DESCRIPTION OF THE RESULTS

A history of the results obtained in the experimental area of Special Core Analysis of the Production Optimization and improved recovery laboratory at the Ecopetrol Innovation and Technology Center, ICP, was reviewed; as an example, the results obtained in a sensitivity test of the Formation to the injection of production water in a sample of a well from the Acacias field located in the Llanos Orientales basin in Colombia are shown.

The data in Figure 4 shows the behavior of the pressure differential during the injection of production water at a flow rate of 1 cc/min in a stable flow period.

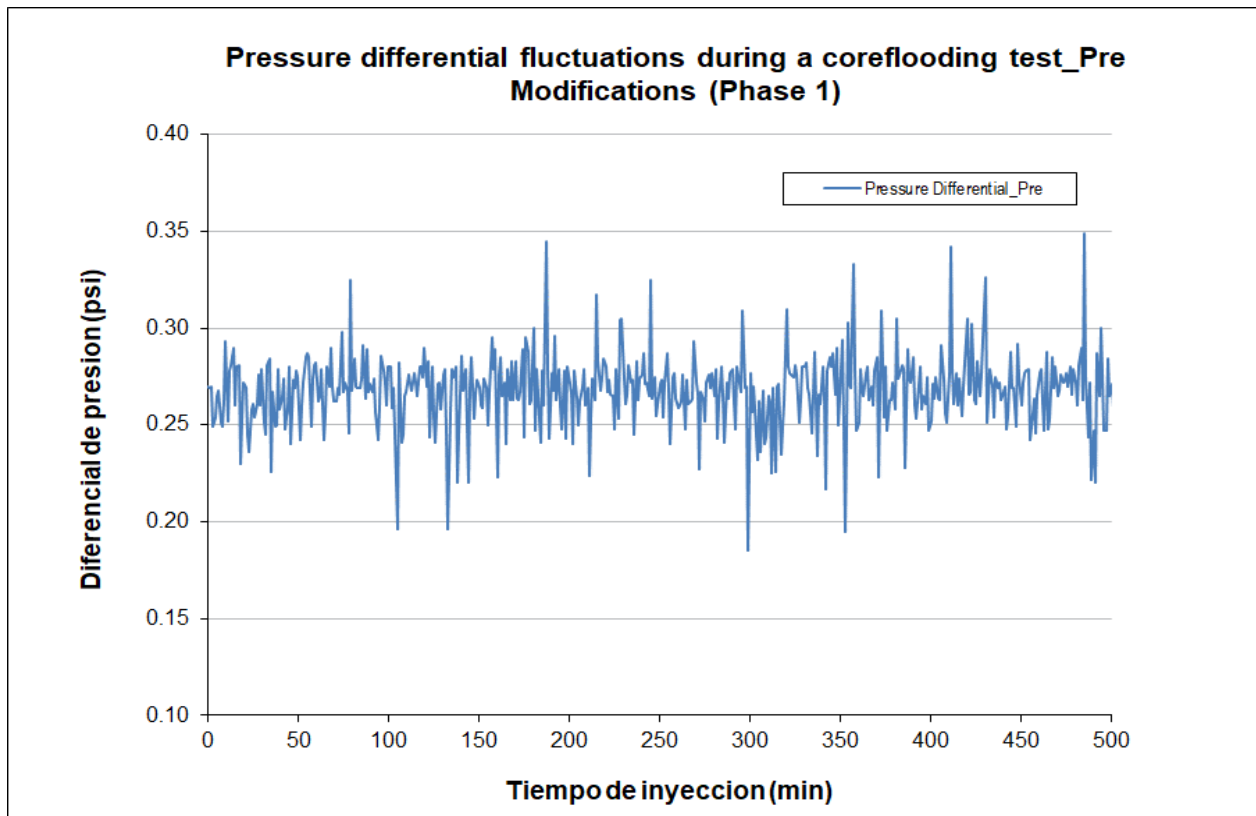


Figure 4: Pressure differential fluctuations during a coreflooding test. Source: Authors, (2022).

As observed in Figure 4, there are fluctuations in the pressure differential in the range of 0.18 - 0.35 psi. Considering that water is being injected at a constant flow, there is an incompressible single-phase flow at a steady state and therefore the pressure differential would be expected to remain constant.

In order to objectively evaluate these fluctuations, it is necessary to perform a statistical analysis and determine the standard deviation of the data. Table 1 presents a basic statistical analysis for a sample of pressure differential data during a sensitivity test.

Table 1: Initial statistical analysis (Phase 1).

variable	valor
Mean	0.2678
Typical error	0.0008
Median	0.2690
Mode	0.2800
Standard deviation	0.0190
Sample variance	0.0004
Kurtosis	3.6620
Asymmetry coefficient	-0.0048
Range	0.1640
Minimum	0.1850
Maximum	0.3490
Addition	139.8100
Account	522.0000
Confidence level (95.0%)	0.0016
Confidence interval 95%	0.0379
Standard deviation in percentage	7.0810
Data outside CI (95%)	29.0000
Data outside CI %	5.5556

Source: Authors, (2022).

The data evaluated follow a normal distribution as shown in figure 5, with a mean of 0.2678 psi, standard deviation of 0.019 psi, taking then that the 95% confidence interval will be ± 0.038 as seen in (5):

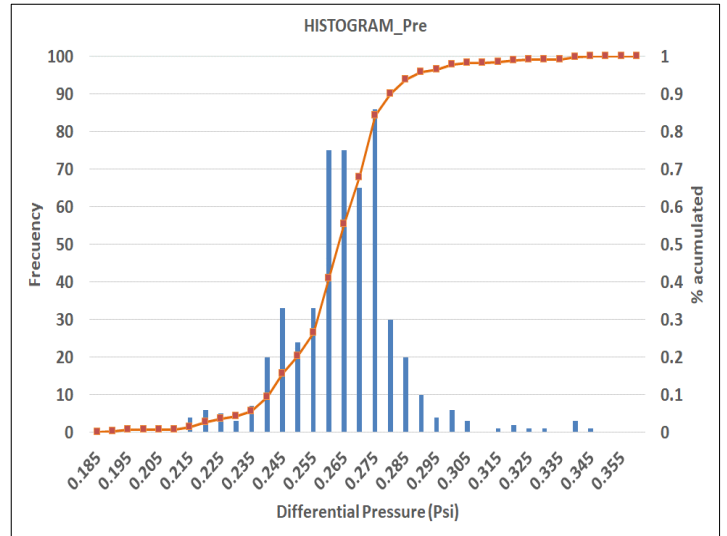


Figure 5: Distribution of pressure differential values (Phase 1).

Source: Authors, (2022).

$$\bar{x} \pm (2 * \sigma_x) = 0.2678 \pm (2 * 0.019) = 0.2678 \pm 0.038 \text{ psi} \quad (5)$$

In figure 6, the moving mean for groups of 14 data was calculated and the confidence interval (95%) was estimated. For practical purposes, the confidence interval on the graph means that it's 95% sure that the measurement will fall in that range, between the two green lines. If we express the standard deviation as a percentage, we observe that the uncertainty of the data in the experiment is 7.08%, which considering the absolute error of the SMAR (pressure differentials sensor) measurement instrument with a precision of ± 0.006 psi or 0.001% is substantially high.

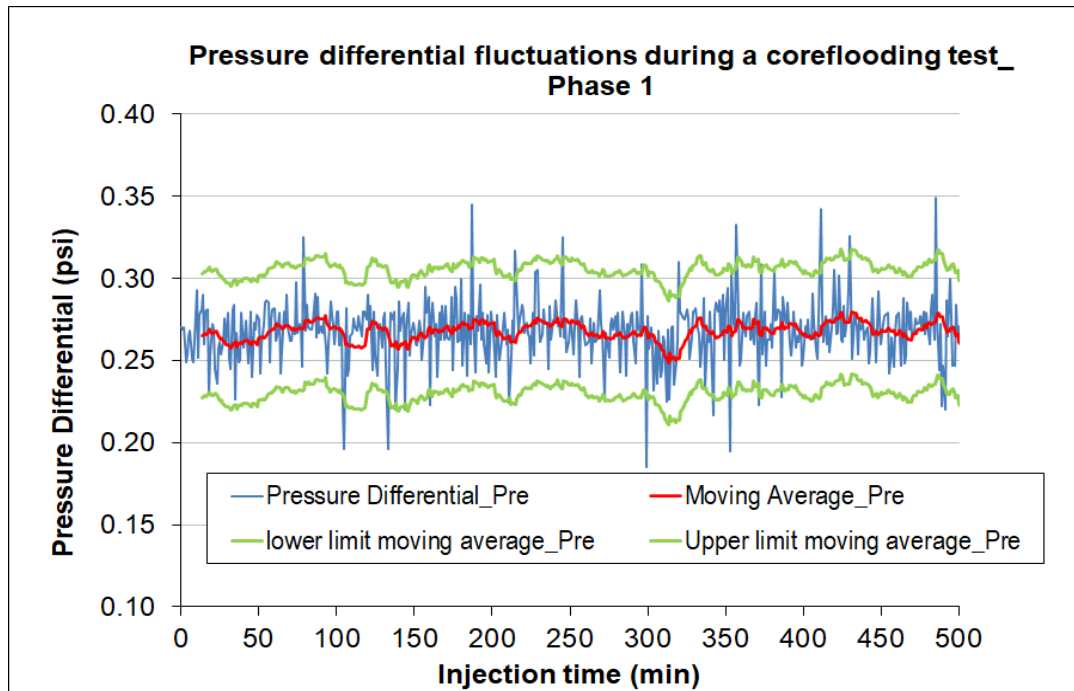


Figure 6: Confidence level (95%), for the pressure differential measurements.

Source: Authors, (2022).

In order to reduce the uncertainty in the measurements, the causes were investigated by reviewing the procedures and experimental configuration of the coreflooding equipment.

III.2 IDENTIFICATION OF THE CAUSES OF DATA DEVIATION

Figure 7 schematically presents the configuration of the coreflooding equipment where the production water sensitivity test was carried out. Basically, the equipment consists of a pump that

injects the fluid into the confined rock sample in the coreholder, with a pressure established in the backpressure (counterpressure or Pore Pressure). The coreholder and the cylinder containing the injected fluid are inside the furnace at the test temperature. The injection rate, the backpressure or pore pressure, the confinement pressure of the sample and the temperature of the test are established according to the case study and the conditions that this requires, generally they are the reservoir conditions or very similar to these.

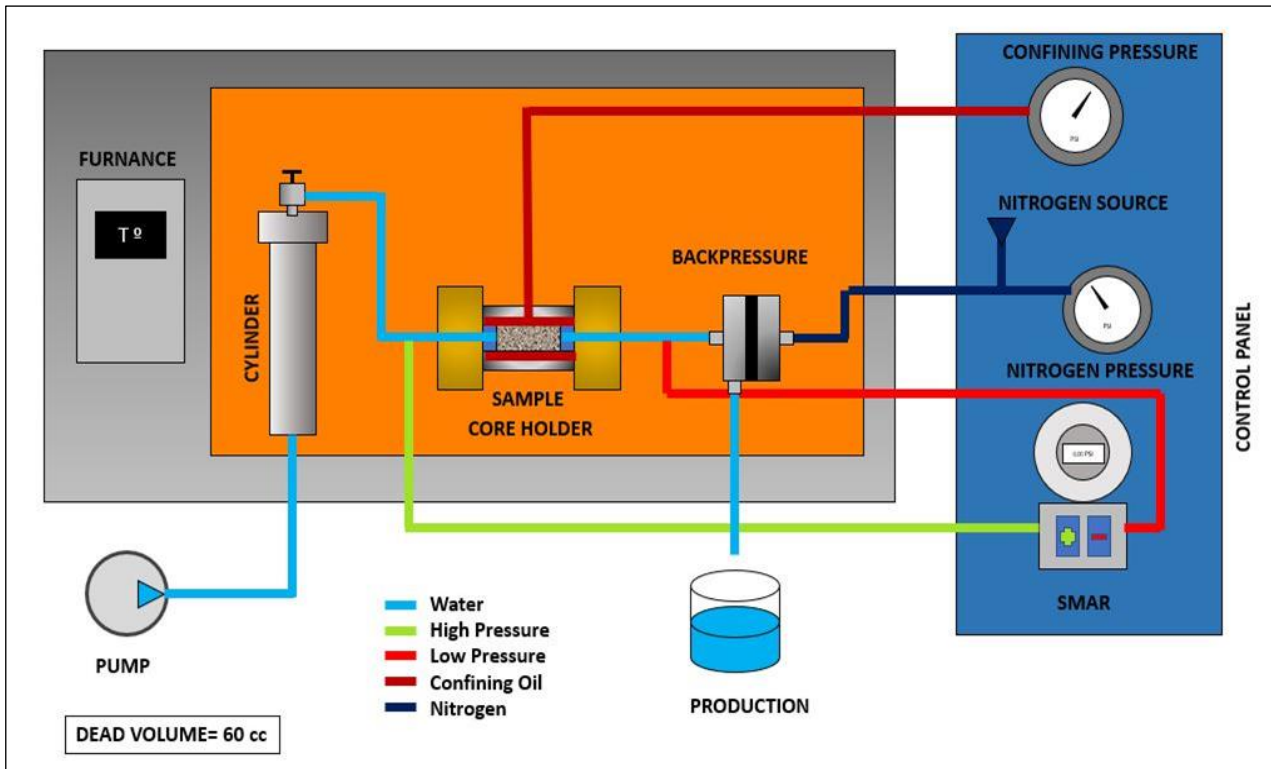


Figure 7: Schematic representation of the permeameter.

Source: Authors, (2022).

The first observation was related to the backpressure (Pore Pressure) used, those used in some tests did not have the characteristic of the gas dome type. The gas dome type has a pressurized nitrogen chamber at working pressure that cushions the fluctuations typical of a backpressure valve. Without this damping, the pressure pulses produced in the backpressure travel in countercurrent and are reflected in the pressure differential measurement.

A second observation was identified in the excess dead volume of the ducts that carry the signal from the sample to the instrumentation. The pressure sensors, both differential and backpressure and confinement, are located in a control panel attached to the equipment. Therefore, the analog signal is transmitted with mineral oil as the medium, from the coreholder to the control panel through 1/8" steel lines. This situation makes the thermal expansion of the fluid representative and is probably influencing the measurement.

A third observation is related to the room temperature or temperature at which the laboratory is located at the time of carrying out the tests. These types of tests are of long duration and must be carried out without interruption. Therefore, the laboratory temperature must also remain constant during the test. However, the air conditioning is turned off at night and due to changes in temperature, although the furnace temperature remains constant,

fluctuations in the confining pressure and changes in the mean value of the pressure differential are observed.

III.2 IMPLEMENTED IMPROVEMENTS

Figure 8 shows a scheme of the equipment with the modifications made by the laboratory personnel to reduce possible sources of error. The changes made in accordance with the recommendations were:

1. Installation of a cylinder with pressurized nitrogen at working pressure in line with production before backpressure. In this way the pressure pulse generated in the backpressure valve is damped inside the cylinder and prevents it from affecting the pressure differential.

2. The length and diameter of the signal lines to the control panel were reduced. The Smar was installed directly on the furnace wall, the flow lines were optimized thus reducing the dead volume of the equipment considerably.

3. To the third effect it was tested 1. the steel lines that lead to the signal of pressure differential were replaced by Teflon lines, since Teflon is a thermal insulator, the effect of room temperature variations on the pressure differential is substantially reduced. It must be taken into account that the maximum pressure that Teflon resists is 800 psi; consequently, it is necessary to prevent injection or displacement pressure from exceeding this limit. 2. Given the

cases in which higher pressures are required, an independent air conditioning system was structured for the laboratory to control the environmental conditions and eliminate this effect. In laboratories

where it is not possible to control the air conditioning, it is recommended to cover the steel lines with thread sealant tape or Teflon tape.

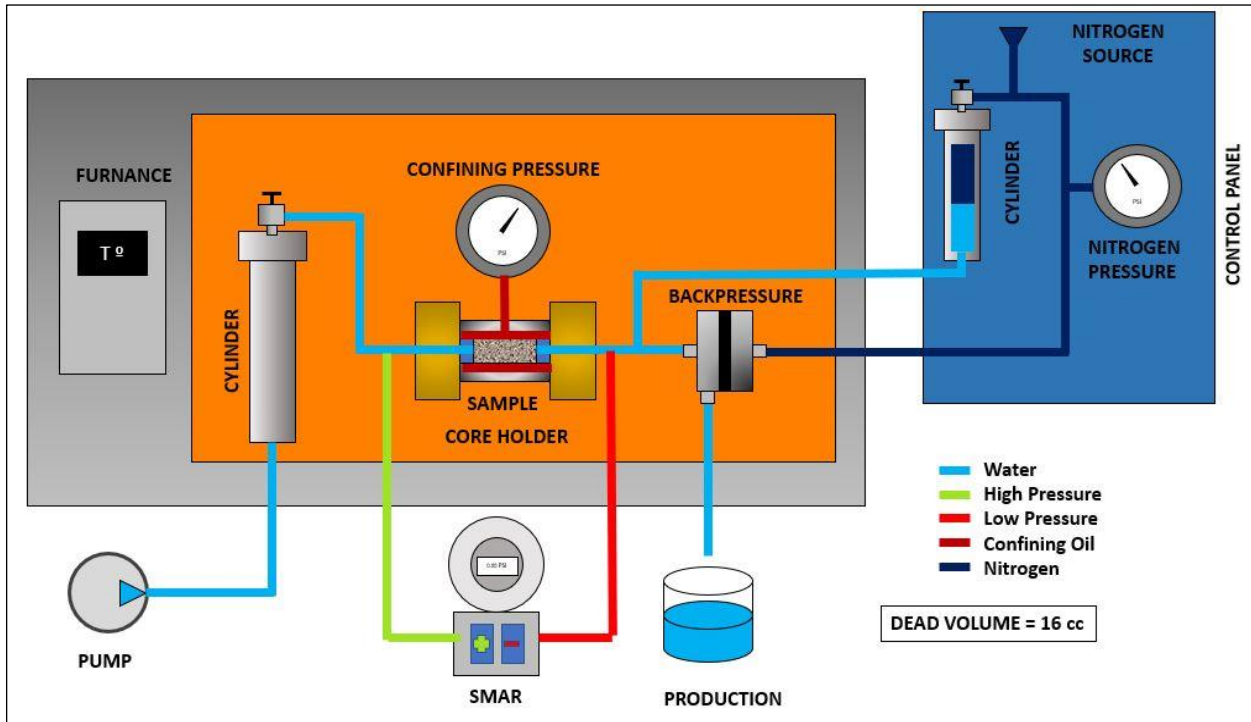


Figure 8: Diagram of the permeameter after modifications.
Source: Authors, (2022).

IV. RESULTS AND DISCUSSIONS

Once the modifications to the different permeameters were implemented, the experiment was resumed and the test

continued under the same conditions. Figure 9 shows the new behavior of the pressure differential.

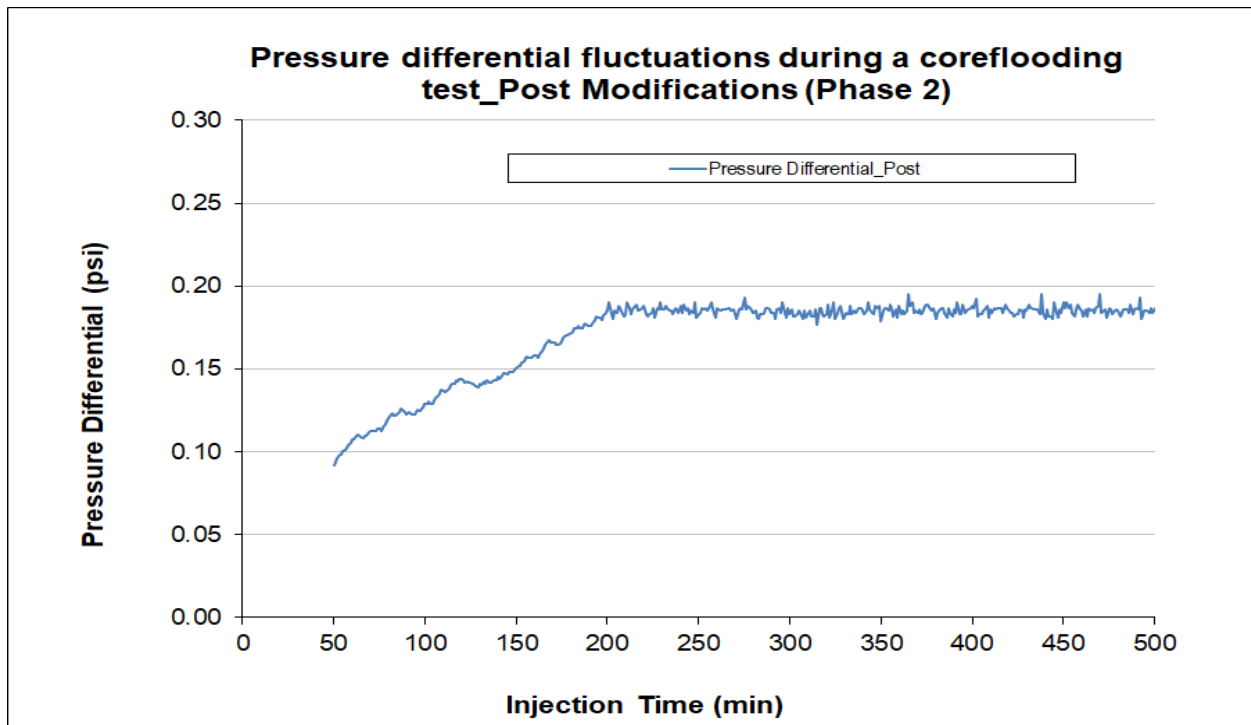


Figure 9: Fluctuations in the pressure differential measurements during a coreflooding test, after making the modifications in the permeameter.
Source: Authors, (2022).

Table 2 shows a statistical summary of the data taken after making the modifications to the equipment. It was identified that the value of the **mean** changed, showing that **systematic errors in the experiment were corrected**. Values such as the standard deviation and typical error decreased, which shows that the modifications made considerably reduced the number of errors when performing a coreflooding test in the permeameters used.

Table 2: Final statistical analysis (Phase 2).

Variable	Worth
Mean	0.1853
Typical error	0.0002
Median	0.1855
Mode	0.1860
Standard deviation	0.0027
Sample variance	0.0000
kurtosis	1.0715
Asymmetry coefficient	0.3001
Range	0.0180
Minimum	0.1770
Maximum	0.1950
Addition	59.6670
Account	322.0000
Confidence level (95.0%)	0.0003
Confidence interval 95%	0.0054
Standard deviation in percentage	1.4564
Data outside IC	19.0000
Data outside IC %	9.0062

Source: Authors, (2022).

Figure 10 shows the histogram of the pressure differential data after making the modifications, which allows us to conclude that the modifications decreased the dispersion of the data, allowing better readings of the differential behavior, and thus giving more reliable results.

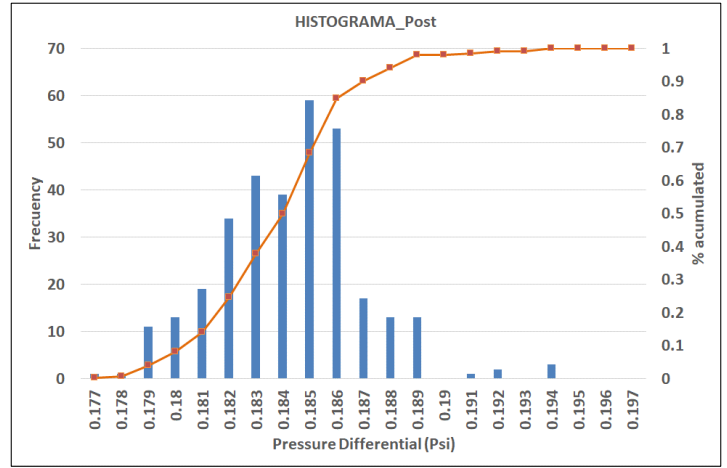


Figure 10: Histogram of the pressure differentials after the modifications made (Phase 2).

Source: Authors, (2022).

In Figure 11, the moving mean for groups of 14 data was calculated and the confidence interval (95%) was estimated. If the standard deviation is expressed as a percentage, it is observed that the uncertainty of the data in the test after making the modifications in the equipment is 1.45%. The evaluated data follow a normal distribution as shown in figure 5, with a mean of 0.1853 psi, standard deviation of 0.0027 psi, taking then that the 95% confidence interval will be ± 0.0054 as seen in (6):

$$\begin{aligned} \bar{x} \pm (2 * \sigma_x) &= 0.1853 \pm (2 * 0.0027) \\ &= 0.1853 \pm 0.0054 \text{ psi} \end{aligned} \tag{6}$$

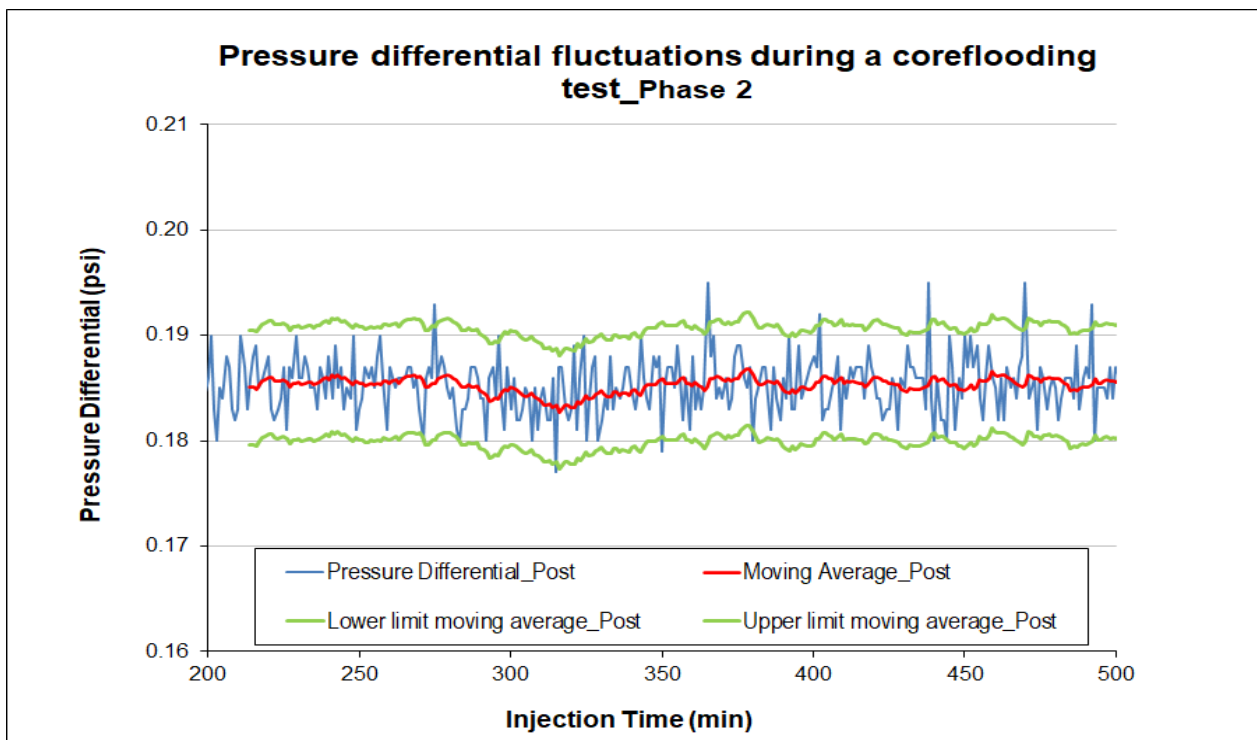


Figure 11: Fluctuations in the pressure differential data after making the modifications in the experimental protocol (Phase 2).

Source: Authors, (2022).

Figure 12 shows a comparison between the results obtained Pre and Post (phase 1 and phase 2) adjustment in the protocol of the permeameter equipment. The initial results presented a standard deviation of 0.019 psi, with a mean of 0.2678 psi and a 95% confidence interval of 0.0379 psi. While the results taken after the modifications in the equipment have a standard deviation of 0.0027 psi, with a mean of 0.1853 psi and a confidence interval of 95% of 0.0054 psi. Expressing the standard deviation as a percentage, it

can be seen that the uncertainty of the measurements was reduced from 7.08% to 1.45%.

The relevance of this work is given by the improvement in the quality and reliability of the measurements, in addition to the optimization of the time of the experiments, since by reducing the dispersion of the pressure differentials data, it will be achieved in less time the stable flow state in the porous medium, a critical condition for permeability evaluations.

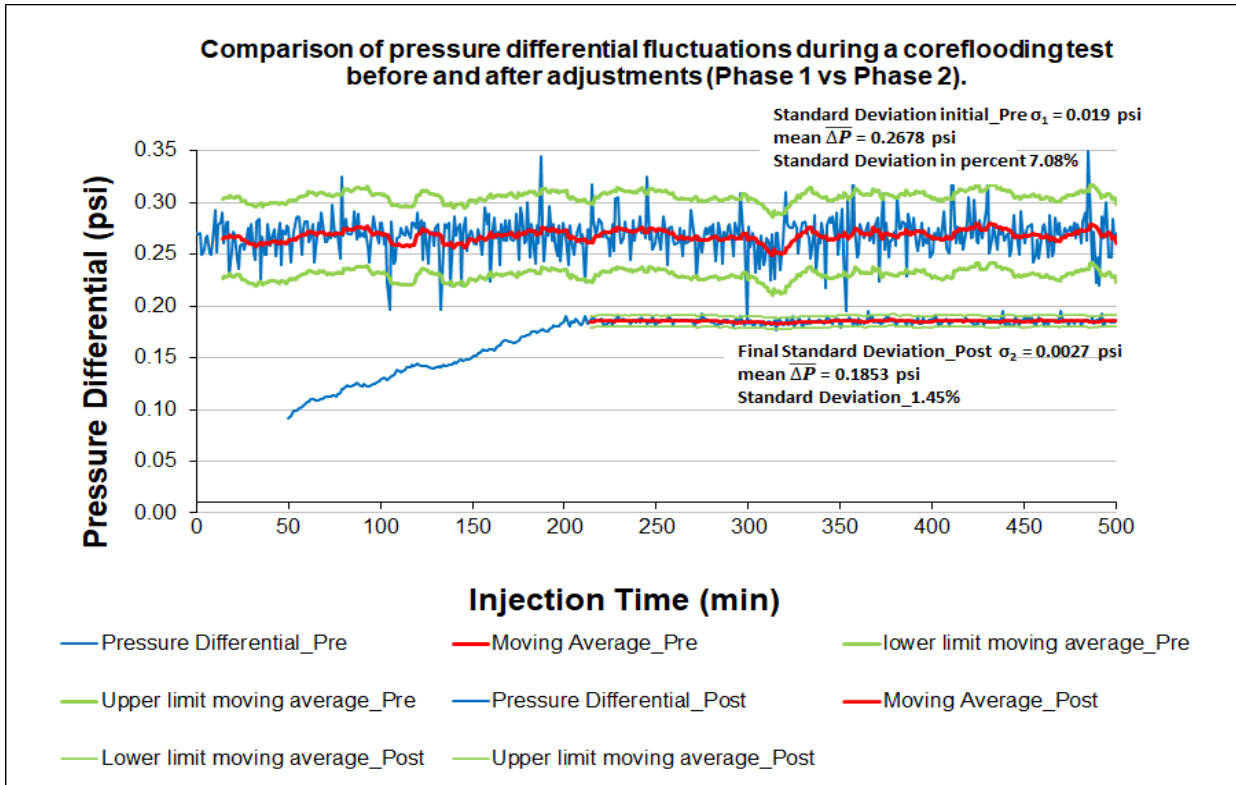


Figure 12: Comparison of pressure differentials data during coreflooding, before and after making the modifications in the permeameter protocols.
Source: Authors, (2022).

V. CONCLUSIONS

In the process of evaluating the quality of the data resulting from the coreflooding, parameters were identified in the pressure differential measurements, which present fluctuations that impact the stabilization time. A deviation of 7.08% was observed with respect to the mean of the measurements, which is considered high and affects the execution time and results of the tests.

Through detailed analysis of the experimental procedure and equipment operation, the sources that were impacting the quality of the measurements were identified and modifications to the equipment were recommended to eliminate them. The precision and accuracy of the pressure differentials displayed on the permeameter were found to be considerably low, and were directly related to the pressure pulses created in the backpressure, the high dead volume in the signal lines, and the influence of the variation of the room temperature.

With the laboratory staff, the proposed modifications were implemented, and new tests were run under the same conditions to observe the changes produced. It was possible to substantially reduce the standard deviation of the measurements to 1.45%, with respect to the mean. Consequently, the stabilization time of the pressure differential was considerably improved and, therefore, the total duration of the tests.

VI. AUTHOR'S CONTRIBUTION

Conceptualization: Jorge Alberto Rojas P., Jenny Paola Rueda M., Jorge Alejandro Sarmiento G., Pedro Juan Rojas M., Jose Luis Mendoza, Cesar Augusto Romero R. and Carlos Humberto Amaya A.

Methodology: Jorge Alberto Rojas P and Carlos Humberto Amaya A.

Investigation: Jorge Alberto Rojas P., Jenny Paola Rueda M., Jorge Alejandro Sarmiento G., Pedro Juan Rojas M., Jose Luis Mendoza, Cesar Augusto Romero R. and Carlos Humberto Amaya A.

Discussion of results: Jorge Alberto Rojas P., Jenny Paola Rueda M. and Jorge Alejandro Sarmiento G.

Writing – Original Draft: Jorge Alberto Rojas P and Carlos Humberto Amaya A.

Writing – Review and Editing: Jorge Alberto Rojas P., Jenny Paola Rueda M. and Jorge Alejandro Sarmiento G and Carlos Humberto Amaya A.

Resources: Jorge Alberto Rojas P., Jenny Paola Rueda M., Jorge Alejandro Sarmiento G., Pedro Juan Rojas M., Jose Luis Mendoza, Cesar Augusto Romero R. and Carlos Humberto Amaya A.

Supervision: Jorge Alberto Rojas P., Jenny Paola Rueda M. and Jorge Alejandro Sarmiento G.

Approval of the final text: Jorge Alberto Rojas P., Jenny Paola Rueda M. and Jorge Alejandro Sarmiento G.

VII. ACKNOWLEDGMENTS

We thank the technical team of the experimental area of Special Petrophysical Analysis of the Production Optimization and Enhanced Recovery Laboratory, Ecopetrol's Innovation and Technology Center, ICP, for their support in this research.

VIII. REFERENCES

- [1] Amaya, Carlos. Adjusting experimental set-up improves relative permeability reliability. CT&F, Vol. 2, Núm. 4. dic. 2003.
- [2] Ecopetrol. Naranjo Carlos, Herrera Julia. Ensayos de reproducibilidad de la Ley de Darcy para asegurar la calidad de los resultados. Piedecuesta. 2011.
- [3] Taylor J. R. An Introduction to Error Analysis. The study of uncertainties in physical measurements, Second Edition, 1997.
- [4] Medina R. S. Breve Introducción a la Teoría de Errores y la Graficación. Universidad Autónoma de Aguascalientes. México. Primera Edición 1997.
- [5] H. Berendsen. A Student's Guide to Data and Error Analysis. Cambridge University Press. First published 2011.
- [6] ASTM International. E177-20. Use of the Terms Precision and Bias in ASTM Test Methods. 2020
- [7] ASTM International. E456-13a (Reapproved 2022) Standard Terminology Relating to Quality and Statistics. 2022
- [8] Villaraga-Gomez, Herminso. X-ray Computed Tomography for Dimensional Measurements. ASNT's Digital Imaging Conference, Foxwoods Resort & Casino, Mashantucket, CT. July 25-26, 2016, American Society for Nondestructive Testing www.asnt.org.
- [9] Birger Stjernholm Madsen. Statistics for Non-Statisticians. Second Edition. Springer 2016.
- [10] ASTM International. E2586-19. Standard Practice for Calculating and Using Basic Statistics. 2019
- [11] API, Recommended Practice. API RP 40, February 1988.
- [12] Exxon Production Research. Coring and Core Analysis Course. 2000.
- [13] McPhee Colin, Reed Jules, Zubizarreta Izaskun. Core Analysis: A Best Practice Guide (Volume 64) (Developments in Petroleum Science, Volume 64) 1st Edition. Elsevier. 2015.